ABSTRACT

Title of Dissertation:	ULTRAFAST NONLINEAR RESPONSE OF ATOMIC AND MOLECULAR GASES IN NEAR-IR AND MID-IR REGIONS
	Sina Zahedopur Anaraki, Doctor of Philosophy, 2017
Dissertation directed by:	Professor Howard Milchberg, Department of Physics Department of Electrical and Computer Engineering

There is a dynamical interaction between an ultrashort laser pulse and the medium it propagates through. At the shortest timescales, the near-instantaneous electronic response of the medium contributes to an induced polarization nonlinearity. On a longer timescale, the vibrational response can contribute, followed on even longer timescales by the rotational response. One of the major consequences of these nonlinearities is that they can induce the collapse and filamentation of the laser pulse, leading to ionization and plasma generation.

In this dissertation, measurements and theory are presented for both the fundamental atomic and molecular nonlinearities themselves (electronic, rovibrational, and ionization rates) in the range λ=400nm-2600nm, and their applications. The media investigated are air constituents (Ar, N_2, O_2), H_2, D_2, and common transparent optical materials. In particular, in one application it is shown that in molecular gases like N_2

and O_2, the propagating laser electric field can pump a rotational wavepacket, producing molecular ensembles with both transient and long-lived ("permanent") alignment components. This alignment, which generates quantum echoes (rotational revivals), can interact with the pulse that generated it (rotational nonlinearity) and with any pulses that may follow. We show that a properly timed train of ultrashort laser pulses can resonate with the rotational revivals, causing a "permanent" alignment in the gas which thermalizes and then drives a strong hydrodynamic response which can exceed that from the plasma heating by a filament.

ULTRAFAST NONLINEAR RESPONSE OF ATOMIC AND MOLECULAR GASES IN NEAR-IR AND MID-IR REGIONS

by

Sina Zahedpour Anaraki

Dissertation submitted to the Faculty of the Graduate School of the
University of Maryland, College Park, in partial fulfillment
of the requirements for the degree of
Doctor of Philosophy
2017

Advisory Committee:
Professor Howard Milchberg, Chair
Professor Christopher Davis
Professor Julius Goldhar
Dr. Jared Wahlstrand
Professor Ki-Yong Kim

Dedication

To my dearest family.

Acknowledgement

First and foremost, I want to thank my advisor Prof. Howard Milchberg for the privilege of working in his labs, learning from and sharing ideas with him. After receiving my master's degree in communications networks, I was looking to find a new direction for my research, when he kindly let me work in his well-equipped laser labs and learn from him and his students.

Starting with no background in ultrafast optics, I want to thank Dr. Jennifer Elle and our lab's former research scientist, Dr. Jared Wahlstrand (currently at NIST), who brought me up to speed, shared their thoughts and helped me with my experiments. I also want to thank my colleagues Dr. Eric Rosenthal, Dr. Nihal Jhajj,Ilia Larkin, Fathollah Salehi, Linus Feder, Bo Miao, Daniel Woodbury and Robert Schwartz, who are always ready to brainstorm and ponder challenging problems. I wish the best of luck to our new lab member Anastasia Korolov in her research. I also appreciate the help of our bright undergraduate assistants Jesse Griff-McMahon, Ryan Smith and Dan Younis.

Almost all of the experiments required custom parts to be made. I want to thank Edd Cole for teaching me the basics of machining, and John 'Jay' Pyle, Nolan Ballew and Dr. Stephen Henderson for helping me in making various parts and components used in my experiments. I also want to thank Dr. Edward Condon and Bryan Quinn for their technical assistance whenever we asked for it.

Finally I want to thank Prof. Ki-Yong Kim, Prof. Christopher Davis, Prof. Julius Goldhar and Dr. Jared Wahlstrand for giving their time to read my thesis, provide comments and serve on my defense committee.

Table of Contents

Dedication ii

Acknowledgement iii

Table of Contents iv

List of Tables vi

List of Figures vii

Chapter 1: Introduction 1
1.1 Motivation and outline of the dissertation 1
1.2 Linear and nonlinear response of media 4
1.3 Laser system 5
1.4 Mid-infrared optical parametric amplifier 8
1.6 Single-shot supercontinuum spectral interferometry 13

Chapter 2: Quantum control of molecular gas hydrodynamics 17
2.1 Introduction 17
2.2 Experimental setup 19
2.3 Experimental results and discussion 21
2.4 Photoacoustic measurement of resonant rotational heating 30
2.5 SSSI measurement of permanent alignment 33
2.6 Saturation caused by centrifugal distortion 37

Chapter 3: Measurement of refractive index of air constituents and wide bandgap solids in mid-IR region 41
3.1 Introduction 41
3.2 Experiment setup 42
3.3 Separation of electronic response from rotational response 44
3.4 Direct measurement of instantaneous nonlinear response in large bandgap solids at mid-IR wavelengths 54
3.5 Spatiotemporal characterization of ultrashort pulses from the near-IR- to the mid-IR 62

Chapter 4: Absolute measurement of the ultrafast nonlinear electronic and rovibrational response in H_2 and D_2 67
4.1 Introduction 67
4.2 Experiment 69
4.3 Rotational Response 71
4.4 Vibrational Response 74

4.5 Extraction of nonlinear coefficients 82

Chapter 5: Bound electron nonlinearity beyond the ionization threshold 85
5.1 Introduction 85
5.2 Experiment Setup 87

Appendix A: Classical work done on a rigid rotor by single impulse 101

Appendix B: Electronic and rotational symmetries in isotropic media 104
Bibliography 107

List of Tables

Table 3.1 Measured electronic Kerr coefficient $n^s_{2,\mathrm{elec}}$ at 1 atm (at probe wavelength of 600 nm and pump wavelength of 800 nm), polarizability anisotropy $\Delta\alpha$, and polarizability derivative $\partial\alpha/\partial Q$. A comparison is made with previous experimental and theoretical work. The rightmost column shows n_2 estimates at 1 atm based on our experimental results for a long pulse at 800 nm……..…52

Table 3.2 Measured $n_2 (1\times10^{-16}\,\mathrm{cm}^2/\mathrm{W})$ for solid samples……..……....61

Table 4.1. Measured electronic Kerr coefficient $n^s_{2,\mathrm{elec}}$ at 1 atm (at probe wavelength of 600 nm and pump wavelength of 800 nm), polarizability anisotropy $\Delta\alpha$, and polarizability derivative $\partial\alpha/\partial Q$. A comparison is made with previous experimental and theoretical work. The rightmost column shows n_2 estimates at 1 atm based on our experimental results for a long pulse at 800 nm…….……81

List of Figures

Figure 1.1. Schematic design of (a) Pulse stretcher. The distance of lens 2 and grating 2 is smaller than that of lens 1 and grating 1, thus the redder parts of the spectrum encounter smaller delay compared to the bluer side. This results in the pulse to be positively chirped. (b) Pulse compressor. The redder side of the spectrum encounters longer delay compared to the bluer side, thus the pulse is negatively chirped……7

Figure 1.2 Parametric gain in a $\chi^{(2)}$ material where a weak input signal at ω_{signal} is amplified by splitting photons at ω_{pump} into two photons ω_{signal} and ω_{idler} such that $\omega_{pump} = \omega_{signal} + \omega_{idler}$ ……..8

Figure 1.3 The output energy of OPA and DFG units when pumped by a 8 mJ, 38 fs Ti:Sapphire laser…….....9

Figure 1.4 Strong pump cause a time dependent change in refractive index of the medium it propagates through. The probe overlaps in time with this refractive index change and acquires phase shift. …….……..……..13

Figure 1.5 Schematic of single shot spectral interferometry setup…….……15

Figure 2.1. Experimental setup for measuring the 2D density profile of the rotationally excited gas at the pump beam focus. The chopper provides alternating pump on/off for background subtraction. (a) Simulation of hole depth vs. initial temperature showing that density hole depth is an excellent proportional measure of initial gas heating. (b) Scheme for (t_1, t_2) delay scan of pulses from pulse stacker……..……21

Figure 2.2. Relative density depression (proportional to heating) measured at 40μs delay due to single-pulse (110 fs FWHM) gas heating versus pump intensity at focus. In argon, plasma generation from multiphoton ionization and tunneling is the only source of gas heating, whereas in diatomic molecules, rotational excitation enables nonlinear absorption below the ionization threshold. The solid black line shows a density matrix calculation of the rotational absorption in N2 and the dashed line is a classical calculation using eq. (2.3). The experimental points deviate from the density matrix simulation at higher intensities due to ionization and plasma absorption, which is not modeled here……..……23

Figure 2.3. Rotational absorption as a function of time delays t_1 and t_2 in the pulse stacker. The images at the top show extracted density hole images for three delays, showing the varying depth of the hole. (a) Interferometric measurement of peak relative depth of gas density hole. The deepest gas density depression corresponds to the peak energy absorption predicted by the simulation. (b) Simulation of absorbed energy ΔE, found by numerically solving eqs. (2.1) and (2.2) and averaging along the

pump beam's confocal parameter. pump beam's confocal parameter. pump beam's confocal parameter……...……27

Figure 2.4. Reduction of rotational heating using two pulses. Blue circles: Measured change in gas density as a function of the time delay t_1 between two pulses spaced near the half revival $T/2$~4.16 ps in N_2. The hole depth is reduced by ~65%. Red crosses: Simulation of rotational energy change per molecule from solving eqs. (2.1) and (2.2) for varying t_1, showing absorption reduction of ~90%.....29

Figure 2.5. Experimental setup for the photoacoustic measurements of gas heating. The inset on the lower left shows a sample trace from the microphone, digitized by an analog-to-digital convertor (ADC). The inset on the upper left shows the amplitude of the sound wave as a function of two delays……...……..…30

Figure 2.6. Experimental (a-c) photoacoustic measurement of the intensity dependence of the microphone data and comparison to density matrix code. In panels **(d-f)** the heating due to the pulses are calculated using density matrix simulation. The width of the pulses is 95fs with peak intensities (a)15 TW/cm^2, (b)40 TW/cm^2, and (c)50 TW/cm^2……...……32

Figure 2.7. (a) At thermal equilibrium for a given *j*-state all of *m*-states are equally likely to be occupied, resulting in net zero birefringence. **(b)** Transitions of the form $j \to j+2$ and $m \to m$ make lower *m*-states to be more likely to be occupied resulting in a net alignment along *z*-axis……..……33

Figure 2.8. In order to measure permanent alignment, we need to have the reference arrive before the first pulse in the pump laser pulse train, and the probe to arrive up to ~60 ps later. This causes the spectral fringes to be too fine for the imaging spectrometer; in order to have both long time delay between reference and probe and also be able to resolve the fringes, we added another Michelson interferometer before the beam enters the spectrometer. We set the delay on this interferometer to 2 ps. The 120 ps apart reference and probe add to the background without making any fringes…….…….35

Figure 2.9. (a)Transient and permanent alignment due to pulse train around t = 0 and full revivals (left column) and half revivals (right column) in N_2 for 8 pulses of 45 TW/cm$^{2.}$ (b) Alignment measured after each pulse in the 8-pulse train. We see saturation of permanent alignment at $5T_r$ (in vicinity of the 5th pulse)……..……36

Figure 2.10.Solid curves show simulation of energy deposition in N_2 for a periodic trains of impulses with fluence of (a) 0.5J/cm^2 and (b) 3J/cm^2 with period of $T = T_r + \varepsilon$. In the first case the pulse train with $T = T_r$ remains resonant even after 14 pulses. In the second case, this pulse train can only remain resonant for 6 pulses……..…….39

Figure 3.1. Diagram of the experiment. A Ti:Sapphire regenerative amplifier pumps an infrared optical parametric amplifier (OPA) to produce a tunable pump pulse and generates visible supercontinuum (SC) in a Xe gas cell. A Michelson interferometer (MI) creates probe and reference SC pulses. Pump and probe/reference beams are crossed in a chamber filled with N_2, O_2, or Ar. The spectral phase and amplitude of the probe is measured and used to find the time-domain phase shift induced by the pump pulse……...……42

Figure 3.2. Experimental results in N_2 and Ar at $\lambda_e = 1250\text{nm}$ central pump wavelength: (a) nonlinear phase shift $\Delta\varphi_{\parallel}(x,t)$ of the probe for $\mathbf{E}_p \parallel \mathbf{E}_e$ and (b) nonlinear phase shift $\Delta\varphi_{\perp}(x,t)$ of the probe for $\mathbf{E}_p \perp \mathbf{E}_e$ in N_2. (c) Temporal lineouts $\Delta\varphi_{\parallel}(x=0,t)$ and $\Delta\varphi_{\perp}(x=0,t)$ in N_2 and their decomposition into electronic and rotational responses, as described in the text. (d) Temporal lineouts of the parallel and perpendicular polarized phase shift in Ar and the perpendicular phase shift scaled by a factor of 3……..45

Figure 3.3.Experimental results in (a) Ar and (b) N_2 at 2200 nm, a wavelength where the pump pulse shape is longer and more complex than at shorter wavelengths……..48

Figure 3.4. Experiment setup for direct measurement of n_2 in thin (L<0.3mm) solid samples. In this experiment we used an InSb camera to images the spot size of the pump focus. Furthermore, we calibrate the pixel counts on the camera to pump intensity. Both pump$\parallel$ probe and pump$\perp$ probe are recorded in the imaging spectrometer simultaneously……..……..58

Figure 3.5. (a) Measured SSSI phase shift in 130 μm of sapphire at pump wavelength 2500 nm. (b) Image of the pump spot calibrated to show the pump intensity at t = 0……..……..59

Figure 3.6. Measured SSSI phase shift in 130 μm of sapphire as a function of pump intensity for wavelengths (a) 1550nm, the loop present in the blue dataset is an indication that the origin $y = 0$ between $\Delta\varphi(y,t=0)$ and $I(y,t=0)$ was not chosen perfectly. Shifting the origin by a few pixel causes the loop to disappear as shown in part (b) with 1550nm, (c) 2000nm and (d)2500 nm. Each color corresponds to a dataset with varied pump energy. In each dataset, a × corresponds to a measured phase shift along the pump spot lineout……...……60

Figure 3.7. Scheme for recording 2D SSSI measurements by scanning the probe across the spectrometer slit. An auxiliary HeNe laser beam is used to track the location of the probe with respect to the slit……63

Figure 3.8. Creating a tilted pulse front using a prism……...……..64

Figure 3.9. (a) Temporal profile of an 800nm pulse with tilted pulse front (deliberately introduced by passing it through a prism) (b), (c) spatial profile of the pulse at t= −50fs and t=50fs. If we integrate the 2D+1 data cube along its time axis we get the total spatial profile of the beam that agrees with the 2D image generated by a CCD camera……..……65

Figure 3.10.. Image of a mid-IR pulse centered at 2600nm at t = 0……...……66

Figure 4.1. Thin gas flow tube. A hole is laser drilled in a stainless steel tube. The tube is crimped to achieve the desired thickness for the interaction between the gas and pump/probe pulses……69

Figure 4.2. **(a)** Pump-induced 1D space- and time-resolved phase shift $\Delta\Phi(x,t)$ for a 46 TW/cm2, 40 fs pulse in H_2 and D_2 for the pump $\mathbf{E}_e$ and probe $\mathbf{E}_p$ polarizations parallel and perpendicular. To increase the signal to noise[29], $\Delta\Phi(x,t)$ is extracted from the average of 200 single-shot interferograms. **(b)** Intensity dependence of the peak phase shift in H_2 (+) and D_2 (×) extracted from the spatial profile of the response $\Delta\Phi(x,t=0)$ for a pump pulse of peak intensity ~80 TW/cm^2…….……70

Figure 4.3. Experimental data on the rotational molecular response in H_2 and D_2. Time-dependent phase shift for $\mathbf{E}_e \parallel \mathbf{E}_p$ as a function of pump pulse duration for (a) H_2 and (b) D_2. Density-matrix simulations of the rotational phase response (using fitted values of the rotational constants as described in the text) are shown as dashed lines. The Fourier transform of the phase shift at times after the 40 fs pump pulse for (c) H_2 and (d) D_2, showing which rotational coherences are excited. The green dashed curves in (c) and (d) show the Fourier transform of the fitted density-matrix simulations……...……73

Figure 4.4. Phase shift of chirped SC probe vs $\Delta\omega = \omega_{p,overlap} - \omega_e$.The measured probe spectral phase is $\varphi(\omega) = \beta_2(\omega-\omega_0)^2 + \beta_3(\omega-\omega_0)^3$, with $\beta_2 = 1675\,\mathrm{fs}^2$, $\beta_3 = 396\,\mathrm{fs}^3$ and $\omega_0 = 3.05\,\mathrm{fs}^{-1}$. The time delay of SC frequency component at ω (left axes) is given $\phi'(\omega)$. (a) Supercontinuum interference spectrum with variably delayed pump pulse superposed. The top axis shows the time corresponding to each frequency component. (b)Experimental and best fit rovibrational simulation plots for (b) H_2 and (c) D_2. The best-fit simulations enabled extraction of $n_{2,\mathrm{elec}}$ and $\partial\alpha/\partial Q$, shown in Table 4.1……...……..79

Figure 4.5. (a) Calculated nonlinear index $2n^s_{2,elec} + n^s_{2,vib} + n^g_{2,vib}$ experienced by the probe as a function of the pump-probe beat frequency $\Delta\omega$ for a 40 fs pulse centered at 800 nm, calculated using Eq. (4.10) (dashed blue) and for and calculated numerically (solid green). The electronic component $2n^s_{2,elec}$ is shown as a red dotted line for

comparison. (b) Calculated nonlinear index $n^s_{2,elec} + n^s_{2,vib}$ for an infrared pulse. The vibrational nonlinearity is resonant for optical frequency near $\Omega_v/2$……83

Figure 5.1. Experimental apparatus for 2D+1 SSSI measurement of field-induced ionization. Not shown: 800 nm rejection mirror after Xe gas cell, auxiliary interferometer for gas target characterization, and pre-target pump spot imaging camera. DM1, DM2, DM3: dichroic mirrors…….……..88

Figure 5.2. Results in Ar for peak pump intensity of 95 TW/cm2 and pulsewidth 42 fs. (a) Measured spatiotemporal phase shift $\Delta\Phi(x,y_0,t)$. (b) An image of the pump spot at the gas target. (c) The phase shift $\Delta\Phi(x,y,t$ =–14 fs), showing mostly the Kerr response. (d) Phase shift $\Delta\Phi(x,y,t$ =+25 fs), showing the Kerr response on the wings and the growing plasma contribution in the center of the beam. (e) Phase shift $\Delta\Phi(x,y,t$ =+100 fs), showing the dominant plasma contribution after the pump pulse. The peak of the pump pulse defines zero for the *x*, *y*, and *t* coordinates……..……..90

Figure 5.3. Results in Kr at a pump peak intensity of 84 TW/cm^2. (a) Measured spatiotemporal phase shift $\Delta\Phi(x,y_0,t)$. (b) An image of the pump spot at the gas target, showing that the Kerr response simply follows the pump intensity profile. (c) The phase shift $\Delta\Phi(x,y,t_0$ – 14 fs), showing mostly the Kerr response. (d) The phase shift $\Delta\Phi(x,y,t_0$+21 fs), showing the Kerr response on the wings and the growing plasma phase shift in the center of the beam. (e) The phase shift $\Delta\Phi(x,y,t_0$+100 fs), showing the negative plasma phase shift long after the pump pulse…….91

Figure 5.4. Results in Xe at a pump peak intensity of 50 TW/cm^2. (a) Measured spatiotemporal phase shift $\Delta\Phi(x,y_0,t)$. (b) An image of the pump spot at the gas target, showing that the Kerr response simply follows the pump intensity profile. (c) The phase shift $\Delta\Phi(x,y,t_0$–14 fs), showing mostly the Kerr response. (d) The phase shift $\Delta\Phi(x,y,t_0$+14 fs), showing the Kerr response on the wings and the growing plasma phase shift in the center of the beam. (e) The phase shift $\Delta\Phi(x,y,t_0$+100 fs), showing the negative plasma phase shift long after the pump pulse……..…….....92

Figure 5.5. Results in N_2 at a pump peak intensity of 115 TW/cm^2. (a) Measured spatiotemporal phase shift $\Delta\Phi(x,y_0,t)$. (b) An image of the pump spot at the gas target, showing that the Kerr response simply follows the pump intensity profile. (c) The phase shift $\Delta\Phi(x,y,t_0$ – 14 fs), showing mostly the Kerr response. (d) The phase shift $\Delta\Phi(x,y,t_0$+14 fs), showing the Kerr response on the wings and the growing plasma phase shift in the center of the beam. (e) The phase shift $\Delta\Phi(x,y,t_0$+280 fs), showing the negative plasma phase shift long after the pump pulse and rotational response……..……..…93

Figure 5.6. Results in O_2 at a pump peak intensity of 89 TW/cm^2. (a) Measured spatiotemporal phase shift $\Delta\Phi(x,y_0,t)$. (b) An image of the pump spot at the gas target, showing that the Kerr response simply follows the pump intensity profile. (c) The phase shift $\Delta\Phi(x,y,t_0$ – 14 fs), showing mostly the Kerr response. (d) The phase shift

$\Delta\Phi(x,y,t_0+14$ fs), showing the Kerr response on the wings and the growing plasma phase shift in the center of the beam. (e) The phase shift $\Delta\Phi(x,y,t_0+350$ fs), showing the negative plasma phase shift long after the pump pulse and rotational response……94

Figure 5.7. Ionization yield (x) as a function of peak intensity for (a) Ar (red), Kr (green), Xe (blue); (b) N2 (black) and O2 (magenta). PPT [130] rates are shown as solid lines. TDSE calculations for Ar, Kr, and Xe are shown as closed circles [131]. Fits to a multiphoton ionization rate are shown as dashed lines…….…….96

Figure 5.8. Response during pump pulse. (a) The nonlinear refractive index as a function of time for peak intensity of 42 TW/cm2, below the threshold for ionization, and a fit to a Gaussian with FWHM 42 fs. (b) Nonlinear refractive index as a function of time and fits to the standard model (Kerr effect plus ionization) for Ar. The curves have been offset vertically for clarity. (c) Plot of Kerr index change (×) and plasma index change (+) from fits as a function of intensity in Ar (black), Kr (blue), and Xe (red). (d) Same as part (c) for N_2 (red) and O_2 (blue)…….…….99

Figure A.1 Diatomic molecule in an external pump electric field……101

Figure B.1 Diatomic molecule in an external probe electric field……105

Chapter 1: Introduction

1.1 Motivation and outline of the dissertation

Propagation of an intense, ultrashort laser pulse, is dominated by the propagation medium, which can both distort the laser pulse and leave the medium perturbed. A common type of pulse distortion is linear dispersion, arising from the frequency dependence of the linear response. Depending on the sign of the dispersion, the pulse can be spread or compressed temporally.

The lowest order nonlinear responses in a medium depend on the medium's symmetry properties. In an isotropic medium, the lowest order response is 3^{rd} order in the laser electric field, and includes the processes of self-focusing and self-phase modulation. Spatially, the 3^{rd} order nonlinear response leads to either self-focusing or self-defocusing (depending on the sign of the nonlinearity). Self-focusing, the most common process, which can depend on the electronic, rotational and vibrational responses, can initiate a runaway collapse process in which the beam focuses toward a singularity, a process arrested only when the local intensity is high enough for ionization and plasma generation, which defocuses the beam. Temporally, the third order nonlinear response is responsible for self-phase modulation, which adds new frequency components to the laser pulse; the bandwidth of the pulse can be significantly broadened. Other components of the third order response lead to generation of the 3^{rd} harmonics of the carrier frequency. At high laser intensities near the ionization threshold of the medium, the perturbative approach breaks down, and very high harmonics can be generated [1]

A particularly interesting and practical outcome of self-focusing and self-focusing arrest is the generation of femtosecond filaments. Such a laser filament is formed when a dynamic interplay occurs between self-focusing and plasma-induced defocusing, leading to propagation of a high intensity core over an extended range greatly exceeding the Rayleigh length, the natural scale length for diffraction. For near infrared pulses $\lambda <\sim 1\mu m$, filamentary propagation has been studied extensively [2,3]. Filamentation has found applications in the generation of terahertz radiation [4], high harmonic generation [5], and air lasing [6–8]. Supercontinuum generation [9] both in gases and solids has become an important method to generate laser pulses with extremely broad bandwidth.

Through generation of plasma and excitation of rotations, filamentation in air is shown to leave a column of heated gas behind [10], which causes long-timescale hydrodynamic response [11]. It is this hydrodynamic response [12–17] that is used to inscribe optical waveguides into air remotely.

With an eye on its applications for generation of air waveguides, in Chapter 2 we show that a train of ultrashort near-IR laser pulses can resonate with the rotational states of diatomic molecules such as N_2 and O_2, and cause them to become permanently aligned along the laser polarization axis. The pulse train deposits significant energy into rotations of the molecules, causing a level of gas heating and hydrodynamic response which can exceed that from filamentary plasma generation.

In Chapter 3, we describe our work to measure the electronic nonlinearity coefficients for air constituents and some wide bandgap solids at mid-IR wavelengths.

It has been anticipated that new regimes of laser filamentation are possible at longer wavelengths, such as in the mid- to long-wave infrared range ($\lambda \sim 1.5-10\mu m$), where beam collapse arrest may occur through harmonic walk-off rather than plasma-induced refraction [18]. Mid-IR filamentation plays a major role in the generation of coherent keV photon beams in high-pressure gas-filled capillaries [19] and broad mid-IR supercontinua in high-pressure gas volumes [20].

In Chapter 4 we measure the contribution of the adiabatic vibrational response to the instantaneous nonlinear response of diatomic molecules H_2 and D_2 , which, as the simplest molecules, provide a benchmark for theory and simulation. Finally in Chapter 5, we measure, for the first time, the absolute rates of ionization in noble gases, N_2 and O_2. An interesting outcome of these measurements is that the nonlinear response of the neutral atoms and molecules surviving past the ionization threshold is still approximately quadratic in the laser field, a result predicted by perturbation theory but now shown to still apply 2-3 orders of magnitude in intensity beyond it.

1.2 Linear and nonlinear response of media

We start with the electromagnetic wave propagation equation, with a polarization source term, **P**

$$\nabla^2\mathbf{E}-\frac{1}{c^2}\frac{\partial^2\mathbf{E}}{\partial t^2}=\frac{4\pi}{c^2}\frac{\partial^2\mathbf{P}}{\partial t^2}, \tag{1.1}$$

where $\mathbf{P}=\mathbf{P}_L+\mathbf{P}_{NL}$ is the sum of linear and nonlinear contributions. In general, for a spatially local but possibly temporally nonlocal response, one must use $\tilde{\mathbf{P}}_L(\mathbf{r},\omega)=\chi(\omega)\tilde{\mathbf{E}}(\mathbf{r},\omega)$, where tilde quantities are Fourier transforms of the time dependent fields. However, far from material resonances, the linear response is nearly instantaneous, with $\mathbf{P}_L(\mathbf{r},t)=\chi\mathbf{E}(\mathbf{r},\mathrm{t})$ modeling the linear response of the medium and with $\chi=\chi(\omega_0)$ very weakly dependent on the central frequency of the laser bandwidth. Similarly, for the class of electronic nonlinearities associated with electron orbitals $\mathbf{P}_{NL}$ is likewise a near-instantaneous function of $\mathbf{E}(\mathbf{r},\mathrm{t})$ far from resonances. Equation (1.9) becomes

$$\nabla^2\mathbf{E}-\frac{n^2}{c^2}\frac{\partial^2\mathbf{E}}{\partial t^2}=\frac{4\pi}{c^2}\frac{\partial^2\mathbf{P}_{NL}}{\partial t^2}. \tag{1.2}$$

where $n^2=1+4\pi\chi$ is the index of refraction. In atoms such as noble gases only electronic nonlinearities contribute to $\mathbf{P}_{NL}$. In linear diatomic molecules such as N_2 and H_2 electronic, rotational and vibrational degrees of freedom can contribute to the nonlinear polarization. In the lowest order (third order) isotropic nonlinearities considered in this thesis, which drive self-focusing and self-phase modulation, $\mathbf{P}_{NL}^{elec}=\chi^{(3)}\left|\mathbf{E}(\mathbf{r},t)\right|^2\mathbf{E}(\mathbf{r},t)$ and $\mathbf{P}_{NL}^{rot}(\mathbf{r},\mathrm{t})=(\int_{-\infty}^{t}d\tau\,R(t-\tau)\left|\mathbf{E}(\mathbf{r},\tau)\right|^2)\,\mathbf{E}(\mathbf{r},t)$ for the

electronic and rotational contributions to the total nonlinear polarization, where $\chi^{(3)} = \chi^{(3)}(-\omega_0;\omega_0,-\omega_0,\omega_0)$ is the appropriate third order nonlinear susceptibility [21] and *R* is a time-domain response function describing the cumulative Raman excitation of rotational quantum states during the pulse [22]. The contribution of vibrations is somewhat more complex and is covered in Chapter 4. While vibrational nonlinearities play little role in atmospheric filamentation using near-IR lasers, they can play a significant role in mid-IR propagation [23]

1.3 Laser system

Titanium:Sapphire is the most widely used laser gain medium in ultrafast laser labs today. Ti:Sapphire crystals, usually pumped with λ~0.5μm green pulses derived from frequency doubled ~1 μm range lasers, can amplify over a bandwidth λ=680 nm - 1100nm, ensuring support of ultrashort pulse structure, if desired. Alternatively, for CW operation, the wide bandwidth supports broad tunability.

For ultrashort pulses Ti:Sapphire-based oscillator cavities support mode-locking over a wide bandwidth. The most common mode-locking mechanism is Kerr lens mode locking, pioneered by Spence, Kean and Sibbett [24]. Here, the oscillator cavity has been adjusted so that nonlinear self-focusing in the laser material leads to the lowest loss round-trip propagation path in the cavity, while linearly propagating modes experience the greatest loss. Hence, the shortest pulse—the modelocked pulse, which is also the most intense—is the only one to survive cavity losses and it commandeers all of the laser gain [25,26]. If necessary, pulses picked from the train of ultrashort laser pulses emerging from the oscillator can be used as a seed for further stages of amplification.

In our lab, we use a commercial oscillator[1] to generate a train of broadband (~65 nm) pulses with repetition rate of 80 MHz. The oscillator is pumped by a single mode 5 W green laser (λ=532 nm). The energy of each oscillator pulse is ~5 nJ—too small to cause any nonlinear effects in dilute media such as gases. In order to observe nonlinear effects in dilute media, the oscillator pulses need to be amplified in a high gain (~10^6) Ti:Sapphire regenerative amplifier (RGA), where Pockels cells are used to trap (switch in) 1 in every 80000 seed pulses. To avoid catastrophic nonlinear self-focusing in the RGA and in any subsequent amplifiers, the seed pulses are stretched in temporal duration from ~40fs to ~200ps using a grating stretcher. After stretching, the seed pulse is switched into the RGA cavity using a Pockels cell. It then reflects back and forth ~12-25 times inside the RGA cavity, picking up energy from amplification in the pumped Ti:Sapphire crystal (pumped by a Q-switched, frequency doubled λ~1μm laser), until it is ejected (switched out) from the cavity by another Pockels cell after reaching an energy of multiple mJ, depending on the laser system (see below). The pulse temporal stretch is then reversed using a grating compressor, yielding ~40 fs pulses at several energies (see below). The stretch-amplify-compress processes is called Chirped Pulse Amplification (CPA) [27] and is the basis of all modern high intensity, short pulse laser systems. Figure 1.1(a) depicts a schematic of a diffraction grating-based pulse stretcher. It can be seen that the distance of the second lens to the second grating is smaller than that of first lens to the first grating. Hence the red side of the seed spectrum takes a shorter path compared to the blue side, causing the seed pulse to be positively chirped (red temporally leading blue)

[1] Coherent Mantis

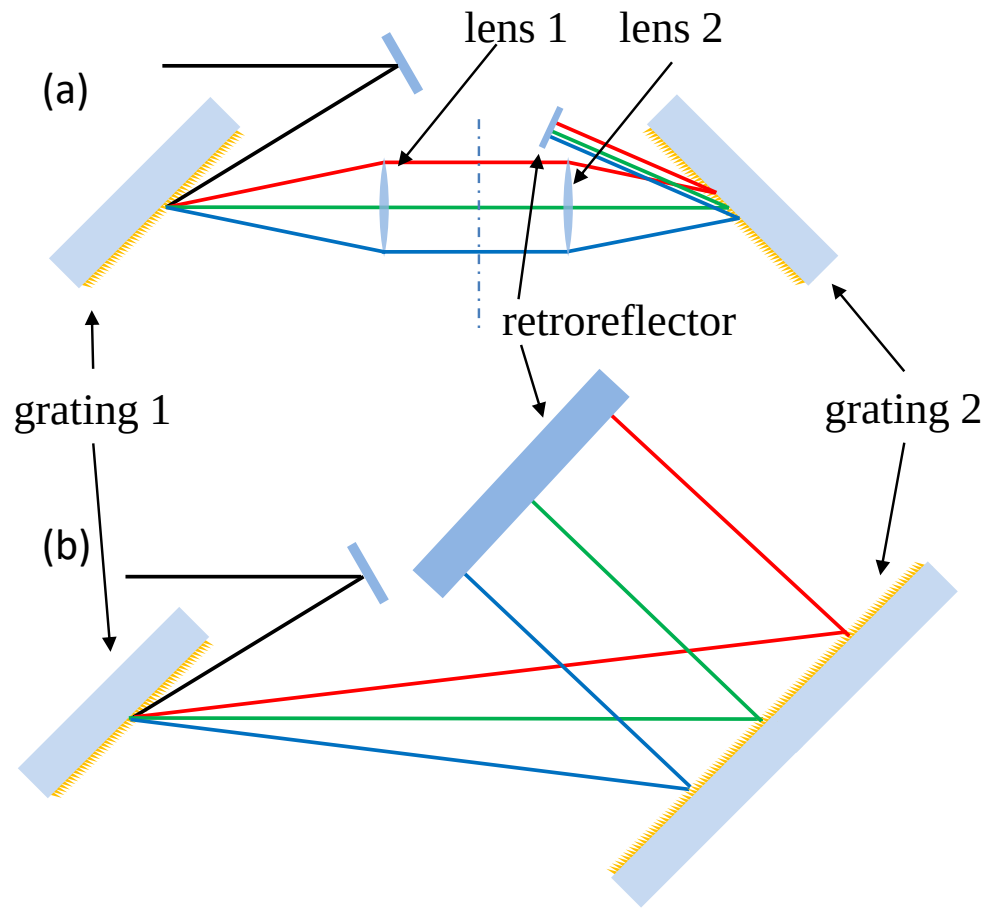

Figure 1.1. Schematic design of **(a)** Pulse stretcher. The distance of lens 2 and grating 2 is smaller than that of lens 1 and grating 1, thus the redder parts of the spectrum encounter smaller delay compared to the bluer side. This results in the pulse to be positively chirped. **(b)** Pulse compressor. The redder side of the spectrum encounters longer delay compared to the bluer side, thus the pulse is negatively chirped.

from ~20 fs to ~200 ps in a typical CPA stretcher. During amplification, normal group velocity dispersion in the Ti:Sapphire rod and Pockels cells leads the pulse to be further positively chirped on each RGA cavity round trip. After the RGA output, a pulse compressor depicted in Fig 1.1(b) compensates the positive chirp of the stretcher and amplifier by introducing negative chirp to the laser pulse.

During the early work done in this dissertation, a commercial regenerative amplifier[1] capable of producing 3.5 mJ, 40 fs pulses at 1 kHz was used as an 800 nm

[1] Coherent Legend Elite

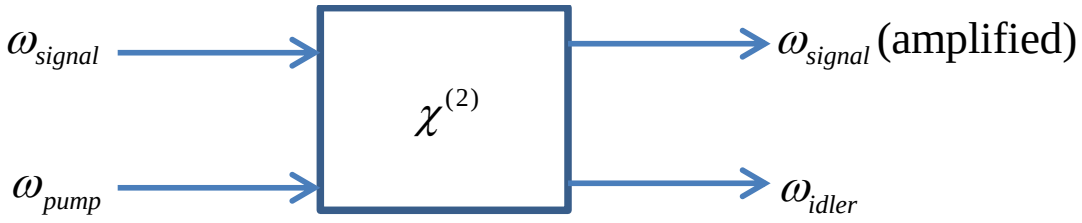

Figure 1.2. Parametric gain in a $\chi^{(2)}$ material where a weak input signal at ω_{signal} is amplified by splitting photons at ω_{pump} into two photons ω_{signal} and ω_{idler} such that $\omega_{pump} = \omega_{signal} + \omega_{idler}$.

ultrashort laser source. This laser was later replaced with another model[1] in which, prior to compression, the RGA output was sent to a single pass amplifier to double its energy. This laser produced 10 mJ, 38 fs pulses at 1 kHz, and was used in later work done in this dissertation.

1.4 Mid-infrared optical parametric amplifier

Optical parametric amplifiers (OPA's) are used to convert the wavelength of ultrafast pump lasers (with fixed wavelength) into regions of spectrum where ultrafast laser gain media are not readily available, such as mid-infrared wavelengths. A tunable commercial[2] OPA and difference frequency generator (DFG) were used in parts of the work presented in this dissertation to shift the center wavelength of our Ti:Sapphire laser source into the mid-IR range of 1.1 μm - 11 μm. The OPA has three stages: white light generation and pre-amplification, second stage amplification and power amplification. In the OPA, β-barium borate (BBO, a negative uniaxial non-centrosymmetric nonlinear material) is used as the medium for parametric[3] gain through difference frequency generation. In the first stage, ~10 μJ of 800 nm, 38 fs,

[1] Coherent Legend Elite Duo
[2] Light Conversion HE-TOPAS-Prime
[3] A parametric nonlinear process is a process in which the energy state of the material after the process is the same as the initial state of material, thus no net energy is exchanged with the medium, e.g.,

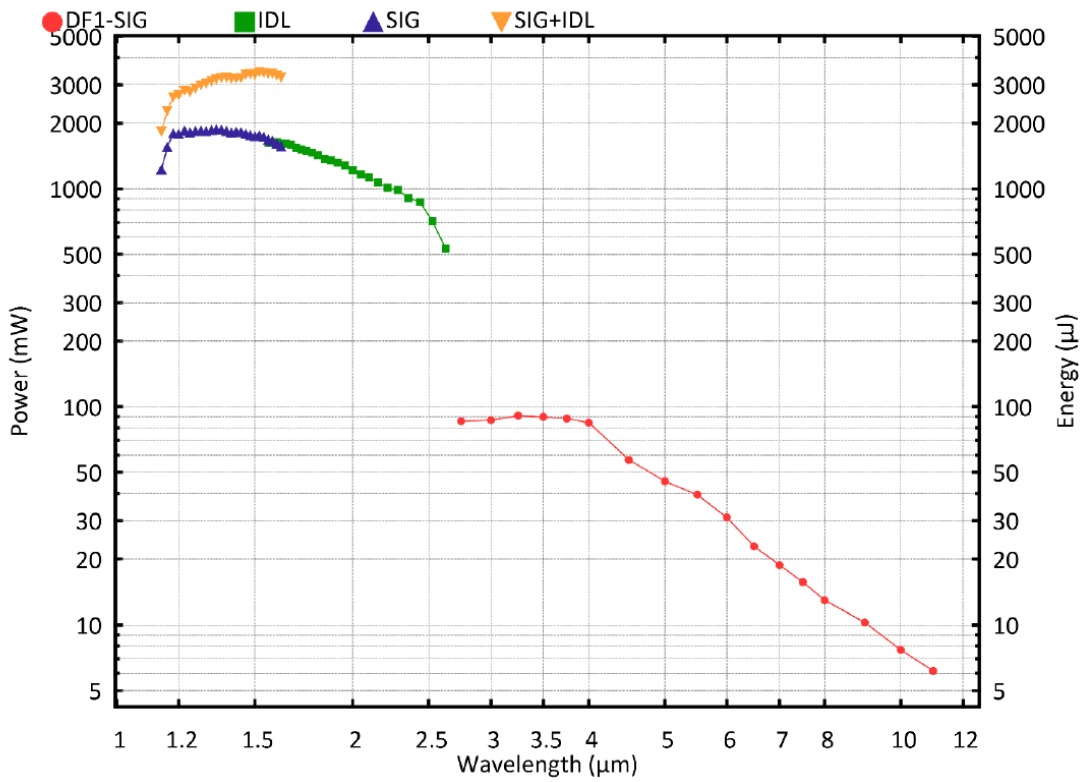

Figure 1.3. The output energy of OPA and DFG units when pumped by a 8 mJ, 38 fs Ti:Sapphire laser.

vertically polarized laser pulse is focused in 3 mm of sapphire. Self-phase modulation in the sapphire produces a broadband supercontinuum spanning from 450 nm to 1600 nm. The supercontinuum is heavily chirped by transmitting it through ~1 cm of ZnSe. The 1.1 µm to 1.6 µm part of the supercontinuum spectrum is used as the weak signal in the first stage of parametric amplification: a computer controlled delay line adjusts the delay of pump ($\omega_{pump} = 800\text{nm}$) so that it overlaps with the part of the spectrum of the signal, the user wants to amplify. The vertically polarized signal and horizontally polarized pump are focused through a BBO crystal, with the pump and signal being non-collinear. The angle of the BBO crystal is tuned by a computer-controlled

second harmonic generation. In non-parametric process, energy is exchanged with the medium, e.g., Raman process [26].

rotation stage to satisfy type II phase matching for the user specified wavelength. The idler and the used pump are blocked whereas the amplified signal is amplified again in a second stage, using a fresh pump. Once again, the idler and the used pump are blocked after the second stage amplification. The amplified signal goes through a final amplification stage, where pump and signal are collinear, resulting in collinearly propagating signal and idler. The collinearly propagating signal and idler can be separated with broadband dichroic mirrors, and either the signal (1.1 μm – 1.6 μm, vertically polarized) or idler (1.6 μm – 2.6 μm, horizontally polarized) can be used as pump in mid-IR ultrafast experiments.

If longer wavelengths are required, a difference frequency generation step can be performed between the signal and idler, extending the wavelength range up to 11 μm. The difference frequency generation is done by type I phase matching in $AgGaS_2$ (silver thiogallate or AGS, negative uniaxial $\chi^{(2)}$ material). Figure 1.3 shows the available pulse energy from the OPA and DFG units when they are pumped by a ~8 mJ of 800 nm, 38 fs Ti:Sapphire laser at 1 kHz repetition rate. For an OPA, the Manley-Rowe relations [26] state that the rate at which pump photons are consumed, is equal to the rate at which new down-converted photons are generated. The energy of the photons for longer wavelengths is lower than that of shorter wavelengths, thus as the difference between the energy of the pump photons and the down converted photons becomes larger, the energy conversion efficiency for the down conversion process declines, as seen in Fig 1.3.

1.5 **Ultrafast time-resolved measurements of laser-induced nonlinearity**

As discussed earlier, the lowest order third order nonlinearities are the most important for the experiments of this dissertation. A significant part of this dissertation will cover single-shot ultrafast time-resolved measurements of these nonlinearities. Our measurement technique is single-shot supercontinuum spectral interferometry [28–30], which we will describe shortly.

Due to its simplicity, the single beam z-scan technique [31] is a widely used method for measuring the nonlinear refractive index and nonlinear absorption in solids and liquids. A sample is moved through the focus of the laser pulse. The nonlinearity and beam propagation changes the spatial profile of the beam after the sample in the far field, where the beam profile is recorded. The researcher can measure the nonlinear refractive index of the sample based on the changes in the beam profile recorded in the far field. A drawback of this technique (and its variants) is that *a priori* assumptions regarding the type of the nonlinearities involved and their time dependence as well as the spatial and temporal profile of the laser pulse are needed in order to simplify the nonlinear laser propagation calculations required by the analysis.

Strong pump-weak probe techniques are improvements to single beam methods such as z-scan: When the intensity of the probe laser field is low enough it can be viewed as a perturbation to the pump electric field. For example, let us assume $\mathbf{E}_e(t) = A_{e,x}(t)\exp\left(i\mathbf{k}_e \cdot \mathbf{r} - i\omega_e t\right)\hat{\mathbf{x}}$ and $\mathbf{E}_p(t) = A_{p,x}(t)\exp\left(i\mathbf{k}_p \cdot \mathbf{r} - i\omega_p t\right)\hat{\mathbf{x}}$ (subscript e for "excitation" and p for "probe") be the electric fields of the pump and probe

respectively, propagating in an instantaneous isotropic $\chi^{(3)}$ medium. The induced dipole moment due to the external fields can be written as

$$P_x = \chi_{xx}^{(1)}\left(E_e + E_p\right) + \chi_{xxxx}^{(3)}\left(E_e + E_p\right)^3. \tag{1.3}$$

Most pump-probe experiments are designed such the pump and probe can be separated spatially ($\hat{\mathbf{k}}_e \neq \hat{\mathbf{k}}_p$ for non-collinear pump and probe) or filtered by color. Ignoring higher order terms in E_p, the induced dipole moment oscillating at frequency ω_p and propagating in direction $\hat{\mathbf{k}}_p$ is

$$P_{x,p} = \chi_{xx}^{(1)}E_p + \chi_{xxxx}^{(3)}E_e^2 E_p. \tag{1.4}$$

In a well-designed pump-probe experiment, the interaction length between pump and probe through the material is small enough (usually through designing the pumped material to be thin) so that there is no need to include *nonlinear propagation effects* due to the pump—the pump imprints a phase on the weak probe (through the nonlinear material response) which simply propagates linearly after the interactions.

The second improvement is the added degree of freedom to make direct observations in the temporal domain. One approach is the multi-shot pump-probe method, where the time delay between the pump and a weak ultrashort probe is varied shot-by-shot, allowing reconstruction of the material's nonlinear response. This method is not useful when there are significant shot-to-shot variations in laser parameters, resulting in even larger fluctuations in the material response. Such considerations led to the development of single-shot spectral interferometric techniques.

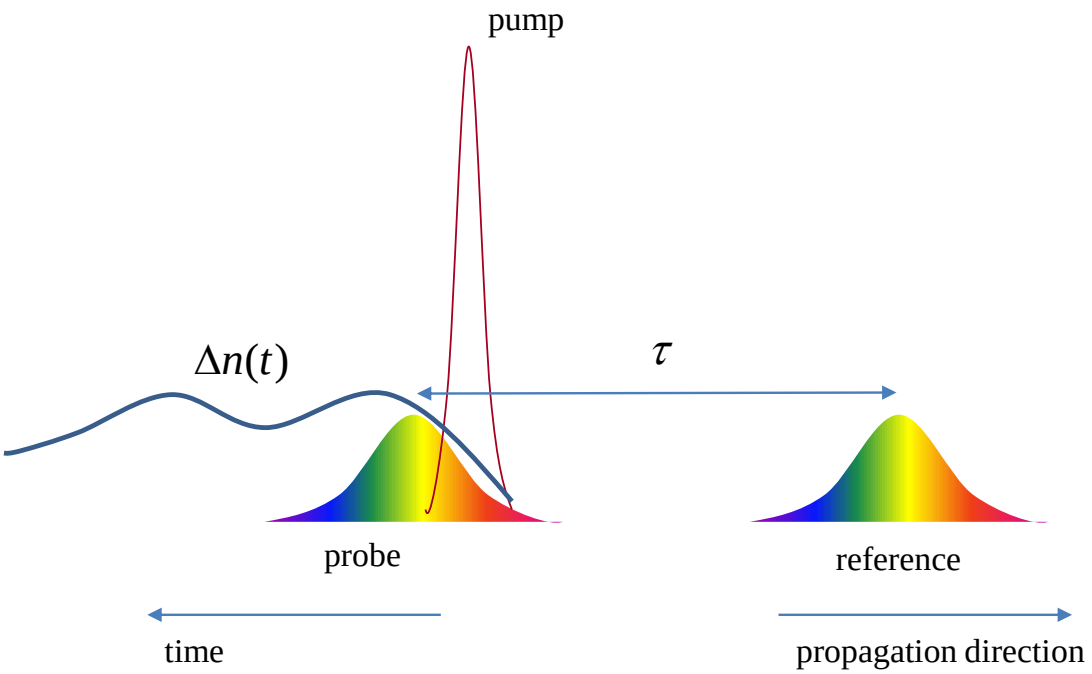

Figure 1.4 Strong pump cause a time dependent change in refractive index of the medium it propagates through. The probe overlaps in time with this refractive index change and acquires a phase shift.

1.6 Single-shot supercontinuum spectral interferometry

In single shot supercontinuum spectral interferometry (SSSI) two identical chirped broadband and low energy laser pulses (reference and probe) propagate collinearly through interaction region. The reference precedes the probe by τ, whereas the strong pump and probe overlap in time, as shown in Fig. 1.4. Each 'color' of the probe interacts with a separate time slice of the material response, acquitting phase shift. After rejecting the pump, the probe and reference interfere in spectral domain in an imaging spectrometer.

Let $E_p(\mathbf{r}_\perp, t)$ and $E_{ref}(\mathbf{r}_\perp, t)$ be the probe and the reference in time domain respectively, where $\mathbf{r}_\perp = (x, y)$ is the transverse spatial dimension. The strong pump

induces a change in the refractive index $\Delta n(\mathbf{r}_\perp, z, t)$ which imparts a time dependent phase shift

$$\Delta\Phi(\mathbf{r}_\perp, t) = k_0 \int \Delta n(\mathbf{r}_\perp, z, t) dz \approx k_0 L_{eff} \Delta n(\mathbf{r}_\perp, t) \tag{1.5}$$

on the probe, where L_{eff} is the effective medium length and k_0 is the probe central wavenumber. The imaging spectrometer enables resolving the spatial dependence of the probe phase shift along a 1D slice, $\mathbf{r}_{\perp,0} = (x, y_0)$. Dropping the spatial dependence

$$E_p(t) = E_{ref}(t - \tau)\, \mathrm{e}^{i\Delta\Phi(t)} \tag{1.6}$$

In the Fourier domain let us denote $\tilde{E}_{ref}(\omega) = \left|\tilde{E}_{ref}(\omega)\right| \mathrm{e}^{i\phi_s(\omega)}$, $\tilde{E}_p(\omega) = \left|\tilde{E}_p(\omega)\right| \mathrm{e}^{i[\omega\tau + \phi_s(\omega) + \Delta\varphi(\omega)]}$, where $\phi_s(\omega)$ is the spectral phase of the reference, $\Delta\varphi(\omega)$ is the phase shift imparted by the material response in the spectral domain[1]. On the spectrometer we observe the interference between probe and reference

$$\begin{aligned} &\left|\tilde{E}_p(\omega) + \tilde{E}_{ref}(\omega)\right|^2 = \\ &\left|\tilde{E}_p(\omega)\right|^2 + \left|\tilde{E}_{ref}(\omega)\right|^2 + \\ &+2\left|\tilde{E}_p(\omega)\right|\left|\tilde{E}_{ref}(\omega)\right| \cos\left(\omega\tau + \Delta\varphi(\omega)\right). \end{aligned} \tag{1.7}$$

Due to the time delay τ between probe and reference, interference fringes appear $\cos\left(\omega\tau + \Delta\varphi(\omega)\right)$ in the spectral domain. We use these fringes to extract the phase shift $\Delta\varphi(\omega)$ using Takeda method [32]. Furthermore $\left|\tilde{E}_{ref}(\omega)\right| = \sqrt{S_{ref}(\omega)}$ and $\left|\tilde{E}_p(\omega)\right| = \sqrt{S_p(\omega)}$ are measured directly by taking the spectra of the reference

[1] Note that $\Delta\varphi(\omega) \neq \mathcal{F}\left\{\Delta\Phi(t)\right\}$.

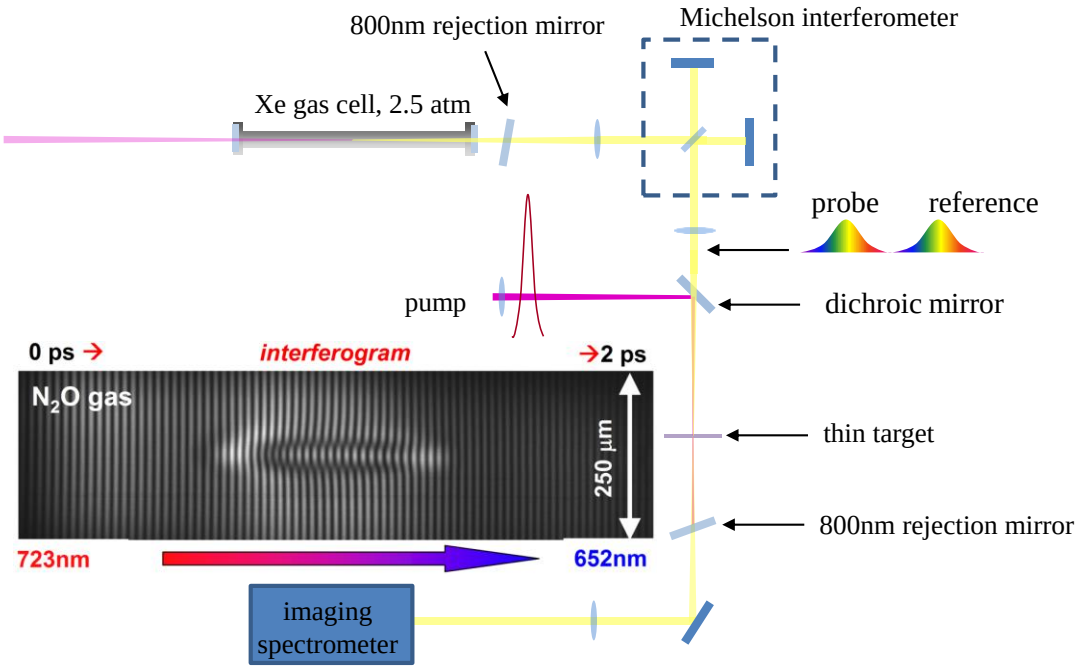

Figure 1.5 Schematic of single shot spectral interferometry setup. The inset shows an example of interference pattern (data taken for publication of [29]) observed in the spectral domain due to time separation between reference and probe.

$S_{ref}(\omega)$ and probe $S_p(\omega)$. An *in situ* method for measuring the spectral phase of the reference $\phi_s(\omega)$ is discussed in detail in [30].

Using Eq. (1.6) we can now derive time domain phase through

$$\Delta\Phi(t) = \mathrm{Im}\left\{\ln\left[\frac{\mathcal{F}^{-1}\left\{\left|E_p(\omega)\right|e^{i[\varphi_s(\omega)+\Delta\varphi(\omega)]}\right\}}{\mathcal{F}^{-1}\left\{\left|\bar{E}_p(\omega)\right|e^{i\varphi_s(\omega)}\right\}}\right]\right\}, \tag{1.8}$$

where $\mathcal{F}^{-1}\{\cdot\}$ denotes the inverse Fourier transform.

This is the basis of the SSSI [28] technique that we use extensively in this dissertation.

Experimentally in order to generate the probe and reference, we focus ~100 µJ of 40 fs Ti:Sapphire laser pulse at f/150 into a 40cm long gas cell filled with 2.5 atm of

xenon. Filamentation in the gas cell generates a supercontinuum spanning from 400nm-850nm. A pump rejection mirror discards the part of the spectra above 700nm. The transmitted supercontinuum is recollimated using a lens. The combination of the lenses before and after the gas cell form a down-collimation telescope, resulting in a collimated supercontinuum with ~2 mm waist full width at half maximum (FWHM). The supercontinuum is split into copropagating probe and reference by a Michelson interferometer. The delay arm of the Michelson interferometer is set so that the probe precedes the reference by ~2 ps. The probe and reference are focused into the test vacuum chamber where they focus in the sample under test.. Furthermore an intense pump focuses on the same spot.

Prior to the focusing of the 800nm beam into the xenon gas cell, we have a variable delay line which we adjust so that the pump and the probe arrive at the sample at the same time. Furthermore, a $\lambda/2$ wave plate adjusts the polarization of the probe/reference with respect to the pump. After the interaction region, both of the pump and probe/reference diverge. At a point where the pump has diverged enough, we reject it so that it cannot interact with the probe at any point downstream out of the vacuum chamber.

The interaction region between pump and probe is magnified and imaged on the (vertical) slit of an imaging spectrometer, where one spatial and one spectral (or as we see later temporal) dimensions are resolved.

Chapter 2: Quantum control of molecular gas hydrodynamics

2.1 Introduction

Significant hydrodynamic perturbation of solids, liquids, and non-dilute gases by nonlinear absorption of intense laser pulses typically proceeds by localized plasma generation, which provides the pressure and temperature gradients to drive both mass motion and thermal transport. This is typically assumed to be the case for femtosecond filaments in gases, where depletion of the laser pulse energy due to absorption limits their ultimately achievable length [2] and where the thermal energy deposited in the gas can result in sound wave generation [12,33–39] followed by a gas density depression or 'hole' that can persist on millisecond timescales [12,36,37]. Recently it was shown that this density hole can affect filamentation at kilohertz repetition rates by acting as a negative lens [36] and can steer filaments [12]. It may even play an important role in filament-triggered electrical discharges [34,35]. New applications such as high average power laser beam guiding and remote generation of lensing structures in the atmosphere [37] can be enabled by control of energy deposition in gases by femtosecond laser pulses.

Previous work on energy deposition by filamentation has emphasized laser absorption due to atomic or molecular ionization and heating of free electrons [34–36,40]. In this chapter, we first show that molecular rotational heating is the dominant source of energy absorption in air filaments produced by single pulses. We then show that significantly greater gas heating can be generated by coherently and resonantly exciting a molecular rotational wave packet ensemble by a sequence of short non-

ionizing laser pulses separated by the rotational revival period [41,42]. By 'wave packet', $|\psi_{rot}\rangle = \sum_{j,m} a_{j,m} |j,m\rangle \exp\left(-i\frac{E_j}{\hbar}t\right)$, we mean the coherent superposition of angular momentum eigenstates $|j,m\rangle$ excited by the laser pulse(s), where *j* and *m* are quantum numbers for square of the total rotational angular momentum and for the component of angular momentum along the laser polarization, $E_j = \frac{\hbar^2}{2I} j(j+1)$ is the energies of state $|j,m\rangle$, *I* is the moment of inertia of the molecule, and $a_{j,m}$ is the probability amplitude of finding the molecule in the $|j,m\rangle$ eigenstate. We note that since all of $\omega_j = \frac{\hbar}{2I} j(j+1)$ are related to ω_1 by integers, $|\psi_{rot}\rangle$ is periodic, with fullrevival period $T_r = \frac{2\pi I}{\hbar}$. The structure of this integer relationship also allows fractional revivals at $T_r/4$, $T_r/2$, and $3T_r/4$ [29]. Gas heating occurs by collisional de-excitation and decoherence of the ensemble, leading to significant hydrodynamic response. Gas heating can be equivalent to that driven by filament plasma heated up to ~50 eV, greatly in excess of typical filament plasma electron temperatures of less than 5 eV. Moreover, we show that it is possible to deplete a population of rotationally excited molecules before the wave packet collisionally decoheres, suppressing gas heating. These results point to new ways of precisely controlling gas density profiles in atmospheric propagation [37], and have practical implications for schemes using pulse trains to enhance supercontinuum generation, filament length and plasma density [43,44], and THz amplification [41]. Other novel extensions are also suggested. Isotope-selective pumping of rotational population was measured

recently at low temperatures and pressures [45]. The interferometric technique employed here, combined with optical centrifuge techniques [46,47] or chiral pulse trains [48], could find use in studying laser-induced gas vortices [49].

Here, laser excitation/de-excitation of the molecular ensemble is monitored by direct interferometric measurement of the gas density depression produced by subsequent heating of the gas. A short laser pulse is absorbed by exciting rotational population by a two-photon Raman process [50,51]. As explained in Chapter 4, the bandwidth of a 40-100fs laser pulse is not enough to excite vibrational levels in either nitrogen or oxygen (0.3eV and 0.2eV respectively), thus the laser pulse cannot excite vibrational states of the gas. Gas heating occurs from thermalization of the pumped rotational ensemble, which occurs over hundreds of picoseconds [52]. Previously it was shown [36] that after ~1 μs, a pressure-balanced quasi-equilibrium forms where the gas density profile is given by $\Delta N \approx -N_0 \Delta T/T_0$, where N_0 and T_0 are the background density and temperature and ΔT is the temperature increase from the laser absorption. Thus, the initial hole depth $|\Delta N|$ is proportional to the absorbed energy. The temperature profile, and therefore the density depression, then decays on millisecond timescales by thermal diffusion [36]. Even after many microseconds of diffusive spreading of the density hole [36], the peak depression is still proportional to the initial temperature, as verified in Fig. 1.1(a), in which a fluid code simulation [36] demonstrates the linear dependence of relative hole depth after 40 μs of evolution vs. the initial gas temperature change in nitrogen.

2.2 Experimental setup

A diagram of the experimental setup is shown in Fig. 2.1. The laser pump consisted of a single pulse, double pulse, or a train of four 800nm, ~110 fs Ti:sapphire pulses generated with a 4-pulse Michelson interferometer [53] ("pulse stacker"). The beam was focused at f/44 by a lens into a chamber filled with various gases, to a vacuum beam waist FWHM of 33μm and a confocal parameter of $L = 2z_0 = 6.2\text{mm}$. In all of the experiments, the laser was operated at 20Hz to avoid cumulative effects of long timescale density depressions caused by previous pulses [36]. A continuous wave helium-neon laser at λ = 632.8 nm was used to interferometrically probe the 2D gas density profile. A plane at the pump beam waist was imaged through a folded wavefront interferometer onto a CCD camera. Pump-induced changes in the gas density cause phase shifts $\Delta\phi(x, y)$ in the *z*-propagating probe that are found by Fourier analysis of the interferogram [36]. Temporal gating of the probe pulse was achieved by triggering the CCD camera's minimum ~40 μs wide electronic shutter to include the pump pulse at the window's leading edge. Before phase extraction, 50 interferograms were averaged in order to improve the signal-to-noise ratio [54]. This reduced the RMS phase noise to ~6 mrad, enabling measurement of relative gas density changes $|\Delta N/N|$ as small as 10^{-4}. The probe interaction length in the pump-heated gas is the pump beam confocal parameter, $L \approx 6.2\text{mm}$. The change in refractive index of a gas varies with its density as $\Delta n/(n_0 - 1) = \Delta N/N_0$ [55], where n_0 and $N_0 \approx 2.47\times10^{19}\,\text{cm}^{-3}$ are the refractive index and number density of the gas at standard temperature and pressure. For the probe beam passing through the heated gas column we have $\Delta\phi = kL\Delta n$ where $k = 2\pi/\lambda$ is

its wave number and L is the propagation length. The gas density depression profile is then given by $\Delta N(x,y) = \Delta\phi N_0 / \left[(n_0 - 1)kL\right]$.

2.3 Experimental results and discussion

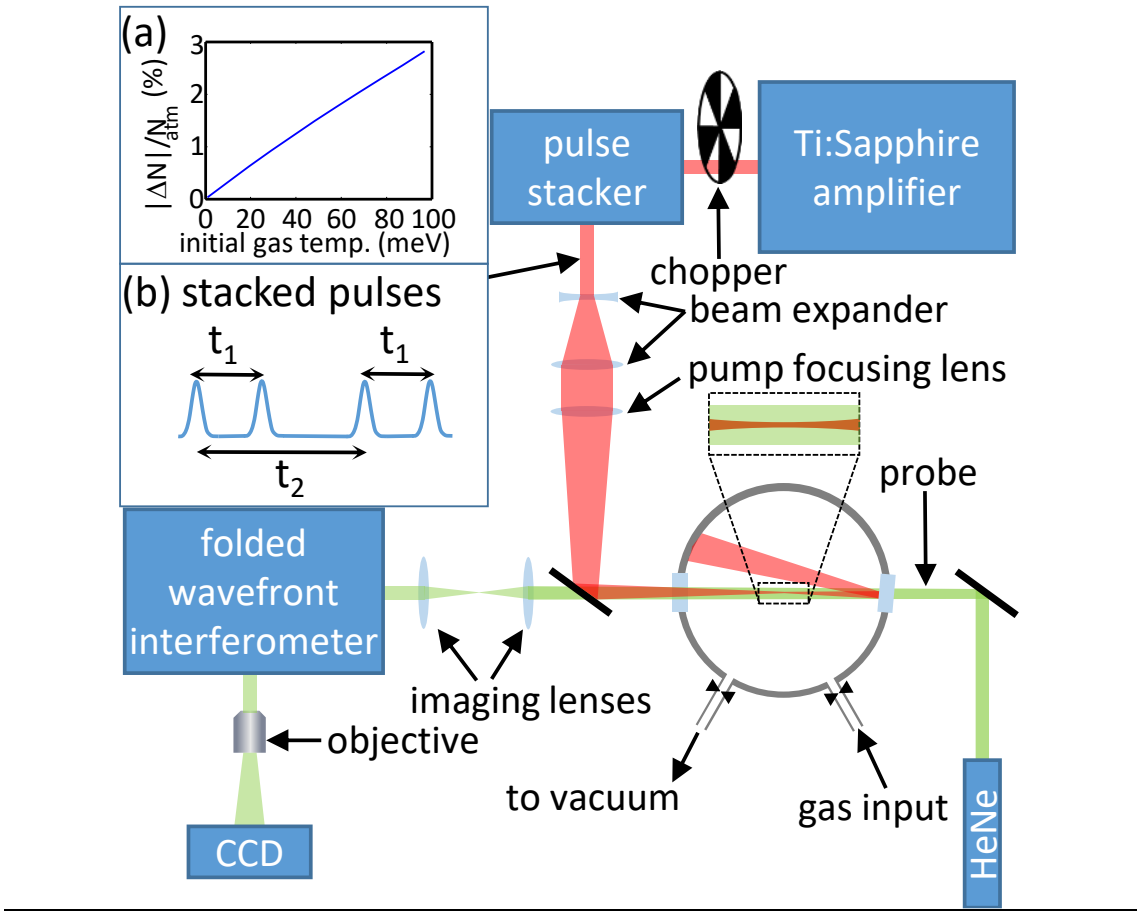

Figure 2.1. Experimental setup for measuring the 2D density profile of the rotationally excited gas at the pump beam focus. The chopper provides alternating pump on/off for background subtraction. **(a)** Simulation of hole depth vs. initial temperature showing that density hole depth is an excellent proportional measure of initial gas heating. **(b)** Scheme for (t_1, t_2) delay scan of pulses from pulse stacker.

In a preliminary experiment, we examined rotational absorption of single 110 fs pulses with energies ranging from 20 μJ to 500 μJ, Figure 2 shows the peak relative density hole depth $\left|\Delta N_{peak}\right| / N_0$, measured at the center of the profile, as a function of the vacuum peak intensity. Measurements are shown for 1 atm N_2, O_2, Ar, and air. As

discussed above, $\left|\Delta N_{peak}\right| / N_0$ is proportional to the laser energy absorption and initial gas temperature change. It is seen that its power dependence is quite different for the diatomic gases and Ar. For peak pump intensities of 40 TW/cm^2, below the ionization threshold of argon, we measured induced density depressions in all the diatomic gases, but none in argon to within our measurement uncertainty. At intensities below the ionization threshold, the energy absorbed by N_2 and O_2 has a roughly quadratic dependence on intensity, as expected for two-photon Raman absorption [38]. The curves deviate from the quadratic dependence at higher intensity, where absorption due to ionization strongly contributes. In all gases, saturation is observed at high pulse energy, which we attribute to the limiting of the laser intensity due to plasma defocusing [2]. Notably, our results show that at typical femtosecond filament clamping intensities of ~50 TW/cm^2, the greatly dominant source of laser energy deposition in molecular gases is rotational absorption and *not* ionization and plasma heating.

To calculate rotational absorption, we numerically solve for the evolution of the density matrix $\boldsymbol{\rho}$ describing the ensemble of molecules, which are assumed to be rigid rotors [41,56,57],

$$i\hbar \frac{d\boldsymbol{\rho}}{dt} = \left[\mathbf{H}, \boldsymbol{\rho}\right] \tag{2.1}$$

where [,] denotes the commutator between operators, and $\mathbf{H} = \mathbf{H}_0 + \mathbf{H}_{opt}$ is the total Hamiltonian composed of $\mathbf{H}_0 = \mathbf{J}^2 / 2I_{\mathbf{M}}$ and the interaction between the optical field and the molecules, $\mathbf{H}_{opt} = -\frac{1}{2}\mathbf{p} \cdot \mathbf{E}(t)$. Here $\mathbf{J}$ is the rotational angular momentum operator, I_{M} is the moment of inertia of the molecule, $\mathbf{p}$ is the induced dipole moment

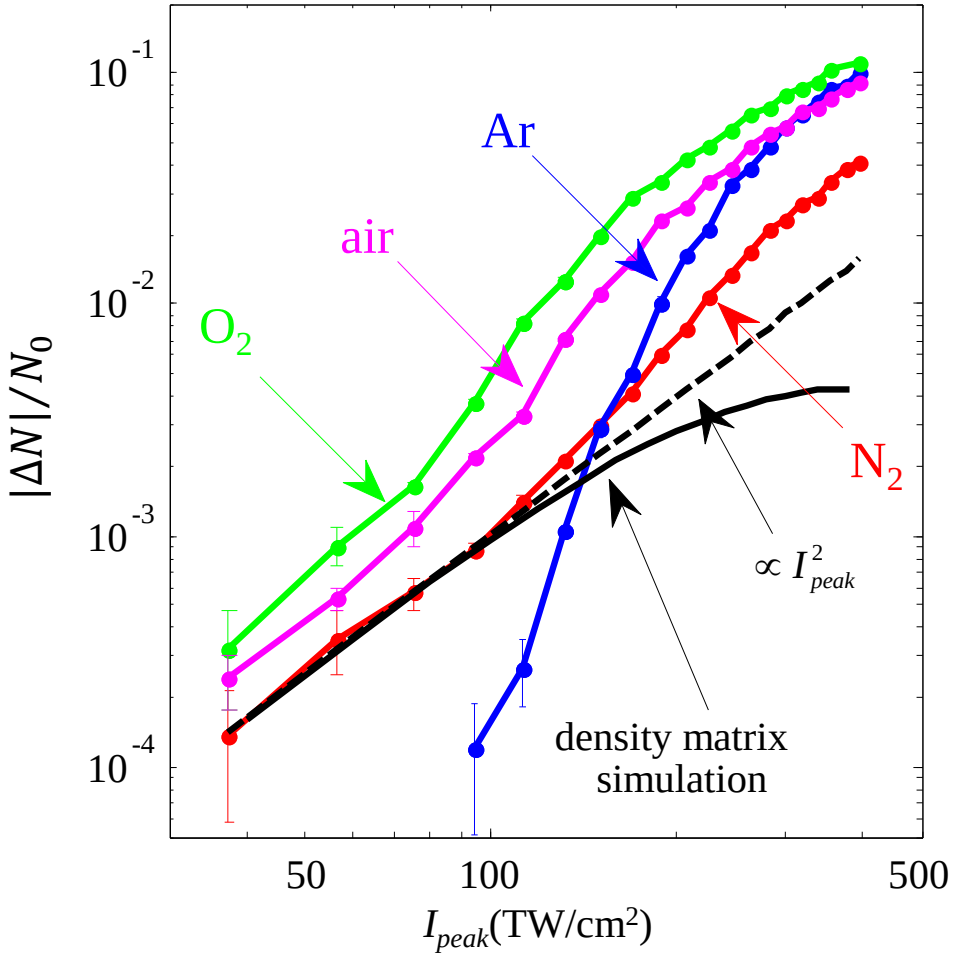

Figure 2.2. Relative density depression (proportional to heating) measured at 40μs delay due to single-pulse (110 fs FWHM) gas heating versus pump intensity at focus. In argon, plasma generation from multiphoton ionization and tunneling is the only source of gas heating, whereas in diatomic molecules, rotational excitation enables nonlinear absorption below the ionization threshold. The solid black line shows a density matrix calculation of the rotational absorption in N2 and the dashed line is a classical calculation using Eq. (2.3). The experimental points deviate from the density matrix simulation at higher intensities due to ionization and plasma absorption, which is not modeled here.

operator, and $\mathbf{E}(t)$ is the time dependent electric field interacting with the molecule. For a series of co-polarized optical pulses as used in our experiment, selection rules dictate that the interaction with the optical field only couples states with $\Delta j = \pm 2$ or 0 and $\Delta m = 0$. Initially at room temperature the rotational states are thermally populated,

with the Boltzmann distribution peaking at approximately j_{max}~10 in N_2. The initial density matrix is $\rho^{(0)}_{jmj'm'} = D_j \delta_{jj'} \delta_{mm'} \exp\left(-E_j / k_B T_0\right) \Big/ Z$, where $E_j = hcBj(j+1)$ is the rotational energy of j^{th} state, $B = \hbar / \left(4\pi c I_M\right)$ is the rotational constant (2.0 cm^{-1} for N_2 [58]), k_B is Boltzmann's constant, $Z = \sum_k D_k (2k+1) \exp\left(-E_j / k_B T_0\right)$ is the partition function, and D_j is a statistical weighting factor depending on the symmetries of the molecule and its nuclear spin statistics.

For N_2, D_j = 6 for j even and D_j = 3 for j odd. The initial average rotational energy per molecule is $Tr\left(H_0 \boldsymbol{\rho}^{(0)}\right) = k_B T_0$ where *Tr* is the trace operation. The change in average rotational energy ΔE per molecule (or the temperature change $k_B \Delta T$ of the molecular ensemble) induced by the pulse or pulse train is then given by

$$\Delta E = k_B \Delta T = Tr(H_0 \boldsymbol{\rho}(t_f)) - Tr(H_0 \boldsymbol{\rho}^{(0)}) = \sum_{j,m} hcBj(j+1) \rho_{(j,m),(j,m)}(t_f) - k_B T_0, \qquad (2.2)$$

where $\boldsymbol{\rho}(t)$ is evolved by eq. (2.1) until time $t = t_f$ when the optical field from the pulse(s) is turned off. The pulses, individually or in a pulse train, are taken to be Gaussian in time.

The calculated rotational temperature change for a single pulse in N_2 is shown in Fig. 2 as a black solid line. The curve has been vertically shifted to match the experimentally measured hole depth in nitrogen. It matches well at low laser intensity *I* where rotational absorption is expected to be proportional to I^2, but saturates at higher intensity as higher *j*-states become more separated in energy.

The low intensity dependence can also be modeled classically as follows. For a classical rigid rotor, the torque on a molecule due to an optical field polarized at an angle θ with respect to the molecular axis is $\frac{1}{2} \Delta\alpha \left|\mathbf{E}\right|^2 \sin 2\theta$, where $\Delta\alpha = \alpha_{\parallel} - \alpha_{\perp}$ is

the molecular polarizability anisotropy along its long and short axes. This can be used to show (in appendix A) that the ensemble-averaged work done on a molecule in the limit of a single short pulse with fluence F is

$$\Delta E_{classical} = \frac{16F^2\pi^2\left(\Delta\alpha\right)^2}{15c^2 I_M} \quad . \tag{2.3}$$

This expression is plotted in Fig. 2.2 as a dashed line. The result agrees with the density matrix calculation at low intensities for a single pulse excitation of N_2 and O_2. We emphasize that the density matrix calculation predicts only the rotational absorption—at high intensities, the absorption is dominated by ionization and plasma heating as seen in the increasing deviation of the experimental points and simulation curves.

In the next experiment we investigated the effect of a 4-pulse train on the laser absorption and heating in nitrogen. With multiple pulses timed to match the rotational revival period, it is possible to strongly enhance the contribution of higher rotational states to the wavepacket ensemble [41]. Here we show directly that this translates into dramatically increased gas heating. The durations of pulses 1-4 were 110 fs, 110 fs, 120 fs and 110 fs, measured by a single shot autocorrelator, corresponding to vacuum peak intensities 61 TW/cm^2, 41 TW/cm^2, 41 TW/cm^2, 51 TW/cm^2. Note that if these pulses were coincident in time, the resulting single pulse would exceed the nitrogen ionization threshold. The pulse stacker time delays t_1 and t_2 were scanned by computer-controlled delay stages, so that the pulses arrived at $t = 0$, t_1, t_2, and t_1+t_2, as depicted in Fig. 2.1(b). We initially tuned the time separation between successive pulses to be T, the period of the first rotational revival. In nitrogen, $T = (2cB)^{-1} \approx 8.36$

ps, the time when the alignment revival crosses zero. Then, a fine 2D scan in (t_1, t_2) of $|\Delta N_{peak}| / N_{atm}$ was performed with 40 fs delay steps.

Figure 2.3(a) shows the results of the pulse delay scan. Each point in the graph depicts the relative depth of the gas density hole at its center. The deepest hole, near $t_1 = T$ and $t_2 = 2T$, corresponds to the situation where each pulse in the train excites the molecules at the full revival from the previous pulse. Other features in the plot can be understood as resonances involving fewer pulses. The vertical bar ($t_1 = T$, $t_2 = 2T + \Delta t$) is where the first two pulses and second two pulses are resonant, but the delay between the second and third pulses is not. The horizontal bar ($t_1 = T + \Delta t$, $t_2 = 2T$) is where the first and third pulses are resonant (at the second full revival of the first pulse), and the same with the second and fourth pulses. The diagonals correspond to resonances between two pulses in the train. The southwest to northeast diagonal ($t_1 = T + \Delta t$, $t_2 = 2T + \Delta t$) is where the second and third pulses are resonant. The southeast to northwest diagonal ($t_1 = T + \Delta t$, $t_2 = 2T - \Delta t$) is where the first and fourth pulses are

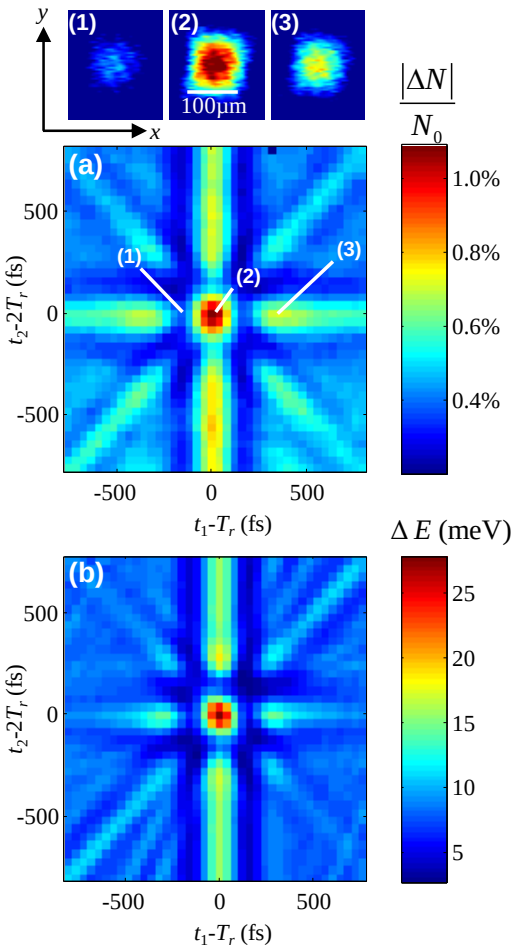

Figure 2.3. Rotational absorption as a function of time delays t_1 and t_2 in the pulse stacker. The images at the top show extracted density hole images for three delays, showing the varying depth of the hole. **(a)** Interferometric measurement of peak relative depth of gas density hole. The deepest gas density depression corresponds to the peak energy absorption predicted by the simulation. **(b)** Simulation of absorbed energy Δ*E*, found by numerically solving eqs. (2.1) and (2.2) and averaging along the pump beam's confocal parameter.

resonant (at the second half revival). The maximum depth of the gas density hole induced by the 4-pulse train is ~6 times greater than the minimum in Fig. 2.3(a), which is similar to that induced by a single pulse.

Figure 2.3(b) shows a simulation, using eqs. (2.1) and (2.2), of the absorbed energy in N_2 as a function of the (t_1, t_2) scan of a 4-pulse train using the experimental pulse parameters as inputs. The simulations predict ionization-free heating of as much

as ~32 meV/molecule (ΔT~150K) at the pump beam waist, which is only matched by a ~50 eV filament plasma (with electron density ~10^{16} cm^{-3} [59]). The plot shows an axial average peak heating of 28 meV/molecule along the pump confocal parameter. Comparison to Fig. 2.3(a) shows very good agreement between experiment and theory, with the resonance bars in the simulation decaying somewhat faster from the heating peak than in the experiment, an effect we are investigating. A similar experiment and simulation were performed for O_2 gas, likewise with good agreement.

So far we showed that it is possible to coherently excite a rotational wavepacket ensemble with a sequence of pulses separated by a full revival period, leading to strong heating of a gas of diatomic molecules. However, it is also possible to first excite the ensemble and then de-excite it well within the decoherence time over which it would normally thermalize and fully heat the gas. To show this, we used the first two pulses out of the pulse stacker, as specified earlier. The first pulse was used to excite the ensemble. We scanned the arrival time of the second pulse, t_1, near $T/2$ ~ 4.16 ps, the half-revival period of nitrogen. Figure 2.4 shows the measured depth of the density hole reduced by ~65% at the half-revival delay, while the simulation, axially averaged over the laser confocal parameter, shows an absorption reduction of ~ 90%. In essence, energy from the first pulse invested in the wavepacket ensemble is coherently restored to the second pulse. Viewed alternatively, the $T/2$-delayed second pulse acts as an out-of-phase kick to suppress the molecular alignment induced by the first pulse, in contrast to the T-delayed pulses which act as in-phase kicks to enhance alignment.

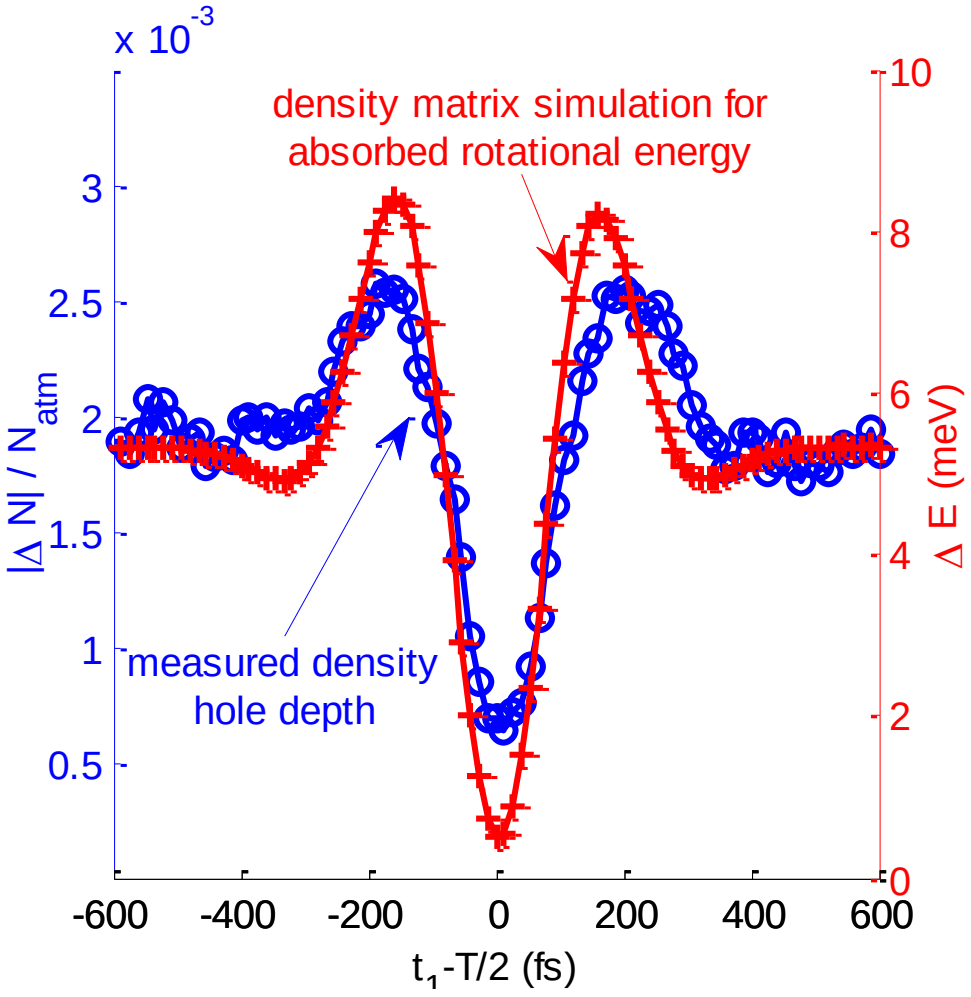

Figure 2.4. Reduction of rotational heating using two pulses. Blue circles: Measured change in gas density as a function of the time delay t_1 between two pulses spaced near the half revival $T/2 \sim 4.16$ ps in N_2. The hole depth is reduced by ~65%. Red crosses: Simulation of rotational energy change per molecule from solving eqs. (2.1) and (2.2) for varying t_1, showing absorption reduction of ~90%.

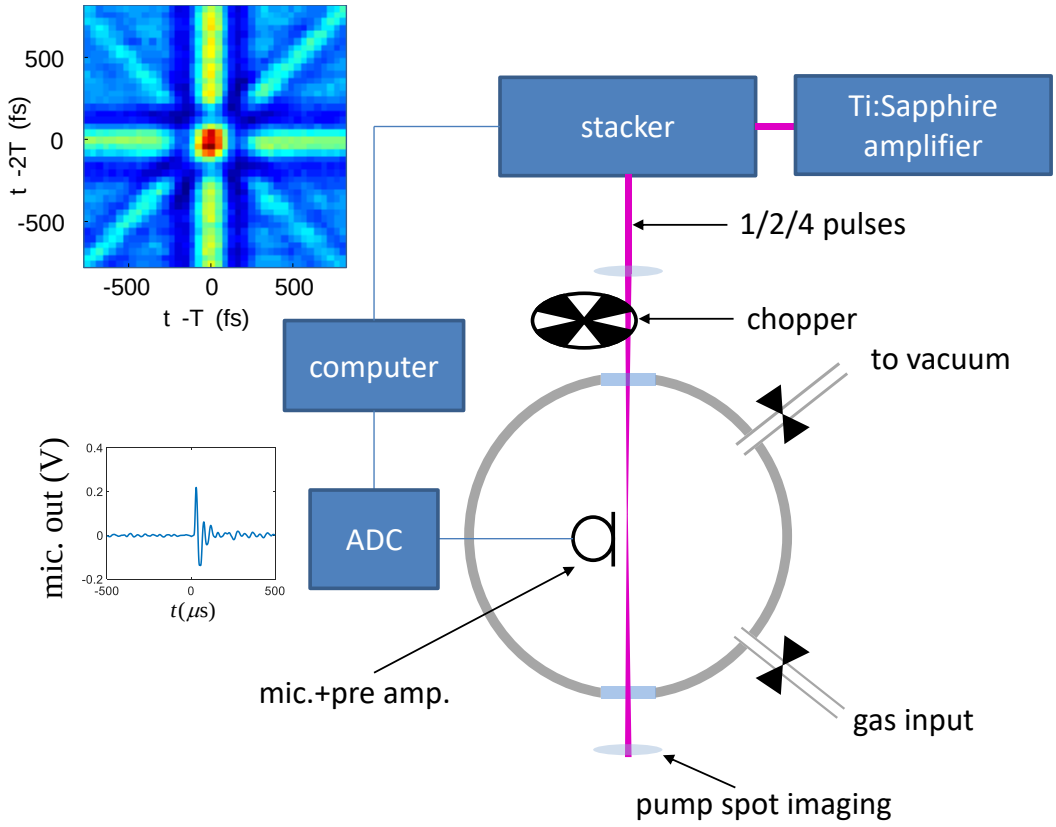

Figure 2.5. Experimental setup for the photoacoustic measurements of gas heating. The inset on the lower left shows a sample trace from an amplified electret microphone, digitized by an analog-to-digital convertor (ADC). The inset on the upper left shows the amplitude of the sound wave as a function of two delays.

2.4 Photoacoustic measurement of resonant rotational heating

In our previous investigation of resonant rotational heating in air, we used interferometry with a CW helium-neon laser to measure the density depression produced by the gas heating. Here we employ an electret microphone[1] to measure the emitted acoustic wave amplitude [38] from the column of heated gas, which is shown to be a good proxy [10] for the amount of energy absorbed by the gas. Acoustics have been used to study energy deposition in extended filamentary propagation [14,33], THz wave detection [60], and to study rotational heating in an optical

[1] Sparkfun BOB-12758

centrifuge [46,61], where chirped optical pulses are used to excite extremely high angular momentum states. The microphone/acoustic method is relatively simple: while interferometry requires complex processing of interferograms and care to minimize probe refractive distortion by the heated gas column, the acoustic technique merely requires placement of a microphone near the laser focus to sample the emitted acoustic waves, with the signal collected by a slow oscilloscope or A/D converter. The experiment is depicted in Fig. 2.5 which includes a sample trace from the microphone. In a 4-pulse experiment we observe a resonant peak in the sound emitted due to rapid expansion of gas (red region in center). The microphone measurement also reproduces the horizontal, vertical and diagonal features of the interferometric density hole measurement. We performed similar timing scans as in the interferometric measurements for various peak laser intensities, with the results shown in Fig. 2.6(a-c). The duration of each pulse in the 4-pulse train is 95 fs FWHM, where each pulse in the sequence has energy (a) 25μJ, (b) 62μJ and (c) 84μJ with corresponding peak intensities per pulse of 15TW/cm^2, 40TW/cm^2, and 50TW/cm^2. The molecular absorbed energy from the pulse sequence is simulated using density matrix code [29] and shown in Fig. 2.6(d-f). The horizontal dark bands in Fig. 2.6(c) are due to periodic laser energy fluctuation during the scan.

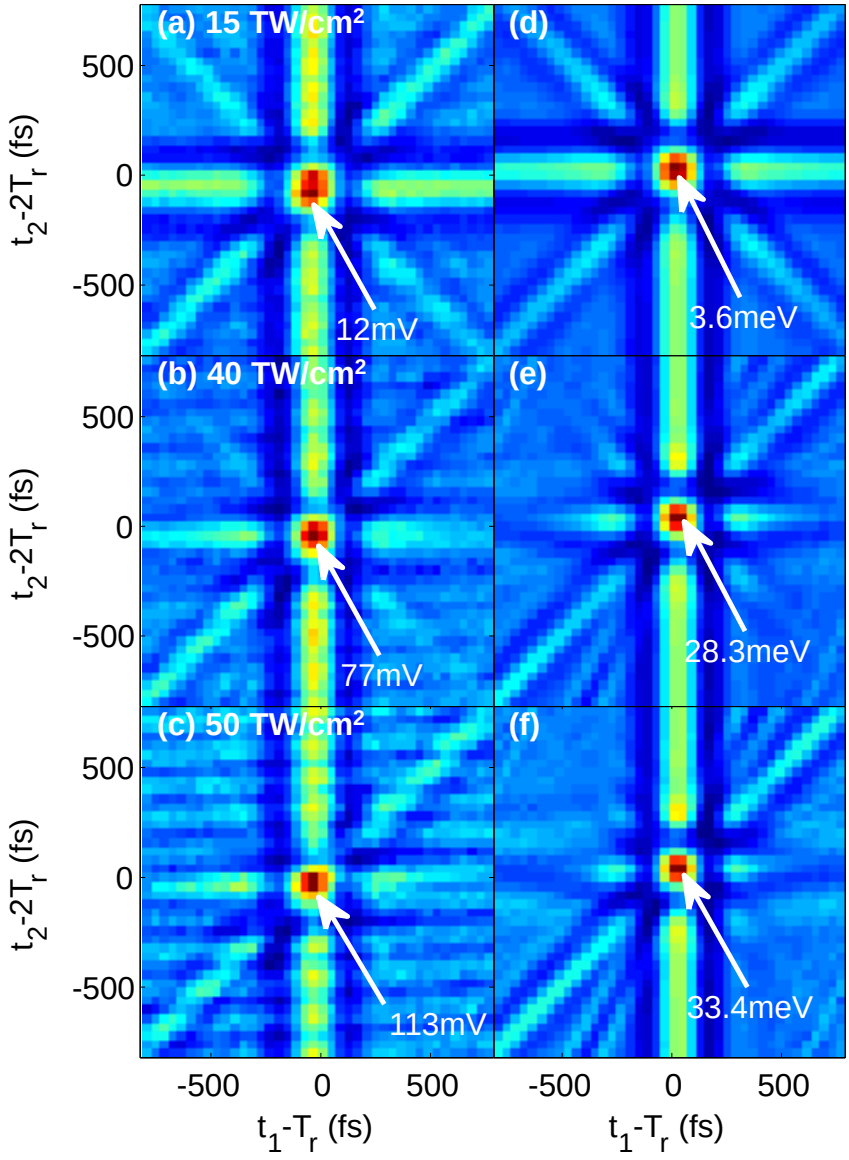

Figure 2.6. Experimental **(a-c)** photoacoustic measurement of the intensity dependence of the microphone data and comparison to density matrix code. In panels **(d-f)** the heating due to the pulses are calculated using density matrix simulation. The width of the pulses is 95fs with peak intensities **(a)**15 TW/cm^2, **(b)**40 TW/cm^2, and **(c)**50 TW/cm^2.

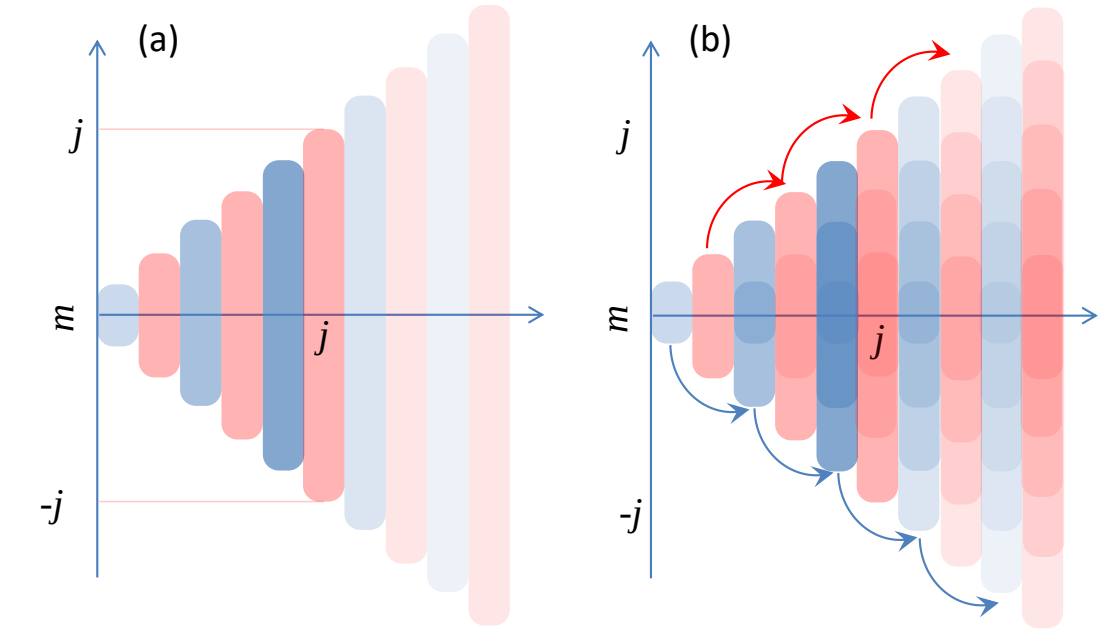

Figure 2.7. (a) At thermal equilibrium for a given *j*-state all of *m*-states are equally likely to be occupied, resulting in net zero birefringence. **(b)** Transitions of the form $j \to j+2$ and $m \to m$ make lower *m*-states to be more likely to be occupied resulting in a net alignment along *z*-axis.

2.5 SSSI measurement of permanent alignment

In §2.2-§2.4 we experimentally showed that a train of ultrashort laser pulses—if properly timed— can resonate with rotational states of a diatomic molecule such as N_2 and result in heating the gas. To show gas heating, we measured long timescale events such as sound emission and reduction in density, long after the last pulse in the laser pulse train. These long timescale events are the consequence of the rotational energy deposited in the molecules. On shorter timescales (<100ps [29]), before collisions redistribute the rotational energy, the gas becomes birefringent due to permanent alignment [62] of the molecule along the laser polarization. In this section, we use SSSI to measure this alignment.

At thermal equilibrium the distribution of an ensemble of diatomic molecules is governed by the thermal distribution $\rho^{(0)}_{jmj'm'} = D_j \delta_{jj'} \delta_{mm'} \exp\left(-E_j / k_B T_0\right) / Z$; for a given *j*-state, the molecule is in any of the $m = -j, \cdots, j$ states with equal probability.

Recall, for sufficiently large *j*, a state with large $m<j$ has rotational angular momentum aligned mainly along the laser polarization axis (*z*-axis). Thus the molecular axis is almost orthogonal or anti-aligned to the laser polarization. Conversely, states with low *m* are mostly aligned along the laser polarization. Therefore, in thermal equilibrium, the uniform distribution of *m* states means that there is no net alignment. In §1.2 we saw that a laser pulse can create a rotational wave packet, i.e., a coherent superposition of $|j,m\rangle$ states. The phases of these states oscillate with frequency $E_j/\hbar = \omega_j = 2\pi cBj(j+1)$, and the alignment $<\cos^2\theta>_t$, the time-dependent ensemble average of $\cos^2\theta$, where θ is the angle between the laser electric field and the molecular axis, shows periodic 'revival' structure, with full revival period of $T_r = 2\pi/\omega_1 = (2cB)^{-1}$. Furthermore, we saw that a train of linearly co-polarized laser pulses resonant with the revivals[1] can effectively pump the rotational states causing the population to shift from $|j,m\rangle$ to $|j+2n,m\rangle$, where *n* is an integer. As $\Delta m=0$ for these Raman transitions, for each *j* the distribution of *m* states is no longer uniform, because states of lower *m* are more likely occupied. This leads to a residual *permanent alignment* [62] along the laser polarization, causing the gas to become birefringent, and is schematically show in Fig.2.7. In this section, we use SSSI to directly detect this permanent alignment by observing the birefringence in N_2 resonantly pumped by 8 pulses, each of which is 80 fs, 45 TW/cm^2. Recall from chapter 1 that in regular SSSI, the reference and the probe pulses are delayed by ~2 ps, with the reference arriving first. This maximum delay is set by the resolution of

[1]According to density matrix simulations, the optimal timing for the resonant pumping of *j*-states is such that each laser pulse in the train arrives at the zero crossing of revival due to the previous pulse.

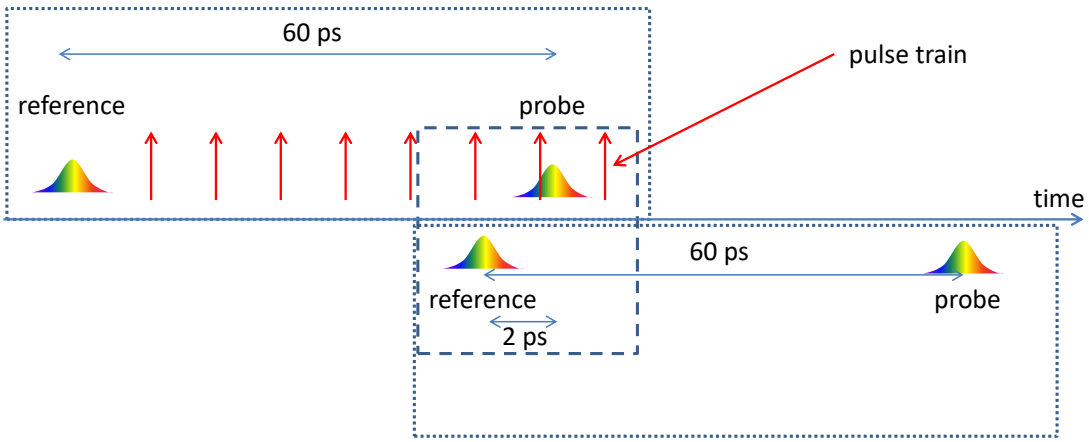

Figure 2.8. In order to measure permanent alignment, we need to have the reference arrive before the first pulse in the pump laser pulse train, and the probe to arrive up to ~60 ps later. This causes the spectral fringes to be too fine for the imaging spectrometer; in order to have both long time delay between reference and probe and also be able to resolve the fringes, we added another Michelson interferometer before the beam enters the spectrometer. We set the delay on this interferometer to 2 ps. The 120 ps apart reference and probe add to the background without making any fringes.

the spectrometer: A longer delay results in extremely closely-spaced fringes in the spectral domain which cannot be resolved by the CCD camera. However for N_2, where $T_r = 8.36\text{ps}$, a 2 ps reference-probe delay is too short for observing permanent alignment, because both the reference and the probe will pick up the permanent alignment phase shift, preventing the measurement of any difference. In order to measure a phase shift caused by permanent alignment, we use a $\sim 7T_r \sim 60\text{ps}$ delay between reference and probe. This allows the reference pulse to arrive before the 8 pump pulse sequence and the probe pulse to arrive after.

We achieved this delay, while still preserving measurable spectral fringe spacing, by adding another Michelson interferometer after the interaction region but before the spectrometer, as shown in Fig. 2.8, so that two replicas of the reference and probe are produced. This allows us to place a copy of the probe at a short delay (<<60 ps) from a copy of the reference so that they form easily resolvable fringes in the spectral

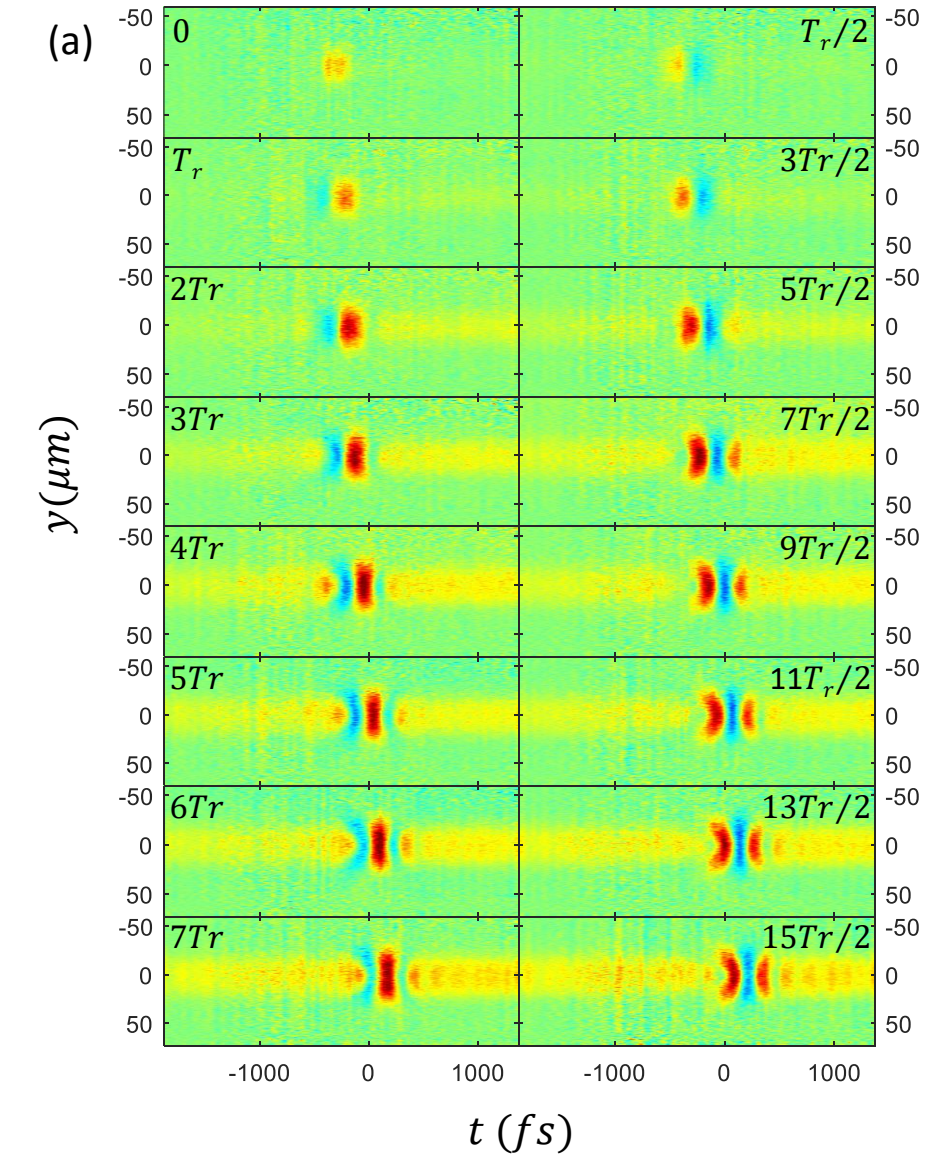

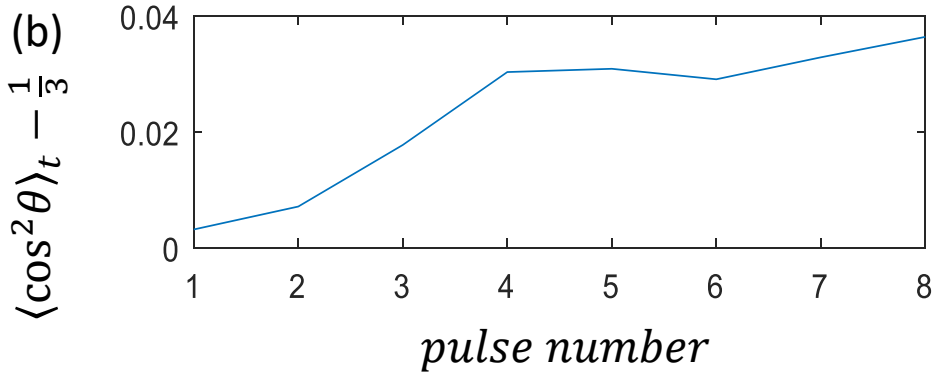

Figure 2.9. (a) Transient and permanent alignment due to pulse train around t = 0 and full revivals (left column) and half revivals (right column) in N_2 for 8 pulses of 45 TW/cm$^{2.}$ **(b)** Alignment measured after each pulse in the 8-pulse train. We see saturation of permanent alignment at $5T_r$ (in vicinity of the 5th pulse)

domain. Meanwhile, the other reference/probe pair, which are widely separated in time, make unresolvable fringes that add to a smooth background. Figure 2.9(a) shows the extracted SSSI phase. The left column is the time window around the main pulse and the full revivals whereas the right column shows a time window near the half revivals. We see that after 2 pulses the permanent alignment is detected as a faint yellow horizontal strip around $y = 0$. The later pulses cause this alignment to become stronger until it saturates by the 4^{th} -5^{th} pulse as shown in Fig. 2.9 (b).

2.6 Saturation caused by centrifugal distortion

Rotational revivals are the cornerstone for resonant pumping of molecular rotations. For a rigid molecular rotor undergoing no collisions, the dynamics remain coherent: the revival period is fixed, and the temporal structure at each revival is identical. In air, dephasing due to collisions causes this coherence to disappear with ~100ps timescale [29]. However, even without consideration of collisions, dephasing occurs because the rigid rotor approximation breaks down for high *j* states: for high *j*-states the molecular bond stretches due to the centrifugal force, the rigid rotor Hamiltonian must be corrected to account for this, leading to corrected eigenenergies of the $|j,m\rangle$ states to be modified as $E_j/\hbar = \left[hcBj(j+1) - hcDj^2(j+1)^2 \right]/\hbar$, with *D* being the centrifugal distortion constant ($D/B \approx 10^{-6}$ for N_2 and O_2). Therefore, the rotational wave packet is not actually periodic with period of T_r; the $|\psi\rangle = \sum_{jm} a_{jm} |j,m\rangle$ wavepackets underlying the revivals diphase causing the revivals to decrease in amplitude and broaden in time (disperse) We call this effect "centripetal dispersion". A pulse train spaced at T_r will produce nearly optimal heating initially, but as centrifugal distortion becomes more pronounced, there is no

single moment in time that a laser pulse can interact with all of the *j*-states with the same phase. Eventually the heating caused by later pulses becomes less efficient as the laser pulse excites some states while de-exciting others. This effect has been termed the "Anderson wall" [63] because of an analogy between periodic kicking of quantized molecular rotational states and a disordered lattice [64]. It is important to realize that centripetal dispersion is just one fundamental limiting factor for practical rotational heating with long train of pulses; the other fundamental limitation is dephasing due to collisions. The dephasing by due to centrifugal distortion can be somewhat mitigated simply by adjusting pulse train timing interval by a few tens of femtoseconds, so that each pulse remains resonant with the shifting revival peaks from the contributions of the higher *j*-states.. Although centrifugal dispersion results in the eventual disintegration of the rotational revival as a well-defined structure, our simulations show that for pulse trains as long as 10 pulses, it is possible to resonantly heat linear molecules such as N_2 by intelligently delaying the pulses so they still resonate with some $|j,m\rangle$ states. In Fig 2.10(a) shows the deposited energy simulated in N_2 for a train of 14 impulses with each impulse has a fluence of 0.5J/cm^2 and the pulse train has a period of $T = T_r + \varepsilon$, with $\varepsilon \geq 0$ varied between simulations. The solid line curves in Fig 2.10(b) shows the same simulation but the fluence of each impulse is increased to 3J/cm^2. In the first case, the fluence of each pulse in the pulse train is such that after 13 pulses, an additional pulse can still resonate with significant population of *j*-states and continue depositing energy. The energy deposition is further improved if the period of the pulses is increased to $T_r + 15\text{fs}$. In the second case, for $T = T_r$ the pulse train excites large *j*-states so that it only remains resonant

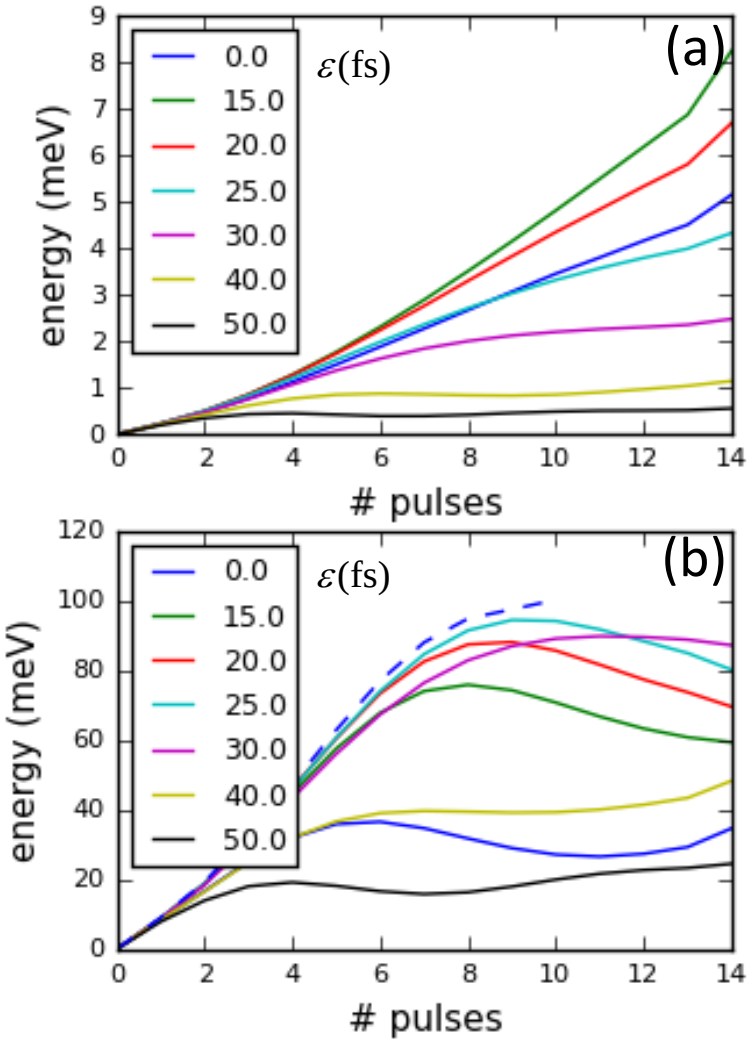

Figure 2.10. Solid curves show simulation of energy deposition in N_2 for a periodic trains of impulses with fluence of **(a)** 0.5J/cm^2 and **(b)** 3J/cm^2 with period of $T = T_r + \varepsilon$. In the first case the pulse train with $T = T_r$ remains resonant even after 14 pulses. In the second case, this pulse train can only remain resonant for 6 pulses.

with a significant population of the states only for 6 pulses. If the pulse train period is increased to $T = T_r + 25\text{fs}$ it can remain resonant for 9 pulses. The dashed line in this figure shows the heating due to an aperiodic pulse train, with the time separation between the last pulse and the next pulse is chosen so that energy deposition is maximized. Even in this case we observe that only 10 pulses remain resonant with net heating almost equal to the periodic pulse train.

In summary, we have measured the dramatic gas hydrodynamic response to coherent excitation and de-excitation of a molecular rotational wave packet ensemble, at peak laser intensities well below the ionization threshold. The laser absorption and gas heating is significantly enhanced by using a 4-pulse train with pulses separated by the molecular rotational revival time. Heating is strongly suppressed by coherently de-exciting the molecular ensemble using pulses spaced by a half-revival. The femtosecond sensitivity to pulse train timing of gas heating and heating suppression is well-predicted by density matrix simulations of the evolution of the wave packet ensemble. These results make possible the fine quantum control of gas density profiles using non-ionizing laser pulses. Such profile modification, at both near and remote locations, has a range of exciting applications including the refractive index control of high power optical pulse propagation in air [12,36,37]. Next we directly measured the permanent alignment superimposed on the dynamic rotational response due to a train of 8 pulses using a modified SSSI setup. The permanent alignment is viewed as a proxy for showing that the pulse train is exciting *j*-states with $\Delta m = 0$ causing the gas to become birefringent. We experimentally observed saturation of the permanent alignment in time domain. Through simulations, we attributed the saturation in both gas heating and permanent alignment to centripetal dispersion in the rotational wave packet.

Chapter 3: Measurement of refractive index of air constituents and wide bandgap solids in mid-IR region

3.1 Introduction

Accurate values for nonlinear coefficients are essential for high-fidelity simulations of intense laser propagation [65–67]—such simulations are indispensable not only for designing experiments and informing applications, but they also motivate the design and parameters of the lasers themselves. It is known that in the near-infrared (pump wavelength $\lambda_e = 0.8\mu\text{m}$), air propagation simulations depend very sensitively on the values used for the coefficients (n_2) describing the instantaneous electronic nonlinear response of air constituents [68]. The best agreement of the simulations with axially resolved measurements occurs for n_2 coefficients measured in [22] using SSSI. In this chapter, we present measurements of n_2 for the air constituents N_2, O_2, and Ar at pump wavelengths ranging from 400 nm to 2400 nm. The near- through mid-IR wavelengths chosen ($\lambda_e = 1250, 1650, 2200$ and 2400nm) are within the transparency windows of air [69]. We find that the nonlinear response is quite dispersionless over the range of wavelengths investigated, except near $\lambda_e = 400nm$, consistent with a simple model for the third-order nonlinear susceptibility developed by Bishop [70].

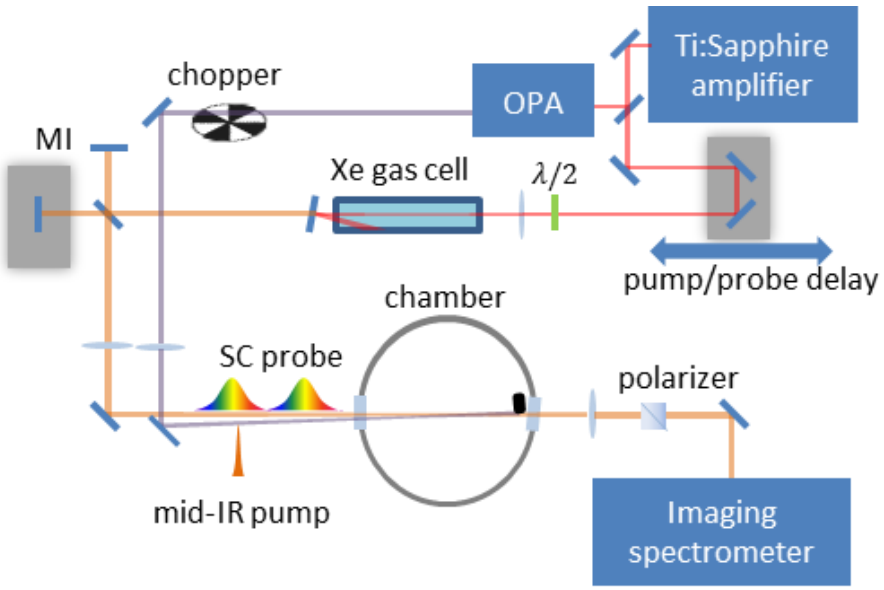

Figure 3.1. Diagram of the experiment. A Ti:Sapphire regenerative amplifier pumps an infrared optical parametric amplifier (OPA) to produce a tunable pump pulse and generates visible supercontinuum (SC) in a Xe gas cell. A Michelson interferometer (MI) creates probe and reference SC pulses. Pump and probe/reference beams are crossed in a chamber filled with N_2, O_2, or Ar. The spectral phase and amplitude of the probe is measured and used to find the time-domain phase shift induced by the pump pulse.

3.2 Experiment setup

The experimental setup is shown in Fig 3.1. We use SSSI [28], as explained in Chapter 1, for our measurements. Pulses from a 1 kHz Ti:Sapphire regenerative amplifier centered at 800 nm are split, with 2.8 mJ pumping an optical parametric amplifier (OPA), which is tunable from 1100 to 2600 nm. A chopper after the OPA reduces the pump pulse repetition rate to 500 Hz so that for each SSSI measurement of the pump interacting with the gas, there is a following measurement without the pump; the subtraction of these results enables dynamic background elimination even when the laser drifts slightly. It also compensates for any spectral phase differences between the reference and the unperturbed probe.

The remaining portion of the 800 nm pulse is attenuated and weakly focused in a 2 atm xenon gas cell, where filamentation generates a 500–700 nm supercontinuum (SC) transmitted through the pump-rejecting dichroic splitter. An interferometer splits the SC into two collinear pulses (reference and probe) separated by 2 ps. The dispersive glass in the SC beam path introduces ~equal positive chirp on the reference and probe making each of the ~1.5 ps long. The OPA output and the SC reference/probe are focused in a backfilled chamber, crossing at 2°. The crossing angle is small enough to consider all pulses as collinear in the analysis. The reference pulse precedes the pump, which is temporally overlapped by the probe, encoded with the pump-induced time-varying nonlinear phase shift.

The focal plane of the reference/probe is imaged onto the entrance slit of an imaging spectrometer, inside of which the reference and probe pulses interfere in the spectral domain. Two-dimensional spectral interferograms (1D space and wavelength) are recorded by a CCD camera at the spectrometer's imaging plane. The 2° angular separation between the pump and reference/probe ensures that the pump is stopped at a beam dump before the entrance slit of the spectrometer. Fourier analysis of the spectral interferogram, using the measured spectral phase of the probe [28,29], enables extraction of the time- and 1D-space-resolved phase shift $\Delta\varphi(x,t)$ induced by the pump pulse with the time resolution limited to <10 fs by the SC bandwidth. Here, x is a transverse coordinate in the pump focal plane. The reference/probe polarization is oriented either parallel or perpendicular to the pump polarization by a half-wave plate before the xenon SC cell. A Glan-Taylor polarizer (10^5:1 extinction ratio) is placed in the reference/probe path to further refine the linear polarization.

Pump–probe walk-off is minimal in these experiments: for the probe central wavelength $\lambda_p = 600\text{nm}$ and pump wavelength range $\lambda_e = 400 - 2400\text{nm}$, the walk-off for our pump–probe interaction length of ~2 mm is <0.5 fs, well below the timescale of the most rapid index transients in the experiment, which are of the order of the pulse width of 40 fs (at $\lambda_e = 800\text{nm}$).

3.3 Separation of electronic response from rotational response

In N_2 and O_2, the nonlinear response is dominated by the near-instantaneous electronic (Kerr) and the delayed rotational responses [29]. If $\Delta\varphi_{\parallel}(x,t) = \Delta\varphi_{elec}(x,t) + \Delta\varphi_{rot}(x,t)$ is the SSSI-extracted phase shift for the probe, polarized parallel to the pump, then nonlinear susceptibility tensor symmetry [71] implies (derived in Appendix B) that $\Delta\varphi_{\perp}(x,t) = \tfrac{1}{3}\Delta\varphi_{elec}(x,t) - \tfrac{1}{2}\Delta\varphi_{rot}(x,t)$ for the perpendicular polarized probe. These equations then yield

$$\begin{aligned} \Delta\varphi_{elec}(x,t) &= 3/5\left(\Delta\varphi_{\parallel}(x,t) + 2\Delta\varphi_{\perp}(x,t)\right) \\ \Delta\varphi_{rot}(x,t) &= 2/5\left(\Delta\varphi_{\parallel}(x,t) - 3\Delta\varphi_{\perp}(x,t)\right) \end{aligned} \tag{3.1}$$

for the separate electronic and rotational nonlinear responses.

Figures 3.2(a) and 3.2(b) show $\Delta\varphi_{\parallel}(x,t)$ and $\Delta\varphi_{\perp}(x,t)$ phase shift measurements in N_2 at $\lambda_e = 1250\text{nm}$. Central lineouts $\Delta\varphi_{\parallel}(x=0,t)$ and $\Delta\varphi_{\perp}(x=0,t)$ are shown in

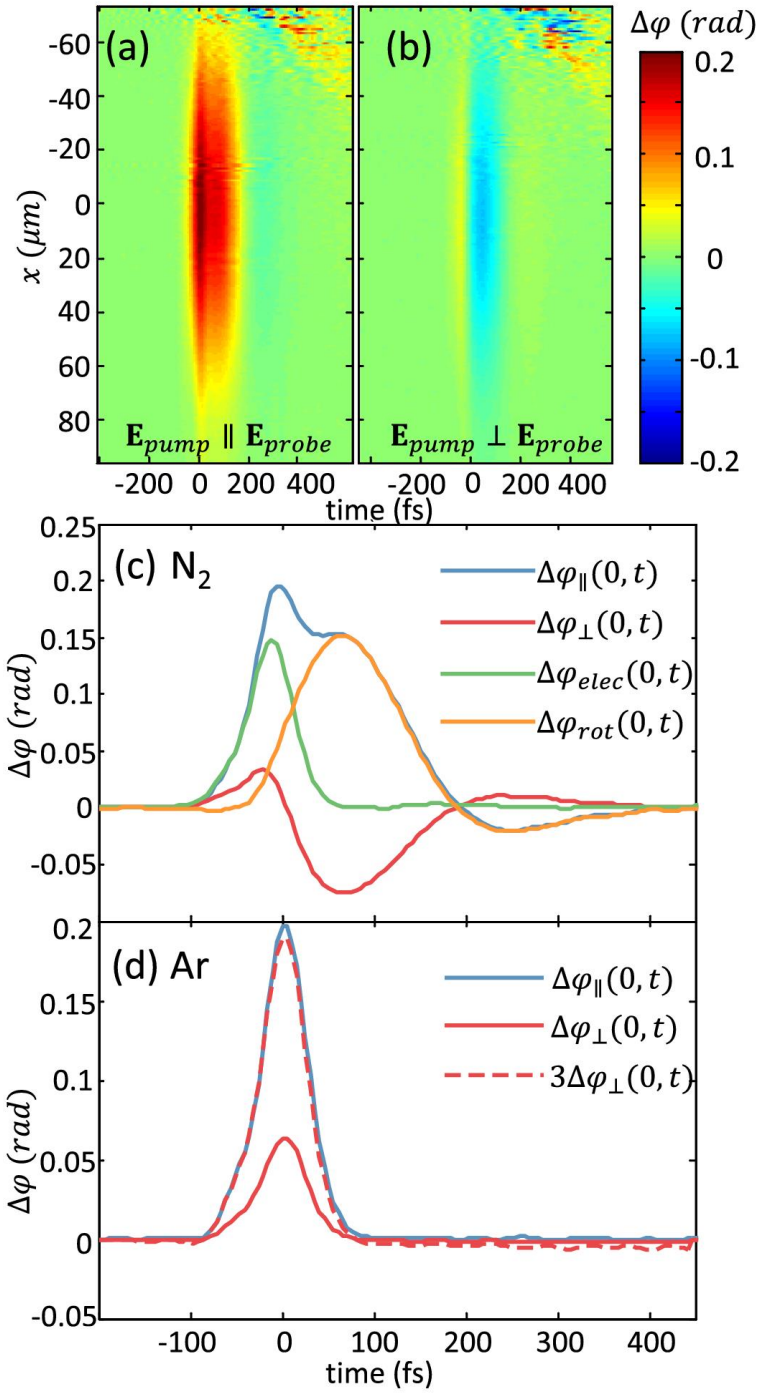

Figure 3.2. Experimental results in N_2 and Ar at $\lambda_e = 1250\text{nm}$ central pump wavelength: **(a)** nonlinear phase shift $\Delta\varphi_{\parallel}(x,t)$ of the probe for $\mathbf{E}_p \parallel \mathbf{E}_e$ and **(b)** nonlinear phase shift $\Delta\varphi_{\perp}(x,t)$ of the probe for $\mathbf{E}_p \perp \mathbf{E}_e$ in N_2. **(c)** Temporal lineouts $\Delta\varphi_{\parallel}(x=0,t)$ and $\Delta\varphi_{\perp}(x=0,t)$ in N_2 and their decomposition into electronic and rotational responses, as described in the text. **(d)** Temporal lineouts of the parallel and perpendicular polarized phase shift in Ar and the perpendicular phase shift scaled by a factor of 3.

Fig. 3.2(c), along with the electronic and rotational responses $\Delta\varphi_{elec}(x=0,t)$ and $\Delta\varphi_{rot}(x=0,t)$ extracted using eq. (3.1). Figure 3.2(d) shows the same plot for Ar, which lacks a rotational response, verifying that $\Delta\varphi_{elec,\parallel}(x=0,t)=3\Delta\varphi_{elec,\perp}(x=0,t)$, as expected for an instantaneous isotropic nonlinearity. This verifies the sensitive ability of our technique to separate the electronic and rotational responses.

In prior measurements of absolute determination of the Kerr and rotational nonlinearities at $\lambda_e = 800\text{nm}$, we used auxiliary interferometric measurements of the optical thickness of our thin gas target and measurements of the pump intensity profile [22]. Here, we use an alternative method, employed in other recent pump–probe nonlinearity measurements [72,73], in which we reference all of our nonlinear phase shift measurements to the rotational responses in nitrogen and oxygen without explicit need for either gas density, pump-probe interaction length or pump intensity profiles. We use the fact that, to the second order in the pump field, the response, as measured by the nonlinear index shift experienced by the probe, is the sum of the electronic and rotational responses [22], $\Delta n_p(x,t) = 2n_2 I(x,t) + \int_{-\infty}^{t} R(t-t')I(x,t')dt'$, where I is the pump intensity; n_2 is the electronic Kerr coefficient, which depends on the probe and pump wavelengths λ_p and λ_e; and R is the impulse response function for quantized rotations of a rigid rotor. The terms in this expression are related to our measured phase shifts by

$$\begin{aligned}\Delta\varphi_{elec}(x,t) &= 2n_2 I_0 f(x,t) k_p L \\ \Delta\varphi_{rot}(x,t) &= \frac{2\pi N k_p L}{n_0}\Delta\alpha(\lambda_p)\left(\left\langle\cos^2\theta\right\rangle_t - \frac{1}{3}\right) \\ &= \frac{2\pi N k_p L}{n_0}\Delta\alpha(\lambda_p)\Delta\alpha(\lambda_e)\frac{I_0}{c\hbar}\int_{-\infty}^{t} g(t-t')f(x,t')\,\mathrm{d}t',\end{aligned} \tag{3.2}$$

where I_0 is the pump peak intensity, and $f(x,t)$ is its normalized spatiotemporal profile; k_p is the probe wavenumber; $L\sim 2$ mm (<pump confocal parameter of ~ 5 cm) is the pump–probe interaction length, N is the molecule number density, n_0 is the background gas refractive index, $\Delta\alpha(\lambda_e)$ [$\Delta\alpha(\lambda_p)$] is the polarizability anisotropy at the pump [probe] wavelength; $\left\langle\cos^2\theta\right\rangle_t - \frac{1}{3}$ is the ensemble-averaged transient alignment induced by the pump pulse [29]; and the rescaled impulse response function is [29] $g(t) = \frac{-16\pi}{15}\sum_j j(j+1)\Big/(2j-1)\left(\rho_j^{(0)} - \rho_{j-2}^{(0)}\right)\sin\omega_{j,j-2}t$ where $\rho_j^{(0)}$ is the thermal population of state j, $\omega_{j,j-2} = 4\pi cB(2j-1)$, and B is the rotational constant.

Essential to our method for absolute measurements is accurate recovery of the pump pulse envelope. Figures 3.3(a) and 3.3(b) show the nonlinear phase shift at $\lambda_e - 2200$nm for argon and nitrogen. The somewhat complex pulse pump envelope $f(x,t)$ measured in Fig. 3.3(a) results from the propagation of the OPA idler through a dichroic mirror. Figure 3.3(b) shows that such accurate recovery of the intensity envelope enables a clean separation of the electronic and rotational responses, even when the envelope is complex.

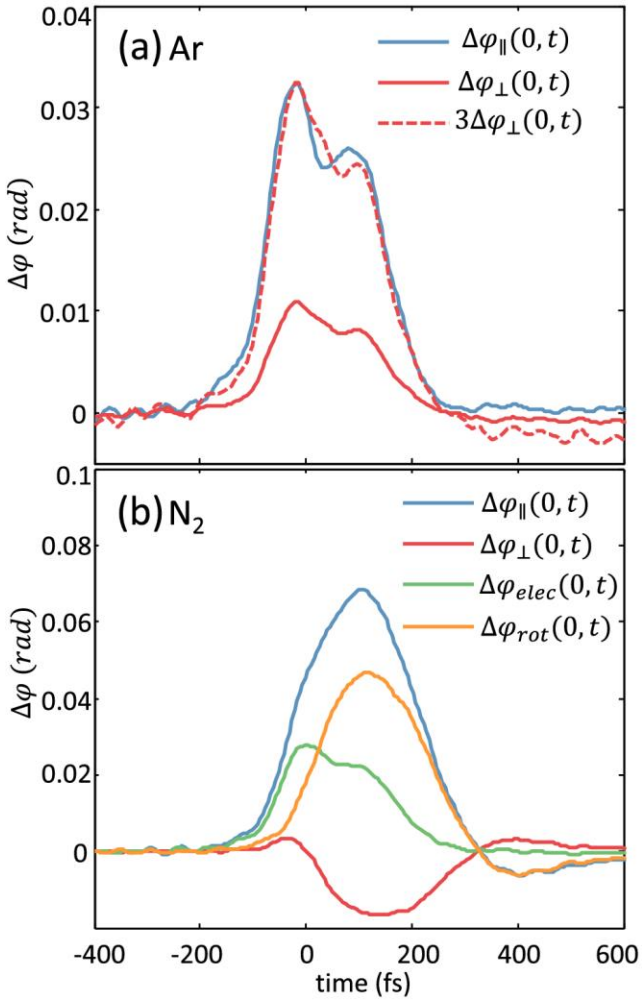

Figure 3.3.Experimental results in **(a)** Ar and **(b)** N_2 at 2200 nm, a wavelength where the pump pulse shape is longer and more complex than at shorter wavelengths.

Examination of Eq. (3.2) now shows that measurement of $\Delta\varphi_{rot}(x,t)$ and computation of the convolution integral $\int_{-\infty}^{t} g(t-t')f(x,t')\,\mathrm{d}t'$ from the known and measured functions g and f gives $\mu_1 = \Delta\alpha(\lambda_p)\Delta\alpha(\lambda_e)NLI_0$. This then allows determination of $\mu_2 = n_2(\Delta\alpha(\lambda_p)\Delta\alpha(\lambda_e))^{-1}$ through the equation for $\Delta\varphi_{elec}(x,t)$. It is important to note that there is a large two-dimensional sample size of μ_2 measurements in each SSSI shot, since the phase shift measurement is both time and

1D-space resolved. In the extracted phases shown here (for example, Fig. 3.2) there are ~100 points in x and ~50–100 points in t, so in principle each shot embodies a maximum ~5000 measurements of μ_2.

Our results for n_2 are summarized in Table 3.1. The uncertainties quoted in the table originate from three sources. First is the residual square error in μ_1 from least-squares fits of $\Delta\varphi_{rot}(x,t)$ [eq. (3.2)] to the data points spanning t for fixed x. The x average of these results gives the tabulated n_2 values, and the standard deviation is one source of uncertainty. Another source of uncertainty is slight laser average power drift over the course of a run, and we include its estimated effect in the displayed error. Finally, we include the propagated uncertainty in the value of $\Delta\alpha$, as given in [22]. The noticeably higher error for the $\lambda_e = 2400\text{nm}$ measurements originates from the very small nonlinear phase shifts (maximum of ~30 mrad) measured for that low peak pump intensity.

From the expression above for μ_2, it is clear that determination of n_2 requires assessment of dispersion in $\Delta\alpha$. Such dispersion has been calculated to have the approximate frequency dependence $\Delta\alpha(\omega) \approx \Delta\alpha(0) + C\omega^2$ [74]. Light scattering measurements for N_2 [75] are well fit by $\Delta\alpha(0) = 6.6\times10^{-25}\text{cm}^3$ and $C = 3.8\times10^{-57}\text{cm}^3\text{s}^2$. This relation, with $\Delta\alpha(0)$ scaled so that $\Delta\alpha(\omega)$ matches our measured value of $\Delta\alpha$ at $\lambda_e = 800\text{nm}$ [22], was used to account for the dispersion of $\Delta\alpha$ in the analysis. The dispersion is quite weak: $\Delta\alpha(\omega_{800\text{nm}})/\Delta\alpha(0) \sim 1.03$ and $\Delta\alpha(\omega_{400\text{nm}})/\Delta\alpha(0) \sim 1.13$.

It is evident from Table 3.1 that neglecting $\Delta\alpha$ dispersion affects the results by at most ~10% near $\lambda_e = 400\text{nm}$ and <2% at longer wavelengths [compare N_2 columns (a) and (b)]. Next, we see that results for n_2 are dispersionless within the precision of our measurements, except near $\lambda_e = 400\text{nm}$ (except for O_2). This is in accord with calculations of the third-order hyperpolarizability at optical frequencies below electronic resonances [70,76]. It is important to be clear that while the Kerr coefficient we actually desire is $n_2(\omega_e) = \left(12\pi^2/cn_0^2\right) N\gamma^{(3)}(\omega_e;\omega_e,-\omega_e,\omega_e)$, where $\gamma^{(3)}$ is the third order hyperpolarizability, our pump–probe experiment actually measures $n_2(\omega_e,\omega_p) \propto \gamma^{(3)}(\omega_p;\omega_e,-\omega_e,\omega_p)$. However, the dispersion formula of [70,76] gives

$$\gamma^{(3)}(\omega_s;\omega_1,\omega_2,\omega_3) = \gamma_0\left(1 + a\omega_L^2 + b\omega_L^4 + \cdots\right), \tag{3.3}$$

where $\omega_s = \omega_1 + \omega_2 + \omega_3$, γ_0 is the static hyperpolarizability, $\omega_L^2 = \omega_s^2 + \omega_1^2 + \omega_2^2 + \omega_3^2$, and $a = 1.8\times10^{-33}, 3\times10^{-33}\text{s}^2$, $b = 1.5\times10^{-65}, 1.6\times10^{-65}\text{s}^4$ and $\gamma_0 = 7.7\times10^{-30}, 9.8\times10^{-30}\ \text{cm}^6/\text{Ws}$ for N_2 and Ar, respectively. For our pump–probe case, $\omega_s = \omega_p$ and $\omega_L^2 = 2\omega_e^2 + 2\omega_p^2$; thus eq. (3.3) gives, at worst (shortest λ_p and longest λ_e), $\delta = \left|n_2(\omega_e,\omega_p) - n_2(\omega_e)\right| / n_2(\omega_e) <\sim 0.06$ for pump and probe wavelengths longer than ~500 nm, which applies to most of Table 3.1 and is within our measurement error. For $\lambda_e = 400\text{nm}$ and $\lambda_p = 600\text{nm}$ (center wavelength of supercontinuum), $\delta <\sim 0.06$, also within our measurement error, confirming the dispersion of n_2 in N_2 and Ar near 400 nm.

In Table 3.1, we compare our results in Ar, N_2, and O_2 with the values of n_2 calculated with Eq. (3.3) using values of γ_0, a, and b (shown above for N_2 and Ar) found using the electric-field-induced second harmonic generation (ESHG) technique [77], in which $\omega_1 = \omega_2 = \omega$ and $\omega_3 = 0$. The agreement is very good. The ESHG results in argon and nitrogen have been shown to agree with theoretical calculations [78–80] to within ~10%. Both theory and ESHG experiments agree with our finding that the nonlinear refractive index is quite dispersionless in the infrared.

Table 3.1 Measured electronic Kerr coefficient $n^{s}_{2,\mathrm{elec}}$ at 1 atm (at probe wavelength of 600 nm and pump wavelength of 800 nm), polarizability anisotropy $\Delta\alpha$, and polarizability derivative $\partial\alpha/\partial Q$. A comparison is made with previous experimental and theoretical work. The rightmost column shows n_2 estimates at 1 atm based on our experimental results for a long pulse at 800 nm.

Pump Wavelength λ_e (nm)	N_2[b]			N_2[c]		O_2[c]			Ar[d]	
	$n_2(10^{-20}\ \mathrm{cm^2/W})$			$n_2(10^{-20}\ \mathrm{cm^2/W})$		$n_2(10^{-20}\ \mathrm{cm^2/W})$			$n_2(10^{-20}\ \mathrm{cm^2/W})$	
	This Work	[76]	$n_{2,\mathrm{rot}}$	This Work	$n_{2,\mathrm{rot}}$	This Work	[76]	$n_{2,\mathrm{rot}}$	This Work	[76]
400	10.1±1.2	9.4	29	9.3±1.1	24	8.5±0.8	10.8	54	10.9±1.3	12.2
800	7.9±0.8	8.4	24	7.9±0.8	24	8.1±0.7	9.0	54	10.1±1.0	10.7
1250	7.7±0.7	8.2	23	7.9±0.8	24	8.9±0.7	8.8	54	10.5±1.0	10.5
1650	8.0±0.8	8.1	23	8.1±0.8	24	7.9±0.6	8.7	54	10.9±1.0	10.4
2200	7.2±0.8	8.1	23	7.4±0.8	24	8.2±0.8	8.6	54	9.3±1.0	10.4
2400	7.6±1.3	8.1	23	7.8±1.3	24	10.0±1.2	8.6	54	9.9±1.7	10.3

(a) Comparison is shown to values of n_2 calculated for our wavelengths using Eq. (3.3), where the coefficients a, b, and γ_0 were measured using the ESHG technique [77]. For long pulses, the effective nonlinearity coefficient can be written as $n_{2,eff} = n_2 + n_{2,rot}$.

(b) n_2 measurements are adjusted for $\Delta\alpha$ dispersion using coefficients found in [75].

(c) n_2 measurements are not adjusted for $\Delta\alpha$ dispersion. We used $\Delta\alpha(\omega_{800\mathrm{nm}})$, measured in [81], for all wavelengths.

(d) Referenced to N_2 measurements.

For the application of these results to propagation simulations, both the electronic and rotational contributions must be considered. For short pump pulses in N_2 and O_2 (<∼50 fs), the electronic response dominates, and for longer pulses (>∼150 fs), the rotational response dominates, as inferred directly from Figs. 3.2 and 3.3. In the limit of a very long pulse, the molecular response is adiabatic, and the effective nonlinearity coefficient can be written as $n_{2,\mathrm{eff}} = n_2 + n_{2,\mathrm{rot}}$, where calculated values of $n_{2,\mathrm{rot}}$ [82] from Eq. (3.4) (using our measured values of $\Delta\alpha$ [22]) are shown in Table 3.1.

$$n_{2,rot} = \frac{4\pi N(\Delta\alpha)^2}{15 n_0^2 c^2 \hbar B} \sum_j \frac{j(j-1)}{(2j-1)^2} \left(\frac{\rho_{j-2}^{(0)}}{2j-3} - \frac{\rho_j^{(0)}}{2j+1} \right) \tag{3.4}$$

3.4 Direct measurement of instantaneous nonlinear response in large bandgap solids at mid-IR wavelengths

Nonlinear propagation of ultrashort laser pulses—typically generated by Ti:Sapphire amplifiers centered at 800nm—in solids has been studied extensively due to its practical applications. For example, in [83] it is shown that due to self-phase modulation, intense multi octave supercontinua can be generated by strategically placing a series of thin fused silica windows in the focus of a high power laser pulse centered at 800nm. It was later reported [84] that this supercontinuum can be compressed to ~3fs FWHM using chirped mirrors.

Commercial optical parametric amplifiers (OPA) that extend the wavelength range of ultrashort Ti:Sapphire lasers into infrared are becoming increasingly available to researchers around the world, enabling study in regimes where transparent media be anomalously dispersive and the laser pulses may show soliton-like behavior [85]. Broadband infrared supercontinuum pulses are of particular interest in molecular spectroscopy and molecular fingerprinting where many molecules have rovibrational absorption lines [86]. In [87] Lanin *et al.* reported generating a 3-18μm sub-two-cycle supercontinuum pulse by focusing 2μJ of 150fs, 7.9μm laser pulse in a 5mm GaAs plate.

Another topic of intense research where mid-IR laser pulse propagation in solids is important is high-order harmonic generation (HHG) in bulk solids. A new regime of HHG has been reported in [88], where a ~3.2μm few-cycle mid-infrared laser pulse was focused into a 500μm ZnO wafer. It was shown in this work that the HHG cut-off frequency scales linearly with the driver electric field, where as in gases it scales quadratically.

Similar to the case of filamentation in air, essential to modeling and simulating these processes is accurate knowledge of the dispersion behavior of relevant nonlinearities as the wavelength of driving laser is tuned farther into the IR. In §3.3 we measured n_2 and its dispersion for air constituents, without the need for direct measurement of the pump intensity and interaction length, by using as a reference the rotational response of molecular gases.

Empirical relationships between the Kerr coefficient of a large bandgap solid and its linear refractive index and Abbe number have been proposed previously [89,90]. However, these estimates need to be tested, since the Abbe number is a measure of dispersion in the visible spectral range. The z-scan [31] technique has been the method of choice for measuring n_2 in solids and liquids; however it uses the assumption of Gaussian profiles both in time and space. Here, we use SSSI to directly measure the nonlinear Kerr coefficient in some of the large bandgap solids(fused silica, BK7, sapphire, CaF_2 and diamond) typically used in mid-IR applications, without making any assumption about temporal and spatial profile of the pulse. A difference between this section and §3.3 is that we measure intensity of the pump directly by imaging the pump focus on the sample using an InSb mid-IR camera (FLIR A6700sc, 1-5μm spectral range). Furthermore, we calibrated this camera so that its pixel counts correspond to mid-IR pulse energy. This allows us to determine the intensity profile of the pump beam as it enters the medium.

Fig 3.4 depicts the experiment setup in detail. The mid-IR pump is produced in an OPA by compressing ~9mJ out of a Legend Elite Duo Ti:Sapphire amplifier. The rest of the laser energy is used to generate broadband supercontinuum in the λ=450-

700nm range. A $\lambda/2$ waveplate is used to rotate the polarization of the Ti:Sapphire beam by 45º before entering the supercontinuum cell filled with 2.5atm of xenon.

Mid-IR wavelength tuning of the OPA is accomplished as follows.The computer-controlled motorized stages in the OPA tune the angles of the nonlinear crystals so that phase-matching conditions are satisfied for the user-specified wavelength. At any tuning point, the output of OPA contains both signal (within λ=1150nm-1600nm range, vertically polarized) and idler pulses (within the λ=1600nm-2600nm range, horizontally polarized), propagating collinearly. After passing through a separator (not shown in the figure) that selects signal or idler, the mid-IR pump beam is sampled using a thin wedged fused-silica window. The back reflection is routed to on the FLIR mid-IR camera to be used as an energy monitor, while the transmission through the wedge is focused at f/40 (confocal parameter= $2z_0$ ~ 2mm for λ=2μm) through the sample of interest using a 25cm CaF_2 lens. We used a Scientech calorimeter to calibrate the pixel counts of the FLIR camera to mid-IR energy at the focus. The pump and reference/probe are angled at ~2º with respect to each other, crossing as depicted in the inset of Fig.3.4 so that the probe overlaps with the pump over their full paths through the sample. The pump is blocked after passing through the sample. The transmitted probe is imaged on the slit of an imaging spectrometer (Horiba microHR). Before the probe reaches the slit, a polarizer cube splits the probe, whose polarization is oriented 45° with respect to the pump polarization, into vertical (s) and horizontal (p) component polarizations. The two polarizations are vertically separated by ~1mm on the spectrometer slit, with both channels probing the interaction region simultaneously. Whether the pump is the

signal or the idler, one of the channels records the probe when pump polarization|| probe polarizationand the other records the probe when pump $\perp$ probe.

In the case of thick (L = 0.5mm thickness) samples (e.g. CaF_2), we used the back reflection off of the front surface of the sample to from an image of the pump focal spot on a separate portion of the FLIR mid-IR camera. In the case of thinner samples (L < 0.3mm), the front and back surface reflections off of the samples where too close to each other, which made imaging the pump spot harder. Instead, in these cases after each run, we immediately swapped the sample under test with a 1mm fused silica slide and imaged the pump spot focus.

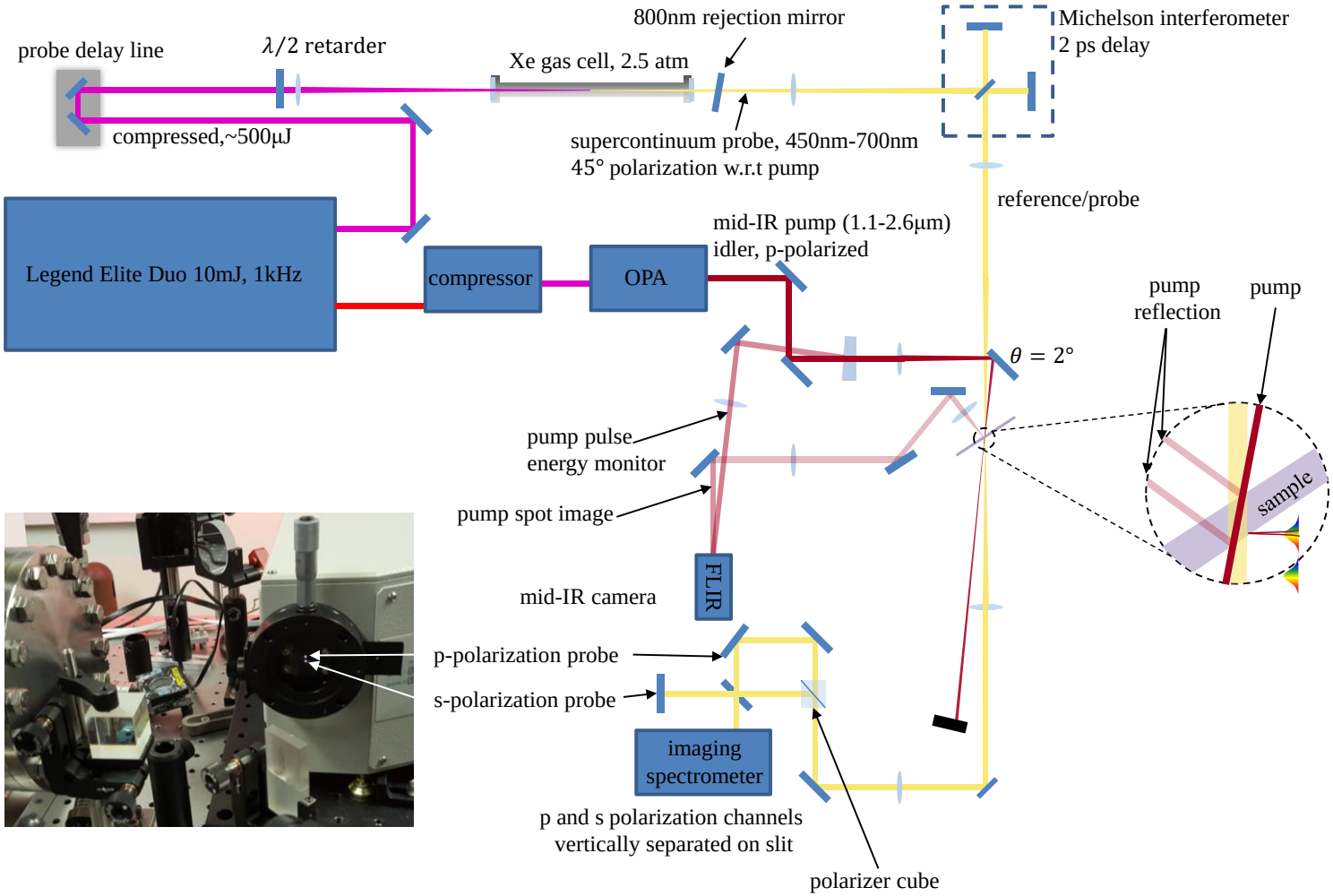

Figure 3.4. Experiment setup for direct measurement of n_2 in thin (L<0.3mm) solid samples. In this experiment we used an InSb camera to images the spot size of the pump focus. Furthermore, we calibrate the pixel counts on the camera to pump intensity. Both pump$\parallel$ probe and pump$\perp$ probe are recorded in the imaging spectrometer simultaneously.

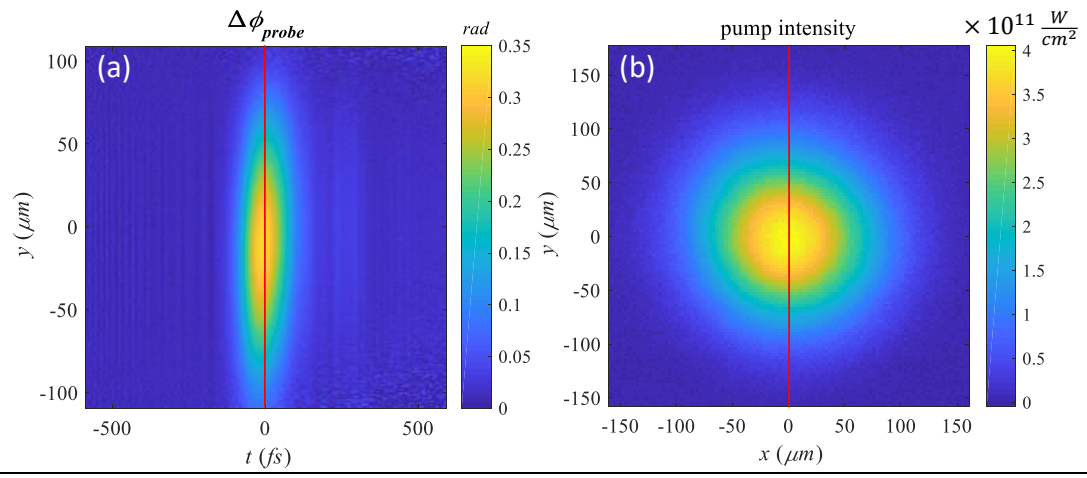

Figure 3.5. **(a)** Measured SSSI phase shift in 130 μm of sapphire at pump wavelength 2500 nm. **(b)** Image of the pump spot calibrated to show the pump intensity at t = 0.

SSSI traces are extracted for both pump || probe and pump ⊥ probe. Figure 3.5(a) shows an example of an extracted SSSI trace in sapphire, where the pump wavelength was set to 2500 nm and pump || probe. The pump focal spot image, a recorded by the FLIR camera is shown in Fig 3.5(b). A horizontal (temporal) lineout of the SSSI trace, denoted by $f(t)$, is normalized to have a peak of 1. The spatial profile of the pump spot $g(x, y)$ is also normalized to a peak of 1. The peak intensity of the pulse is then determined by $I_{peak} = E \Big/ \int g(x, y)\, f(t)\, dtdxdy$, where E is the pump pulse energy. This enables calibration of the pump spot image into a map of intensity at $t = 0$, and allows us to assign a peak intensity at each point along the center of the pump spot on $(x = 0, y)$, shown in Fig.3.5 as red vertical lines, The phase shift induced on the probe along $(x = 0, y)$ at $t = 0$ is given by

$$\begin{aligned} \Delta\varphi(y, t = 0) &= \int 2n_{2,elec} kI(y, z, t = 0)\, \mathrm{d}\, z \\ &\approx 2kn_{2,elec} I(y, t = 0)L, \end{aligned} \tag{3.4}$$

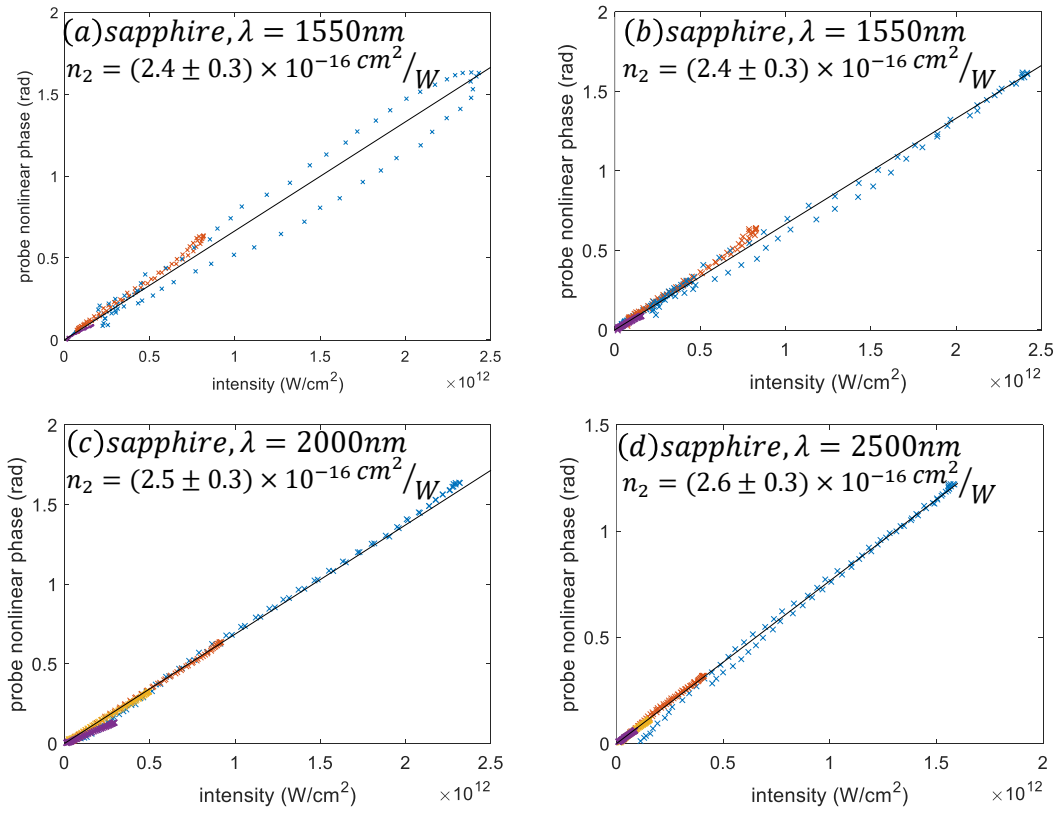

Figure 3.6. Measured SSSI phase shift in 130 μm of sapphire as a function of pump intensity for wavelengths **(a)** 1550nm, the loop present in the blue dataset is an indication that the origin $y = 0$ between $\Delta\varphi(y, t = 0)$ and $I(y, t = 0)$ was not chosen perfectly. Shifting the origin by a few pixel causes the loop to disappear as shown in part **(b)** with 1550nm, **(c)** 2000nm and **(d)**2500 nm. Each color corresponds to a dataset with varied pump energy. In each dataset, a × corresponds to a measured phase shift along the pump spot lineout

for $2z_0 > L$, where, k is the central wavenumber of the probe and L is the sample thickness. As an example, Fig. 3.6(a) shows measured phase lineout, $\Delta\varphi(y, t = 0)$, in sapphire plotted against $I(y, t = 0)$ for pump wavelength of 1550nm, when pump and probe have parallel polarization. Each color in the plot corresponds to a separate dataset in which the pump energy was changed. In each dataset $y = 0$ for $\Delta\varphi(y, t = 0)$ and $I(y, t = 0)$ was assigned to the peaks of the lineouts. Notice that the loop present in the blue dataset in Fig 3.6(a) shows that the alignment of the peaks was not perfect. Shifting the location of $y = 0$ in one of the curves (typically ~2 pixels) makes the

loop disappear, as shown in Fig 3.6(b). We can now determine the Kerr coefficient n_2 fitting a line on the data points as shown in Fig 3.6. Equation (3.4) suggests that the slope of this line is $2kLn_{2,elec}$ in which only $n_{2,elec}$ is unknown.

Table 3.2 summarizes the measured $n_{2,elec}$, and our estimated error bars. The main contributor to the error bars is the uncertainty in peak intensity measurement, due to ~ $5\mu m$ resolution in measuring the spot size. For isotropic media (fused silica and BK7) the ratio of the measured phase shift in the parallel channel to the measured phase shift in perpendicular channel is expected to be 3 [26] and was measured to be ~2.8 across the tested wavelengths. We suspect the main reason for this difference was misalignment of the parallel and perpendicular channels on the spectrometer slit. We also notice a drastic increase in the measured n_2 of BK7 as the pump wavelength approaches 2500nm, near its Raman absorption edge. Except for BK7, we do not observe any significant dispersion in measured Kerr coefficients.

Table 3.2 Measured $n_2 (1\times10^{-16}\,\mathrm{cm}^2/\mathrm{W})$ for solid samples

	1550 nm	**2000 nm**	**2500 nm**
Sapphire (random cut)	2.4±0.3	2.5±0.3	2.6±0.3
Diamond (CVD)	7.9±0.8	5.8±0.6	7.0±0.8
CaF_2	1.3±0.2	1.5±0.2	1.6±0.2
Fused Silica	2.2±0.2	2.0±0.2	2.3±0.2
BK7	2.6±0.3	2.1±0.3	3.5±0.3

3.5 Spatiotemporal characterization of ultrashort pulses from the near-IR- to the mid-IR

Characterization techniques for ultrafast laser pulses have been studied extensively, where techniques such as frequency resolved optical grating (FROG) [91] and spectral phase interferometry for direct electric-field reconstruction (SPIDER) [92] have been introduced. Some of these techniques require either nonlinear iterative extraction algorithms or detectors sensitive to harmonics of the pump. While silicon based image sensors are readily available for visible and near infrared lasers, this is not the case for longer wavelengths, where typical detectors are much more expensive and have lower resolution (owing to small number of pixels and large pixel sizes). In previous sections we have used SSSI to measure electronic, rotational and vibrational [93] nonlinearities of different solids and gases. Here we use SSSI to measure the spatiotemporal envelope of mid-IR pulses, employing the instantaneous electronic response in large bandgap $\chi^{(3)}$ media where the phase of the probe follows the envelope of the pump [94]:

$$\Delta\varphi(x_0, y, t) = 2k_p n_2 I_e(x_0, y, t) L \tag{3.5}$$

Here $\Delta\varphi$ is the probe phase shift, k_p is the central probe wavenumber, n_2 is the Kerr coefficient of the material I_e is the pump intensity and L is the thickness of the material. In this relation we assume $z_0 >> L$ to ignore propagation effects. Each SSSI measurement described above gives a 1D pump profile lineout along x_0, where x_0 is the horizontal location the probe sampled by the spectrometer slit. As shown in Fig. (3.7), in order to generate a 2D+1spatio-temporal profile (2D space plus time) of the pump, the probe is repeatedly scanned across the spectrometer entrance slit by a motorized tilt mount, resulting in a full $\Delta\varphi(x, y, t)$ map, which enables, with

knowledge of k_p, n_2 and L, direct extraction of $I_e(x,y,t)$. During scanning, the location of the probe beam relative to the slit is tracked by an auxiliary HeNe beamline and a tracking camera as depicted in Fig. 3.7.

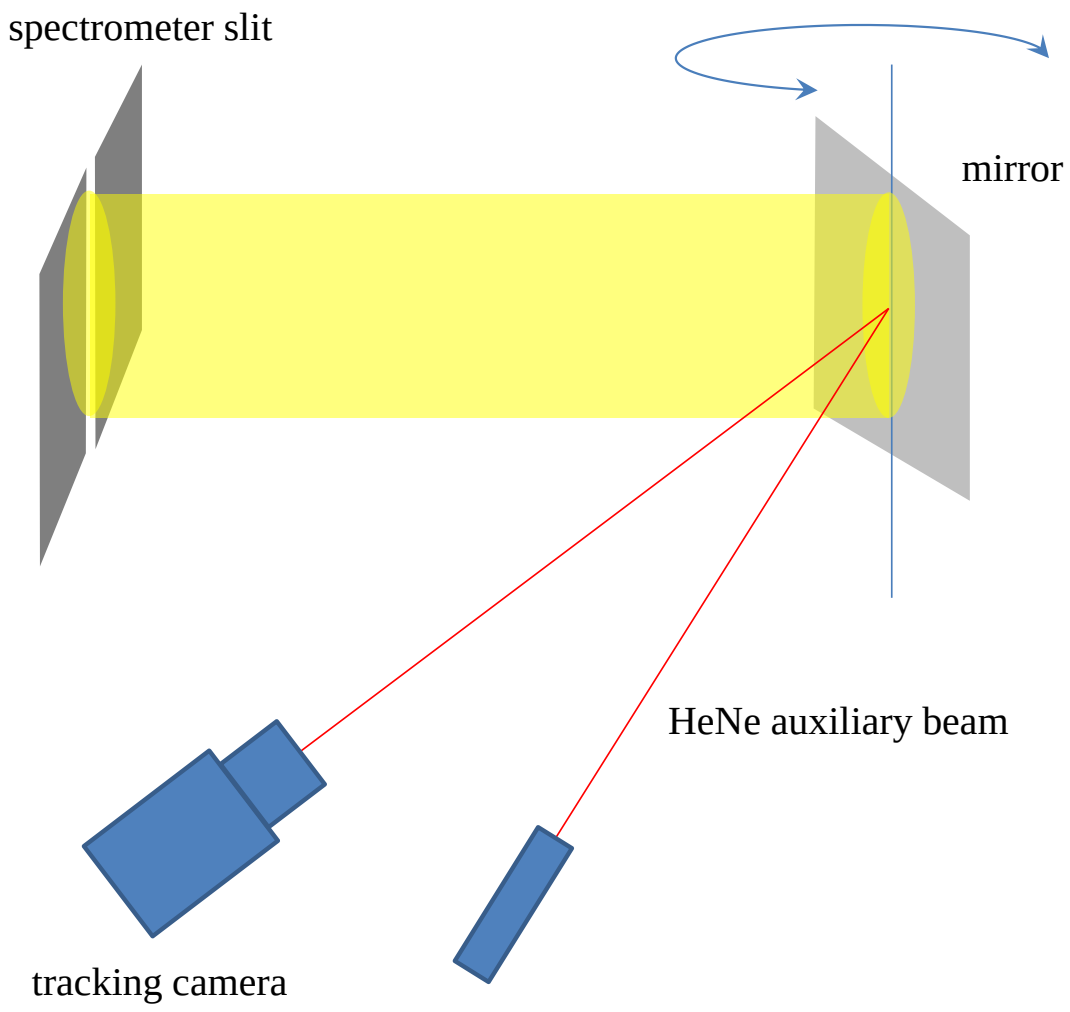

Figure 3.7. Scheme for recording 2D SSSI measurements by scanning the probe across the spectrometer slit. An auxiliary HeNe laser beam is used to track the location of the probe with respect to the slit

Note that all of this information is derived from the visible probe pulse (λ=400nm-700nm), where inexpensive silicon based 2D image sensors can be used. In our

technique, it is important to minimize pump-probe group velocity walk-off. This can be accomplished using very thin or low dispersion samples.

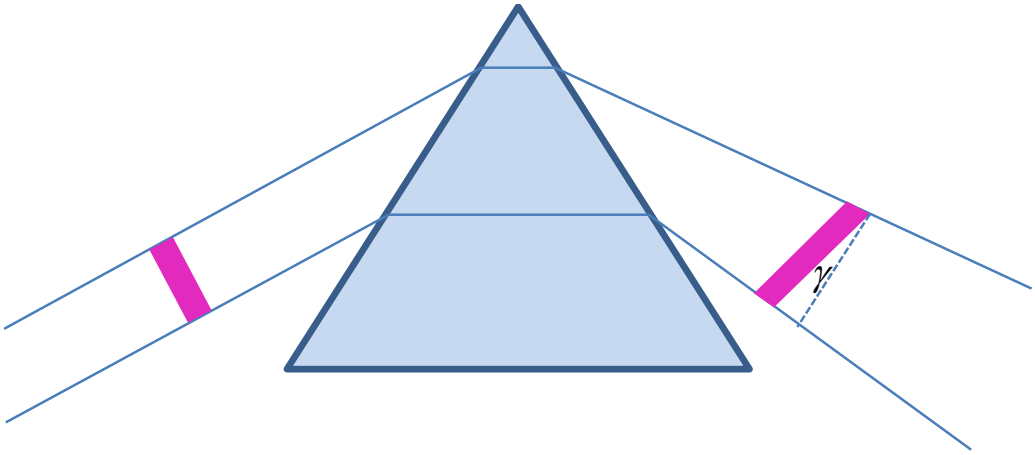

Figure 3.8. Creating a tilted pulse front using a prism.

We demonstrate our technique with two experiments. In the first experiment, we generate a tilted pulse front in a λ= 800 nm pulse, using a 69º prism [95]as shown in Fig. 3.8. Figure 3.9 (a) shows the temporal profile of an ultrashort pulse with a tilted pulse front.. For the target medium we used a 50μm thick BK7 window. Figure 1(b) and (c) shows the 2D spatial profile recovered from 2D SSSI data at , at *t*= -50fs and *t*=50fs (*t*=0 is the pulse peak). By directly imaging the pump spot on a silicon CCD camera, we verified that SSSI is recovering the correct pump spot image within the ~10 μm resolution of our direct imaging system.

Next we used our technique to characterize the profile of a λ=2600nm ultrashort pulse generated by an OPA, as shown in Fig 3.10. In this case we used a 100μm thick fused silica slide as the target SSSI medium (confocal parameter $2z_0 = 6\text{mm}$).

In conclusion, we have used single-shot supercontinuum spectral interferometry to measure the electronic Kerr coefficients for the major atmospheric constituents, N_2,

O_2 and Ar, at wavelengths ranging from 400 nm to 2400 nm. Our measurements are referenced to the polarizability anisotropy of the molecular gases, which enables extraction of absolute nonlinearities without the need for separate measurements of the gas density or pump intensity profiles. Except for the nitrogen and argon measurements at pump wavelength near 400 nm, the Kerr coefficients are measured to be dispersionless within the precision of our apparatus and consistent with the theoretical predictions. In addition, we measured Kerr coefficients in widely used materials sapphire, diamond, fused silica, BK7 and CaF_2 at mid-IR wavelengths. Finally we showed that SSSI can be used to measure the spatiotemporal profile of a laser beam in a broad range of wavelengths without the need for a detector sensitive in that range

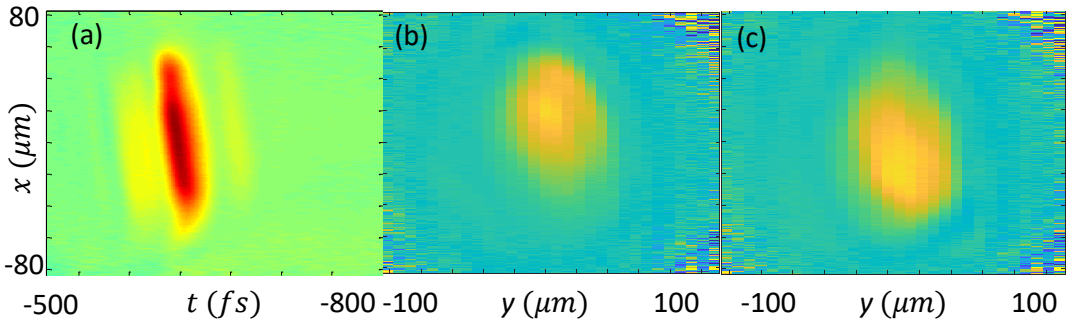

Figure 3.9. **(a)** Temporal profile of an 800nm pulse with tilted pulse front (deliberately introduced by passing it through a prism) **(b), (c)** spatial profile of the pulse at t= –50fs and t=50fs. If we integrate the 2D+1 data cube along its time axis we get the total spatial profile of the beam that agrees with the 2D image generated by a CCD camera.

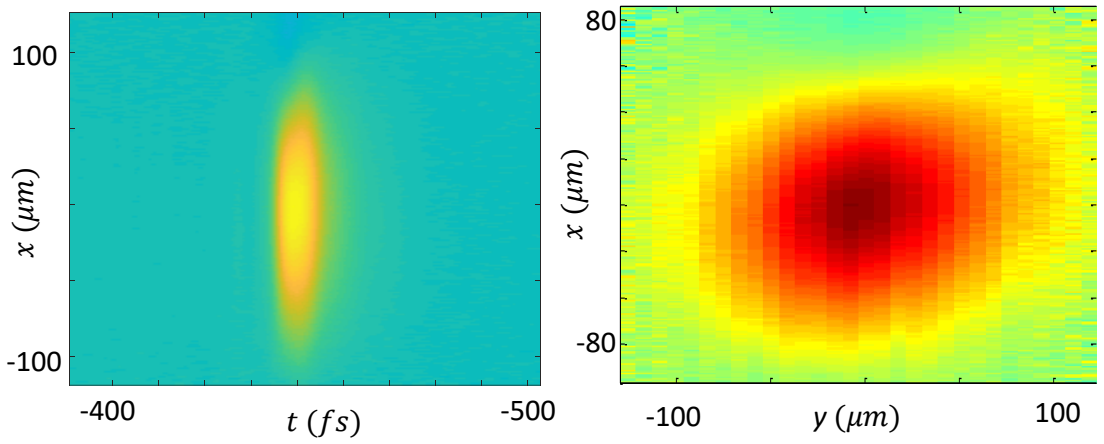

Figure 3.10.. Image of a mid-IR pulse centered at 2600nm at t = 0.

.

Chapter 4: Absolute measurement of the ultrafast nonlinear electronic and rovibrational response in H_2 and D_2

4.1 Introduction

Unlike in monoatomic gases, the nonlinear molecular response cannot be characterized by a single coefficient at a given frequency: processes at several timescales contribute, and so the response depends on pulse duration [29,59,96–99]. The high field nonlinear polarizability of diatomic molecules is a topic of practical and fundamental importance. From optical frequency conversion [4,19] to simulations and experiments in high intensity propagation [2,3,44,59,66,96,100], understanding the atomic and molecular behavior under high laser fields is crucial for applications involving beam propagation in air.

At the fastest timescale, the laser pulse width τ is shorter than the fundamental vibrational period and the fastest rotational response time, $\tau << \Omega_v^{-1} << \Delta t_{rot}$ where Ω_v is the fundamental vibrational frequency and $\Delta t_{rot} \sim 2T / j_{\max}(j_{\max}+1)$ is the fastest rotational timescale, where T and $j_{\max}$ are the rotational revival period and the quantum number of the maximally populated rotational state. Optical laser excitation of vibrational and rotational states can occur by two-photon Raman excitation, but for commonly used ~50-100 fs optical pump pulses, there is insufficient laser bandwidth ($\hbar\Delta\omega < 0.04$ eV) to excite vibrational modes in molecules of interest for atmospheric propagation ($\hbar\Omega_{v,N_2} \sim 0.3$ eV for N_2), and only rotational states are excited [29]. For example, $\hbar / \Delta t_{rot} \sim 0.03$ eV in N_2 where $j_{\max} \sim 10$ at room temperature. However, for femtosecond pulse filamentation in gases, significant pulse self-shortening and spectral broadening *can* occur so as to excite vibrational modes even in H_2 (in which

$\hbar\Omega_{v,H_2} \sim 0.5\,\mathrm{eV}$), driven by pulse spikes thought to be as short as several femtoseconds [101,102]. Nevertheless, to our knowledge there has never been a controlled experiment directly measuring full, time-resolved electronic and rovibrational nonlinear response of a light molecule.

Here, we use SSSI to measure the full absolute electronic and rovibrational nonlinear response of H_2 and D_2 to intense ultrashort optical pulses up to the ionization threshold of $\sim 10^{14}\,\mathrm{W/cm^2}$. The 40 fs pump pulse inducing the nonlinear response is sufficiently short to impulsively drive the rotational nonlinearity, but, on its own, cannot drive vibrational modes as discussed above. However, the vibrational component of the nonlinearity contributes to a two-beam coupling phase shift and energy transfer [103–105], even for a long pump pulse. We use this phase shift, which is independent of the amplitude of a sufficiently weak probe pulse, to also measure vibrational component of the optical nonlinearity.

The nonlinear response can be explored using single-beam experiment [97,99,106], but pump probe techniques allow direct time-resolved observation of the response [22,29,105,107,108] or the response reconstructed with an auxiliary model for pump spatiotemporal dependence [72,73,98]. Single-shot techniques, in particular, eliminate laser pulse-to-pulse fluctuations as a source of error [22,28,29,54,105,107,108]. However, it is crucial in pump-probe experiments to properly account for two-beam coupling effects, as shown for plasma and rotational nonlinearities [105]. Two-beam coupling for the case of vibrational nonlinearity is primary focus of this chapter.

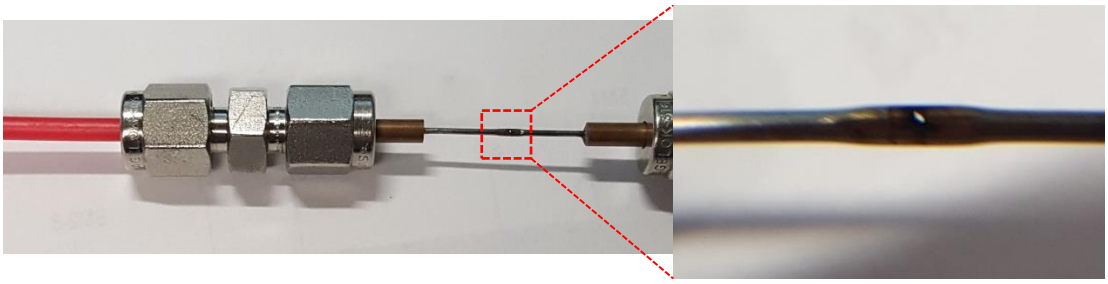

Figure 4.1. Thin gas flow tube. A hole is laser drilled in a stainless steel tube. The tube is crimped to achieve the desired thickness for the interaction between the gas and pump/probe pulses.

4.2 Experiment

The SSSI setup is similar to that discussed in earlier chapters, however the pump (800 nm, Ti:sapphire) and probe (supercontinuum, 450-700 nm) copropagate collinearly through the gas, either a thin laser drilled stainless steel gas flow tube in a vacuum chamber, or through the backfilled chamber without the tube. A photo of the thin gas tube is shown in Fig 4.1. The collinearly propagating pump and probe are separated by wavelength using a dichroic mirror that reflects the pump and transmits the probe. The absolute nonlinear change in refractive index $\Delta n(x,t) = (k_0 L_{eff})^{-1} \Delta\Phi(x,t)$ is then determined, where k_0 is the probe central wave number, L_{eff} is the effective gas interaction length, and $\Delta\Phi(x,t)$ is the space and time resolved phase shift extracted from the spectral interferogram. An example of the full nonlinear response measured by SSSI is shown in Fig. 4.2(a), which plots the phase shift $\Delta\Phi(x,t)$ measured for H_2 and D_2 in a backfilled chamber filled to ~0.3 atm for a peak pump intensity of ~46 TW/cm^2 and pulse width 40fs, where the probe pulse is polarized parallel or perpendicular to the pump. At this intensity the contribution of free electrons from ionization is negligible, without a detectable long timescale negative phase shift on the probe [107,108]. As can be seen, there is a prompt

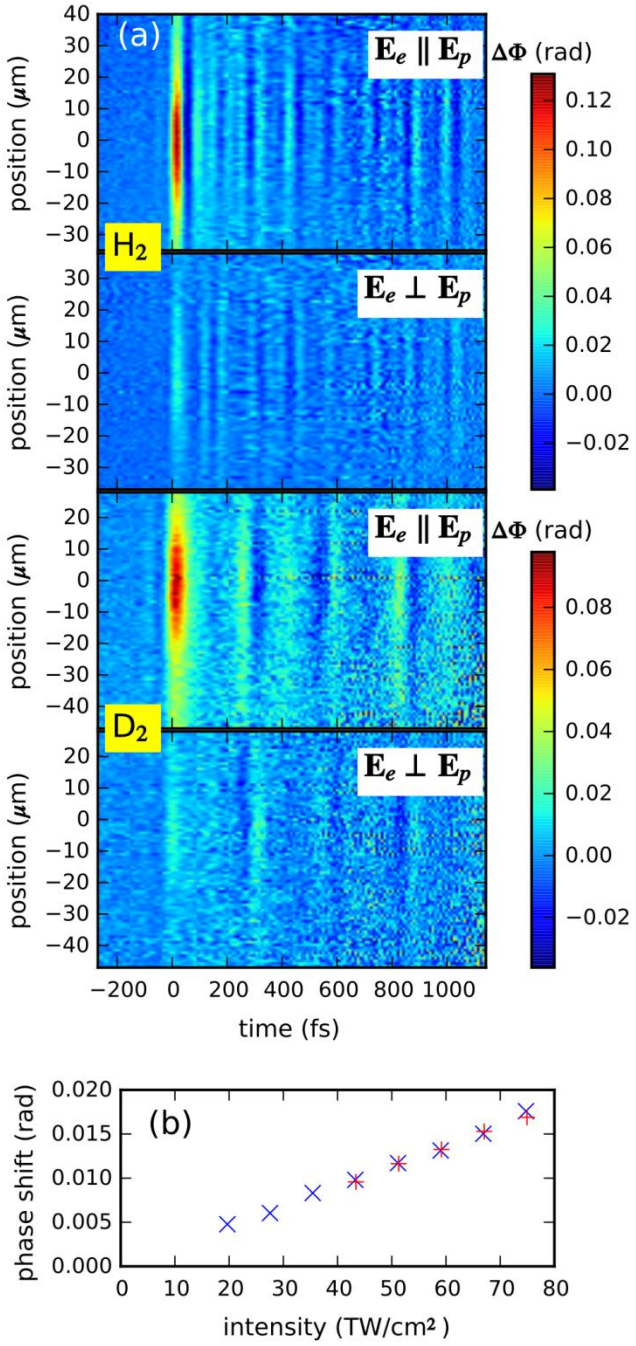

Figure 4.2. **(a)** Pump-induced 1D space- and time-resolved phase shift $\Delta\Phi(x,t)$ for a 46 TW/cm^2, 40 fs pulse in H_2 and D_2 for the pump $\mathbf{E}_e$ and probe $\mathbf{E}_p$ polarizations parallel and perpendicular. To increase the signal to noise [29], $\Delta\Phi(x,t)$ is extracted from the average of 200 single-shot interferograms. **(b)** Intensity dependence of the peak phase shift in H_2 (+) and D_2 (×) extracted from the spatial profile of the response $\Delta\Phi(x,t=0)$ for a pump pulse of peak intensity ~80 TW/cm^2

response near the center of the pump envelope at t = 0, with both electronic and vibrational contribution (to be discussed), followed by a modulated delayed response caused by beating of coherent superposition of quantized rotational states. For a peak pump intensity of ~80 TW/cm^2 (just below the ionization thresholds of H_2 and D_2) and a thin gas target to ensure a uniform axial pump intensity [22], we use the spatially varying pump intensity imprinted on $\Delta\Phi(x, t = 0)$ to plot the phase shift as a function of pump intensity for the probe pulse polarized parallel to the pump pulse in Fig. 4.2(b). As in N_2 and the noble gases [107,108], the prompt nonlinear response of H_2 and D_2 is linear in the intensity, with no saturation in electronic response observed below the ionization threshold, implying that the nonlinear coefficients measured in this paper apply up to that limit. The ionization threshold is defined as the peak intensity level at which we observed long lived negative probe phase shift above the noise floor [108].

4.3 Rotational Response

We first discuss the rotational response, as it solely contributes for times long after the pump pulse. In H_2 and D_2, it depends strongly on the pump pulse duration. The probe phase shift $\Delta\Phi(x = 0, t)$ is shown as a function of pump pulse width in Figs. 4.3(a) and 2(b) as solid curves, for fixed pump pulse energy of 34 μJ. For efficient excitation of a long-lived rotational coherence, the pump pulse width should be shorter than the characteristic response period. Here, for a Gaussian pulse of duration τ the efficiency of excitation of the $j \to k$ rotational coherence is proportional to

$e^{-\tau^2(E_j-E_k)^2/\hbar^2}$, and its contribution to the optical response depends on the initial population in states j and k [29] where the rotational energies, including the centrifugal correction, are $E_j = hcBj(j+1) - hcDj^2(j+1)^2$, where j is the rotational quantum number, B is the rotational constant, and D is the centrifugal constant. Note the reduced modulation amplitude of the rotational mode beating as the pump pulse duration increases; longer pulses become increasingly less efficient at exciting the rotational coherences. The discrete Fourier transform of $\Delta\Phi(x=0,t)$ for t > 200 fs for the shortest pulse width of ~40 fs is shown in Figs. 4.2(c) and 4.2(d). We observe the $j=0\rightarrow 2$ and $1\rightarrow 3$ transitions in both H_2 and D_2 and, additionally the $j=2\rightarrow 4$ and $3\rightarrow 5$ transitions in D_2.

In our determination of the absolute nonlinear response of H_2 and D_2 to intense fields, it is important to note that *all* parameters needed are provided by our SSSI measurements. For the rotational component of the response, the needed parameters are B, D and $\Delta\alpha = \alpha_{||} - \alpha_{\perp}$, the molecular polarizability anisotropy. First, the oscillation frequencies measured in Fig. 4.3(c) and 4.3(d) yield best fits of B = 58.9 (±3.0) cm^{-1}, D = 0.05 (±0.02) cm^{-1} for H_2, and B = 29.3 (±1.5) cm^{-1}, D = 0.021 (±0.008) cm^{-1} for D_2, in good agreement with the literature value [109,110]. The dominant source of uncertainty in the measurements of B and D is from the chirp of the probe pulse, which determines the mapping between frequency and pump-probe delay [28]. Quantum mechanical density matrix simulations [29,111] of the H_2 and D_2 rotational response (for t > 100 fs, after the prompt response) employing these values of B and D are shown in Fig. 4.3 as dashed lines, indicating excellent agreement.

Determination of $\Delta\alpha$, which scales the dependence of the rotational response on molecular polarizability—as $\Delta\alpha^2$— requires an absolute measurement of $\Delta n(x,t)$.

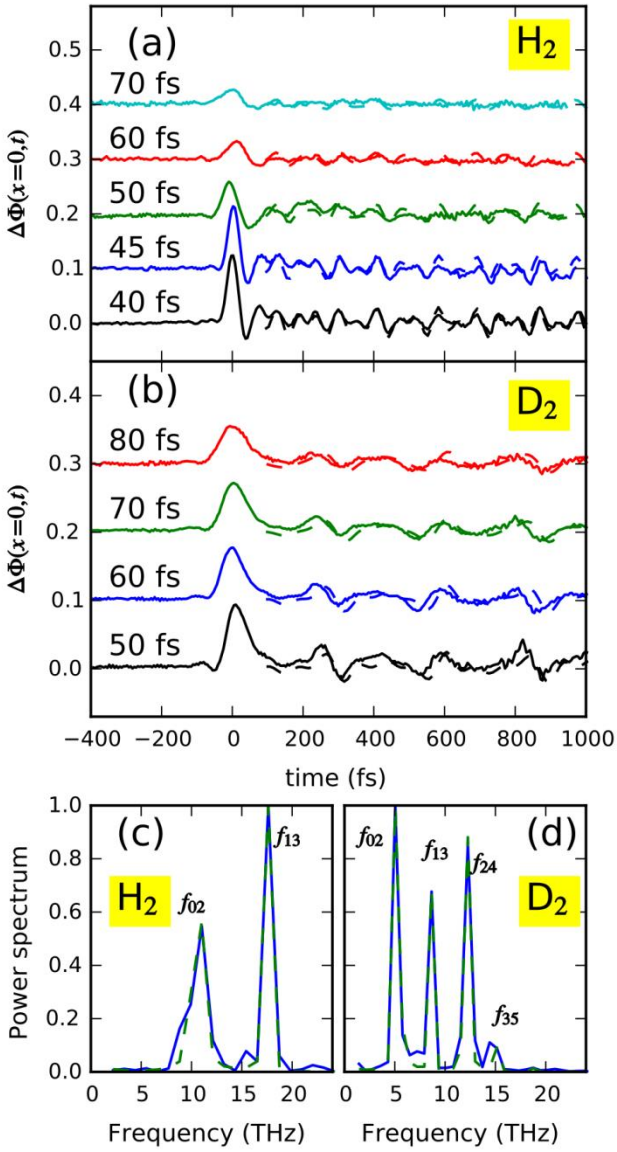

Figure 4.3. Experimental data on the rotational molecular response in H_2 and D_2. Time-dependent phase shift for $\mathbf{E}_e \parallel \mathbf{E}_p$ as a function of pump pulse duration for **(a)** H_2 and **(b)** D_2. Density-matrix simulations of the rotational phase response (using fitted values of the rotational constants as described in the text) are shown as dashed lines. The Fourier transform of the phase shift at times after the 40 fs pump pulse for **(c)** H_2 and **(d)** D_2, showing which rotational coherences are excited. The green dashed curves in (c) and (d) show the Fourier transform of the fitted density-matrix simulations.

Here, the experiment of Fig. 4.2 was repeated using a calibrated thin gas target [81] similar to the one shown in Fig 4.1, and the refractive index modulation for $t > 200$ fs was compared to density-matrix simulations [29,111] of the rotational response to arrive at best-fit values of $\Delta\alpha = (3.0 \pm 0.6) \times 10^{-25}\,\mathrm{cm}^3$ for H_2 and $\Delta\alpha = (3.0 \pm 0.4) \times 10^{-25}\,\mathrm{cm}^3$ for D_2. These values are in agreement with previous scattering-based measurements [112] and calculations [113].

4.4 Vibrational Response

The rotational contribution to the nonlinearity arises from the increased ensemble polarizability as the initially randomly oriented molecules are torqued into alignment with the optical field [29]. Similarly, a vibrational contribution arises from the optical force pushing the molecule's constituent atoms apart and is expressed as the dependence of the molecular polarizability tensor $\boldsymbol{\alpha}$ on changes in the internuclear separation, Q, $\boldsymbol{\alpha}(Q) = \boldsymbol{\alpha}(0) + (\partial\boldsymbol{\alpha}/\partial Q)Q$ for Q small compared to the equilibrium internuclear distance of < 1Å. The vibrational frequencies in H_2 and D_2 are in the ~100THz range, so to observe vibrational excitation directly (as we are able to do with the rotational excitation) one would need a few-cycle optical pulse, as discussed earlier. For a pulse longer than a few optical cycles, the vibrational response is *adiabatic*. The laser-induced molecular stretch Q and thus the stretch-induced change in the polarizability, is proportional to the pulse intensity, causing an effectively prompt response. One could, in principle, infer the size of the vibrational response by observing a reduced nonlinear refractive index for a few-cycle pulse compared with a longer pulse [106]. It appears impossible to distinguish the

vibrational nonlinearity from the electronic nonlinearity through pumping with a 40 fs pulse alone. However, we are able to separate them in another way. In a pump-probe experiment, interference between the pump and probe beams leads to the generation of a nonlinear refractive index grating, which modifies the nonlinear phase shift of the probe beam. This two-beam coupling phase shift is discussed in detail for the bound and free electronic and the rotational components of the optical nonlinearity in diatomic molecules [107]. Here, we use the two-beam coupling phase shift from rovibrational modes to measure the rovibrational component of the optical nonlinearity in H_2 and D_2.

We model the molecular interaction with a pump plus probe field $\mathbf{E}(\mathbf{r},\mathrm{t}) = \frac{1}{2}\left[\hat{\mathbf{e}}_e A_e(t) e^{i(\mathbf{k}_e\cdot\mathbf{r}-\omega_e \mathrm{t})} + \hat{\mathbf{e}}_p A_p(t) e^{i(\mathbf{k}_p\cdot\mathbf{r}-\omega_p \mathrm{t})}\right] + c.c$, where subscripts *e* and *p* refer to pump and probe, $A_e(t)$ and $A_p(t)$ are complex field envelopes (for a weak probe $\left|A_p / A_e\right| << 1$), and we define $\Delta\omega = \omega_p - \omega_e$. As described in [93], for an ultrashort optical pulse, the full rovibrational model [114] can be well approximated by replacing the *j*-dependent vibrational frequencies by a single vibrational mode of frequency Ω_v, so that the total vibrational nonlinear response appears as the polarization $\mathbf{P}^{vib}(t) = N\frac{\partial\alpha}{\partial Q}\langle Q\rangle_t \mathbf{E}$, where $\alpha = \frac{1}{3}\alpha_{\|} + \frac{2}{3}\alpha_{\perp}$, *N* is the molecular density, and $\langle Q\rangle_t$ is the time-dependent ensemble-averaged molecular stretch, given by

$$\langle Q\rangle_t \approx -\frac{1}{4\mu\Omega_v}\frac{\partial\alpha}{\partial Q}\int_{-\infty}^{t}\sin\left[\Omega_v(t'-t)\right]\left|\mathbf{E}(\mathbf{r},t')\right|^2 dt', \qquad (4.1)$$

where μ is the molecular reduced mass.

Inserting the expression for $\mathbf{E}(\mathbf{r},t)$ into eq.(4.1) and keeping slowly varying terms up to first order in the probe field, we find

$$\langle Q\rangle_t = \langle Q\rangle_t^s + \left(\langle Q\rangle_t^g\, e^{i\Delta\mathbf{k}\cdot\mathbf{r}} + c.c\right), \tag{4.2}$$

where $\Delta\mathbf{k} = \mathbf{k}_p - \mathbf{k}_e$, and

$$\langle Q\rangle_t^s = -\frac{1}{4\mu\Omega_v}\frac{\partial\alpha}{\partial Q}\int_{-\infty}^{t}\sin\left[\Omega_v(t'-t)\right]\left|A_e(t')\right|^2 dt' \ , \tag{4.3}$$

$$\langle Q\rangle_t^g = -\frac{1}{8\mu\Omega_v}\frac{\partial\alpha}{\partial Q}\int_{-\infty}^{t}\sin\left[\Omega_v(t'-t)\right]A_e^*(t')A_p(t')e^{-i\Delta\omega t'}dt'. \tag{4.4}$$

The superscripts *s* and *g* denote smooth and grating [94,115]. The former refers to the ensemble averaged stretch induced by the pump field only, and the latter refers to the stretch contribution induced by interference between the pump and probe fields. These stretch terms are the origin of the vibrational nonlinear response contributing to the polarization oscillating at frequencies near ω_p (which is measured in SSSI),

$$\mathbf{P}_p^{vib}(t) = N\frac{\partial\alpha}{\partial Q}\left[\langle Q\rangle_t^s\,\mathbf{A}_p(t)e^{i\mathbf{k}_p\cdot\mathbf{r}-i\omega_p t} + \langle Q\rangle_t^g\,\mathbf{A}_e(t)e^{i\mathbf{k}_p\cdot\mathbf{r}-i\omega_e t}\right]. \tag{4.5}$$

For pump pulses of duration longer than the vibrational period $2\pi\Omega_v^{-1}\sim 8-12$fs in H_2 and D_2, which applies to majority of ultrashort-pulse optical light sources, the vibrational response is effectively instantaneous. We therefore consider the probe instantaneous nonlinear polarization $\mathbf{P}_p^{inst}(t) = \chi_{eff}\mathbf{A}_p(t)e^{i(\mathbf{k}_p\cdot\mathbf{r}-\omega_p t)}$, where the effective nonlinear susceptibility χ_{eff} is related to the nonlinear index shift by $2\pi\chi_{eff} = \Delta n = n_2 I_e$, with n_2 split into electronic plus vibrational components: $n_2 = n_{2,elec} + n_{2,vib}$, with $n_{2,vib} = n_{2,vib}^s + n_{2,vib}^g$. Note that for a nonresonant electronic response, the smooth and

grating terms are the same, so $n_{2,elec} = n^s_{2,elec} + n^g_{2,elec} = 2n^s_{2,elec}$. The nonlinear refractive index for a weak probe pulse is a factor of 2 larger than that for pulse acting on itself [94].

To gain immediate physical insight, we first consider the limit of quasi-CW pulses. Then we have for the smooth component, using eq. (4.3),

$$\begin{aligned} \langle Q \rangle^s_t &= -\frac{1}{4\mu\Omega_v}\frac{\partial\alpha}{\partial Q}|A_e|^2 \int_{-\infty}^{t} \sin[\Omega_v(t'-t)]dt' \\ &= \frac{1}{4\mu\Omega_v^2}\frac{\partial\alpha}{\partial Q}|A_e|^2, \end{aligned} \tag{4.6}$$

and for the grating term, using eq (4.4),

$$\begin{aligned} \langle Q \rangle^g_t &= -\frac{1}{4\mu\Omega_v}\frac{\partial\alpha}{\partial Q}A_e^* A_p \int_{-\infty}^{t} \sin[\Omega_v(t'-t)]e^{-i\Delta\omega t'}dt' \\ &\approx \frac{1}{4\mu\left(\Omega_v^2 - \Delta\omega^2\right)}\frac{\partial\alpha}{\partial Q}A_e^* A_p e^{-i\Delta\omega t}. \end{aligned} \tag{4.7}$$

These expressions then yield

$$n^s_{2,\mathrm{vib}} = \frac{4\pi^2 N}{n_0 c\mu\Omega_v^2}\left(\frac{\partial\alpha}{\partial Q}\right)^2, \tag{4.8}$$

and

$$n^g_{2,\mathrm{vib}} = \frac{4\pi^2 N}{n_0 c\mu\left(\Omega_v^2 - \Delta\omega^2\right)}\left(\frac{\partial\alpha}{\partial Q}\right)^2. \tag{4.9}$$

Note that the vibrational nonlinear response picked up by the probe is greatly enhanced by the grating term $n^g_{2,\mathrm{vib}}$ for $\Delta\omega \sim \Omega_v$, and we exploit the dependence on $\Delta\omega/\Omega_v$ of this resonant two-beam coupling effect to measure the vibrational component of the refractive index. We note that in continuous-wave experiments, it is well known that the vibrational nonlinearity depends strongly on such resonant coupling [76,116]. Here, we use the effect in the ultrafast domain to separate the

electronic and vibrational contributions to the prompt nonlinearity. The expression above for $n_{2,\mathrm{vib}}^{g}$ is singular when $\Delta\omega = \Omega_v$ because of the assumption of infinitely long pulses. For a long, finite pump pulse of the form $A_e(t) = A_{e0}e^{-t^2/2t_e^2}$ (where $t_e \gg \Omega_v^{-1}$), it is straightforward to derive a well-behaved expression for the grating vibrational nonlinearity by integrating Eq. (4.4),

$$n_{2,\mathrm{vib}}^{g} = \frac{4\pi^2 N t_e}{n_0 c \mu \Omega_v}\left(\frac{\partial\alpha}{\partial Q}\right)^2 \left[\mathrm{F}\left(t_e\left(\Delta\omega - \Omega_v\right)\right) - \mathrm{F}\left(t_e\left(\Delta\omega + \Omega_v\right)\right)\right], \qquad (4.10)$$

where $\mathrm{F}(x)$ is the Dawson function.

A very useful representation of our resonant two-beam coupling results is a two-dimensional (2D) plot of SC probe spectral phase shift vs $\Delta\omega = \omega_{p,overlap} - \omega_e$, where $\omega_{p,overlap}$ is the probe frequency which overlaps in time with the pump pulse, as shown schematically in Fig. 4.4(a). Measurements and simulations of SC probe phase shift vs $\Delta\omega$ in H_2 are shown in Fig. 4.4(b), and those for D_2 are shown in Fig. 4.3(c). The time delay of the SC frequency component at ω (left axes) is given by $\phi'(\omega)$, where $\phi(\omega)$ is the chirped SC spectral phase. For each value of $\Delta\omega$, scanning top to bottom in the plots (negative to positive delay) shows the SC phase shift abruptly changing as the molecular nonlinearity is excited by the arriving pump pulse. The initial perturbation is dominated by the electronic and vibrational response, followed at longer times by rotational revivals. Near $\Delta\omega \sim 0.78\,\mathrm{fs}^{-1}$ in H_2 ($\lambda_{p,overlap} = 600\,\mathrm{nm}$) and $\Delta\omega \sim 0.55\,\mathrm{fs}^{-1}$ in D_2 ($\lambda_{p,overlap} = 645\,\mathrm{nm}$), the phase changes strongly, consistent with resonant two-pulse coupling with molecular resonances between the ground and first vibrational excited states. The frequency of the n^{th} vibrational state is given by

$\omega_n = (n+\frac{1}{2})\omega_e - (n+\frac{1}{2})^2 \omega_e x_e$, where ω_e (not to be confused with the pump central frequency) is the harmonic frequency and $\omega_e x_e$ is the first anharmonicity

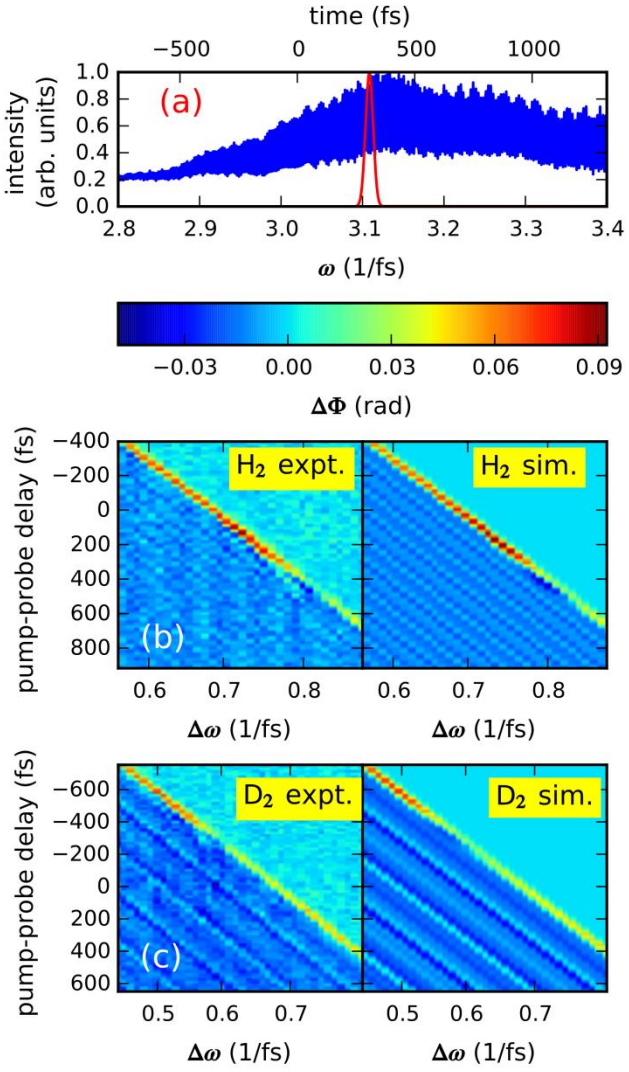

Figure 4.4. Phase shift of chirped SC probe vs $\Delta\omega = \omega_{p,overlap} - \omega_e$.The measured probe spectral phase is $\varphi(\omega) = \beta_2(\omega-\omega_0)^2 + \beta_3(\omega-\omega_0)^3$, with $\beta_2 = 1675\,\mathrm{fs}^2$, $\beta_3 = 396\,\mathrm{fs}^3$ and $\omega_0 = 3.05\,\mathrm{fs}^{-1}$. The time delay of SC frequency component at ω (left axes) is given $\phi'(\omega)$. **(a)** Supercontinuum interference spectrum with variably delayed pump pulse superposed. The top axis shows the time corresponding to each frequency component. **(b)**Experimental and best fit rovibrational simulation plots for **(b)** H_2 and **(c)** D_2. The best-fit simulations enabled extraction of $n_{2,\mathrm{elec}}$ and $\partial\alpha/\partial Q$, shown in Table 4.1.

constant [109]. In H_2, $\omega_e = 0.829\,\mathrm{fs}^{-1}$ and $\omega_e x_e = 0.023\,\mathrm{fs}^{-1}$,and in D_2, $\omega_e = 0.567\,\mathrm{fs}^{-1}$ and $\omega_e x_e = 0.012\,\mathrm{fs}^{-1}$ [58]. For the ground to first excited vibrational state transition, $\Omega_v = \omega_e - 2\omega_e x_e$, so the resonance is predicted to occur at $\Omega_v = 0.783\,\mathrm{fs}^{-1}$ in H_2 and $\Omega_v = 0.543\,\mathrm{fs}^{-1}$ in D_2, consistent with our experimental data.

Table 4.1. Measured electronic Kerr coefficient $n^s_{2,\mathrm{elec}}$ at 1 atm (at probe wavelength of 600 nm and pump wavelength of 800 nm), polarizability anisotropy $\Delta\alpha$, and polarizability derivative $\partial\alpha/\partial Q$. A comparison is made with previous experimental and theoretical work. The rightmost column shows n_2 estimates at 1 atm based on our experimental results for a long pulse at 800 nm.

Gas	$n^s_{2,elec}$ (10^{-20} cm^2/W)		$\Delta\alpha$ (10^{-25} cm^3)		$\partial\alpha / \partial Q$ (10^{-16} cm^2)			n_2 at 800 nm (10^{-20} cm^2/W)		
	This expt.	[76]	This expt.	[112]	This expt.	[113]	[117]	$n_{2,rot}$	$n_{2,vib}$	$n_{2,tot}$
H_2	6.5±1.0	6.37	3.0±0.6	3.14	1.3±0.2	1.24	1.3±0.2	2.8	1.2	10.3
D_2	5.8±1.3	6.20	3.0±0.4	2.99	1.4±0.3		1.22±0.1	3.7	1.1	10.4

4.5 Extraction of nonlinear coefficients

We previously found the rotational response parameters $\Delta\alpha$, B and D from the response at time delays following the pump pulse. Fitting the one-mode vibrational simulation to the measurements in Fig. 4.4 now enables extraction of the two remaining nonlinear coefficients, $n_{2,\mathrm{elec}}$, and $\partial\alpha/\partial Q$. The best-fit coefficients are listed in Table 4.1, with their associated simulation results shown in the right-hand panels of Figs. 4.4(b) and 4.4(c). The $n_{2,\mathrm{elec}}$ and $n_{2,\mathrm{vib}}$ values we find are consistent with previous measurements using long, low-intensity pulses based on harmonic generation [77], the optical Kerr effect [118], and coherent anti-Stokes Raman scattering [119], and the values of $\partial\alpha/\partial Q$ are consistent with previous calculations [113]and Raman scattering measurements [117]. The most important source of error is the determination of the pump laser intensity, which relies on accurate measurement of the spatial pump beam profile at the gas target.

The total nonlinear refractive index $2n^s_{2,elec} + n^s_{2,vib} + n^g_{2,vib}$ experienced by the probe in H_2 is plotted as a function of $\Delta\omega$ in Fig. 4.5(a), as calculated for a 40 fs pump pulse and a broad chirped SC probe, both using the analytical expression [eq. (4.10)] and calculated numerically. The electronic and vibrational parameters are taken from Table 4.1. The electronic component of the nonlinear index $2n^s_{2,elec}$ is shown as a red dashed line for comparison. In both H_2 and D_2, the vibrational Kerr effect is responsible for ~16% of the total (instantaneous) nonlinear refractive index for a 40 fs pulse. Electronic, rotational, and vibrational values of n_2 for a long pulse are given in the rightmost columns of Table 4.1. For pulses longer than ~40 fs in H_2 and ~100 fs

in D_2, the rotational response becomes adiabatic and the long pulse values can be used. While the vibrational nonlinearity is quite small in the visible and near infrared, in the mid-infrared there is a resonance when the optical frequency is near $\Omega_v/2$. This is shown in Fig. 4.5(b). This may have important implications for the propagation of mid-infrared pulses in the atmosphere near $10\mu\text{m}$ [23].

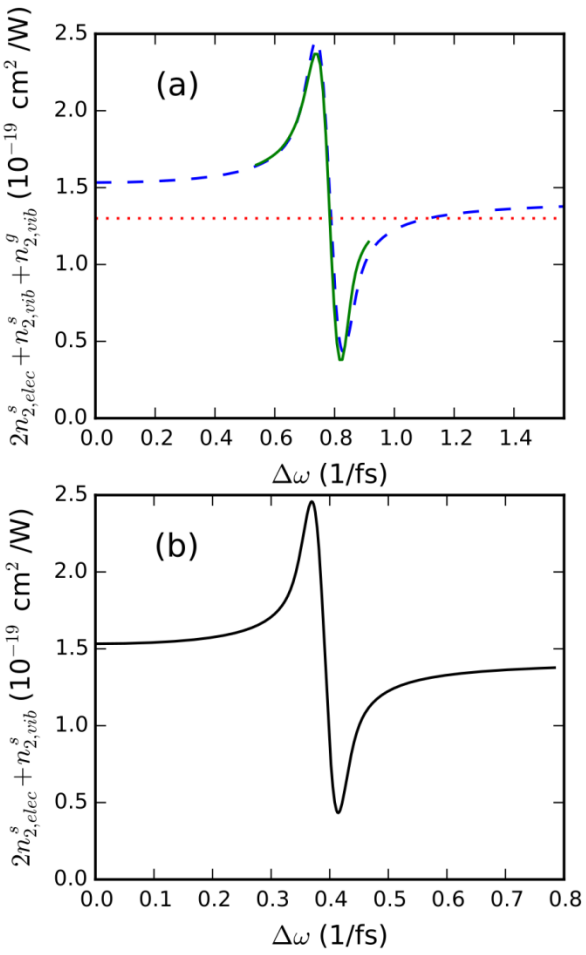

Figure 4.5. **(a)** Calculated nonlinear index $2n^s_{2,elec}+n^s_{2,vib}+n^g_{2,vib}$ experienced by the probe as a function of the pump-probe beat frequency $\Delta\omega$ for a 40 fs pulse centered at 800 nm, calculated using Eq. (4.10) (dashed blue) and for and calculated numerically (solid green). The electronic component $2n^s_{2,elec}$ is shown as a red dotted line for comparison. **(b)** Calculated nonlinear index $n^s_{2,elec}+n^s_{2,vib}$ for an infrared pulse. The vibrational nonlinearity is resonant for optical frequency near $\Omega_v/2$.

In summary, we have demonstrated single shot measurement of the full absolute

electronic and rovibrational nonlinear response of H_2 and D_2 to intense ultrashort optical pulses up to the ionization threshold of ~10^{14} W/cm^2. The presence of the electronic, rotational, and vibrational contributions all in one set of 2D experimental traces enables the determination of the relative contribution of each to the nonlinear response. Importantly, one does not need a few femtosecond pump pulse to excite the vibrational nonlinearity; our pump-probe configuration promotes its excitation through two-beam coupling, even for much longer pump pulses. The nonlinear coefficients measured are applicable over a very wide range of laser pulse widths and intensities below the ionization threshold, and because they apply to the very simplest molecules they constitute a fundamental benchmark for theory and simulation.

Chapter 5: Bound electron nonlinearity beyond the ionization threshold

5.1 Introduction

Field ionization is an extremely nonlinear process that plays a central role in any experiment or application involving propagation of intense optical pulses. It is integral to the process of high harmonic generation and is important to its phase matching [120,121]. It leads to extremely wide bandwidths in supercontinuum generation [122], which can be applied to single cycle pulse generation [123] and ultrafast spectral interferometry [28]. In many situations, field ionization is the mechanism for optical beam collapse arrest in femtosecond filamentation [2,3,124]. For femtosecond laser pulses, the onset of ionization occurs in the intensity regime where multiphoton ionization transitions to tunneling ionization, as the optical field goes from being a small perturbation on the atomic potential to being of comparable strength.

Prior measurements of the ionization of atoms and molecules by intense ultrashort optical pulses have been performed in vacuum chambers at very low pressure by directly capturing the ionization byproducts (electrons and ions) long after the ionizing pulse has passed through the interaction volume, approximately the beam waist region [125–128]. Measurements in atomic hydrogen can be benchmarked to an essentially exact theory [128], and measurements in multi-electron atoms and molecules [125–127] were found to agree with relatively simple single-active-electron theories to within a factor of ~2. Even so, because the electron/ion generation is integrated over the time and space dependence of the laser

pulse, analysis of such measurements demands auxiliary simulation of ionization in an assumed time-and space-dependent field.

Understanding intense light pulse propagation in material media requires knowledge of its absolute nonlinear response through the ionization transition. Because atoms and molecules in this intensity regime are exposed to highly nonperturbative fields, there has been considerable discussion about the effect on nonlinear propagation. In particular, debate has arisen (see [129] and references therein) regarding potentially exotic contributions to the atomic dipole moment, wherein strongly driven bound electrons have been speculated to exhibit a negative polarizability. The results we present in this chapter likewise address this issue.

Employing SSSI, we measure the transient ionization rate induced by an intense laser pulse in a particular gas species by recording the space- and time-dependent phase shift imposed on a probe pulse. Knowledge of the spatio-temporal phase shift, gas density, and medium thickness allows extraction of the absolute transient nonlinear response, which includes the nonlinear polarizability and ionization rate. SSSI, combined with a measurement of the linear phase shift through the target using folded wavefront interferometry, which yields the product of the mean gas density and effective gas target thickness L_{eff} [22], allows us to determine the transient nonlinear shift in refractive index absolutely. This method has been used to measure the nonlinear index of refraction in gases at intensities up to the ionization threshold [22,93,108]; here we measure the response at intensities where the ionization phase shift is comparable to the bound electronic phase shift.

5.2 Experiment Setup

A diagram of the experiment is shown in Fig. 5.1, and is similar to the one we used in Chapter 4. To measure the phase shift in two spatial dimensions and time, the probe beam image is swept across the entrance slit of the imaging spectrometer over a high repetition rate multi-shot scan as discussed in §3.5. For this experiment, up to ~0.5 mJ is focused by a 75 cm focal length lens to a spot size of 65 μm. The other 10% of the amplifier output is compressed by the internal compressor and focused into a Xe gas cell, generating supercontinuum covering the range 500-700 nm. This is split into probe and reference pulses using a Michelson interferometer and sent into the vacuum chamber, focused by a 50 cm focal length lens to a spot size of ~200 μm, which overfills the hole in the target. The pump and probe beams are linearly polarized and have parallel polarization. The probe pulse spectral phase is characterized by time-dependent cross phase modulation [30]. The spectral phase is well fit by $\phi_s(\omega) = \beta_2(\omega-\omega_0)^2 + \beta_3(\omega-\omega_0)^3$, where $\beta_2 = 1050\text{fs}^2$ $\beta_3 = 100\text{fs}^3$ and $\omega_0 = 3.15\text{fs}^{-1}$.

The gas target (similar to the one showed in Fig 4.1) is a flattened metal gas flow tube with a laser-drilled hole mounted inside a vacuum chamber. A roots pump maintains a background chamber pressure of <1 mbar (~100 Pa). The flow gas pressure (density) is adjusted to maximize the probe phase shift while limiting ionization-induced refraction of the pump and probe. Typically this demanded running at lower gas pressure at high laser intensities and at higher pressure for lower laser intensities. The effective gas target thickness is $L_{eff} = \int (N(z)/N_0)dz \sim 450\mu m$, where $N(z)$ is the gas density profile along the pump/probe path through the gas tube

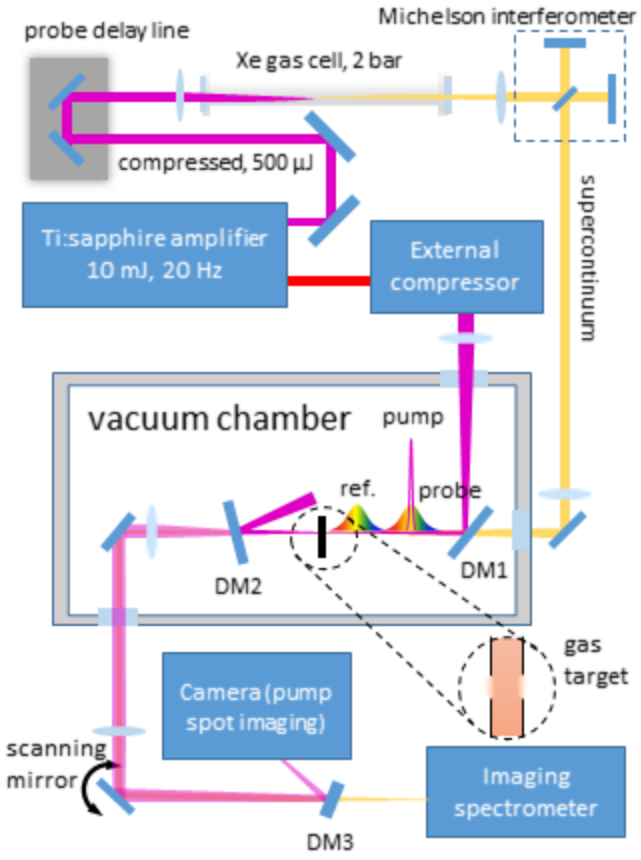

Figure 5.1. Experimental apparatus for 2D+1 SSSI measurement of field-induced ionization. Not shown: 800 nm rejection mirror after Xe gas cell, auxiliary interferometer for gas target characterization, and pre-target pump spot imaging camera. DM1, DM2, DM3: dichroic mirrors.

hole and N_0 is the profile mean density. L_{eff} is much smaller than the pump and probe confocal parameters of 30 mm and 200 mm respectively, ensuring that the pump intensity is independent of the axial coordinate within the gas, improving the time resolution [28]. As discussed in §3.5, in 2D+1 SSSI, the pumped spot in the gas target is imaged, as in standard SSSI, to the entrance slit of an imaging spectrometer. We define the axis parallel (perpendicular) to the slit as x (y). A motorized scanning mirror downstream of the second imaging lens translates the probe/reference beam image in the y direction. Each shot captured is a probe/reference interferogram in ω and x at a particular value of y (= y_i, say). Interferograms are averaged over 100 shots

before extraction to significantly improve the signal-to-noise ratio [54]. Similar to 1D SSSI, the extracted spectral phase shift $\Delta\varphi(x, y_i, t)$ is then used to determine $\Delta\Phi(x, y_i, t)$ [30] for each i. A three dimensional map of the nonlinear response $\Delta\Phi(x,y,t)$ is built by scanning y. A total of ~10000 shots are used to construct $\Delta\Phi(x,y,t)$. For each laser shot, an image of the pump spot is also captured, enabling measurement of y_0 as the probe beam is swept back and forth, and allowing post-collection compensation in the data analysis of pump beam intensity and pointing fluctuations.

Temporal slices of the extracted phase shift $\Delta\Phi(x,y,t)$ in Ar are shown in Fig. 5.2 for a 42 fs pump pulse of peak intensity 95 TW/cm^2. Unlike in our previous results [108], these new measurements are absolute and quantitative at intensities where ionization is observed. This required increasing the pump spot size to minimize lensing of the pump and probe by the plasma transverse gradient, increasing the time between pump pulses to 100 ms to avoid cumulative thermal effects in the gas [107], and improving the temporal resolution of SSSI by minimizing the probe chirp (consistent with the desired temporal window) and optimizing the spectrometer resolution [30]. Similar temporal slices for Kr, Xe, N_2 and O_2 are shown in figures 5.3-5.6. The bound electronic response is relatively larger in Kr and Xe than in Ar, but otherwise the results are qualitatively similar. The molecular gases N_2 and O_2 have an additional delayed rotational response that peaks ~80 fs after the peak of the pump pulse [22,29].

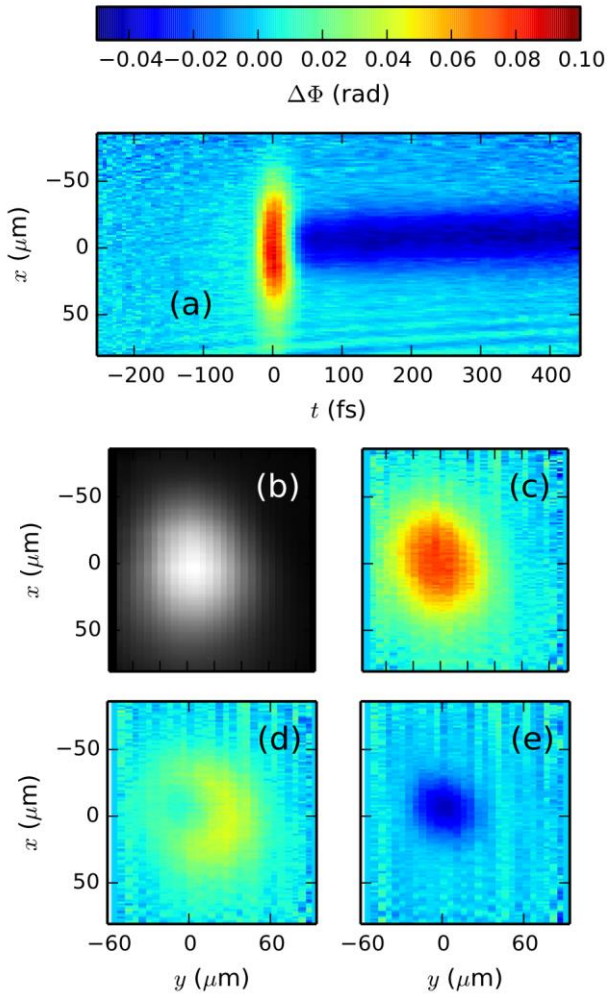

Figure 5.2. Results in Ar for peak pump intensity of 95 TW/cm2 and pulsewidth 42 fs. **(a)** Measured spatiotemporal phase shift $\Delta\Phi(x,y_0,t)$. **(b)** An image of the pump spot at the gas target. **(c)** The phase shift $\Delta\Phi(x,y,t$ =–14 fs), showing mostly the Kerr response. **(d)** Phase shift $\Delta\Phi(x,y,t$ =+25 fs), showing the Kerr response on the wings and the growing plasma contribution in the center of the beam. **(e)** Phase shift $\Delta\Phi(x,y,t$ =+100 fs), showing the dominant plasma contribution after the pump pulse. The peak of the pump pulse defines zero for the *x*, *y*, and *t* coordinates.

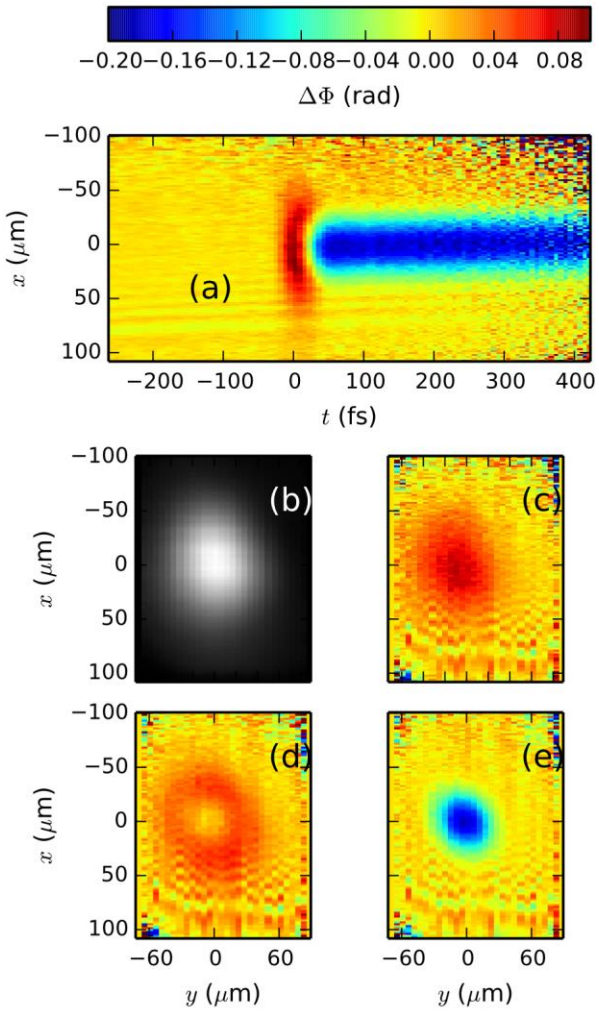

Figure 5.3. Results in Kr at a pump peak intensity of 84 TW/cm^2. **(a)** Measured spatiotemporal phase shift $\Delta\Phi(x,y_0,t)$. **(b)** An image of the pump spot at the gas target, showing that the Kerr response simply follows the pump intensity profile. **(c)** The phase shift $\Delta\Phi(x,y,t_0 - 14$ fs), showing mostly the Kerr response. **(d)** The phase shift $\Delta\Phi(x,y,t_0+21$ fs), showing the Kerr response on the wings and the growing plasma phase shift in the center of the beam. **(e)** The phase shift $\Delta\Phi(x,y,t_0+100$ fs), showing the negative plasma phase shift long after the pump pulse.

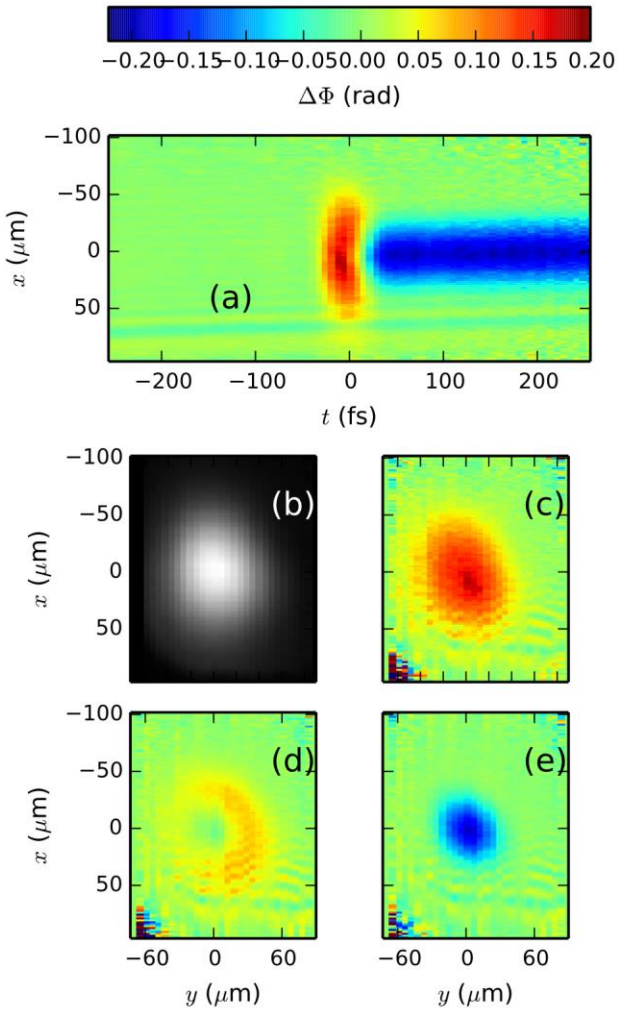

Figure 5.4. Results in Xe at a pump peak intensity of 50 TW/cm^2. **(a)** Measured spatiotemporal phase shift $\Delta\Phi(x,y_0,t)$. **(b)** An image of the pump spot at the gas target, showing that the Kerr response simply follows the pump intensity profile. **(c)** The phase shift $\Delta\Phi(x,y,t_0-14$ fs), showing mostly the Kerr response. **(d)** The phase shift $\Delta\Phi(x,y,t_0+14$ fs), showing the Kerr response on the wings and the growing plasma phase shift in the center of the beam. **(e)** The phase shift $\Delta\Phi(x,y,t_0+100$ fs), showing the negative plasma phase shift long after the pump pulse..

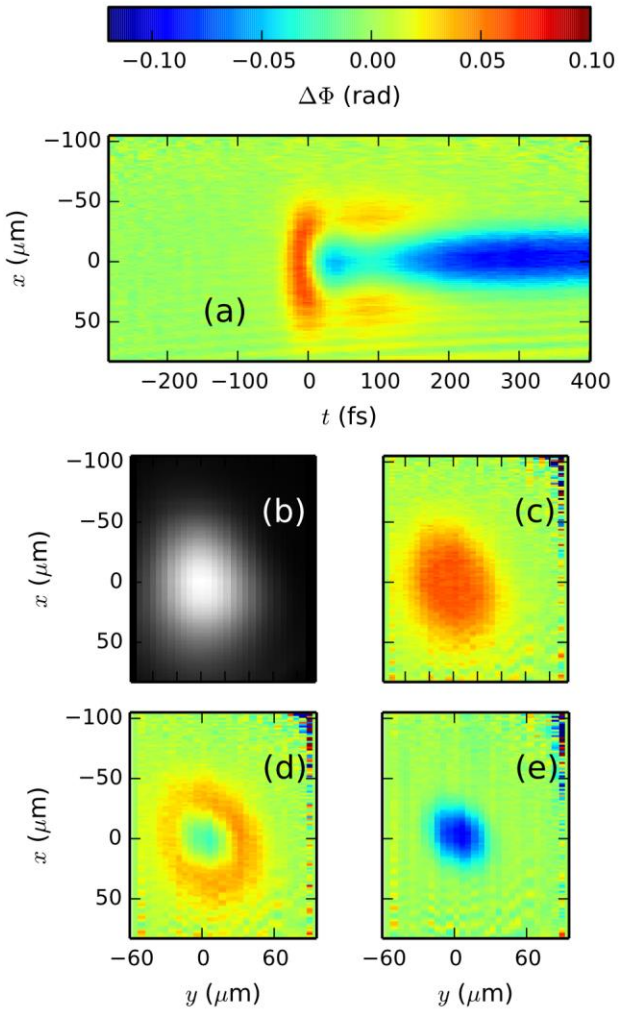

Figure 5.5. Results in N_2 at a pump peak intensity of 115 TW/cm^2. **(a)** Measured spatiotemporal phase shift $\Delta\Phi(x,y_0,t)$. **(b)** An image of the pump spot at the gas target, showing that the Kerr response simply follows the pump intensity profile. **(c)** The phase shift $\Delta\Phi(x,y,t_0 - 14$ fs), showing mostly the Kerr response. **(d)** The phase shift $\Delta\Phi(x,y,t_0+14$ fs), showing the Kerr response on the wings and the growing plasma phase shift in the center of the beam. **(e)** The phase shift $\Delta\Phi(x,y,t_0+280$ fs), showing the negative plasma phase shift long after the pump pulse and rotational response.

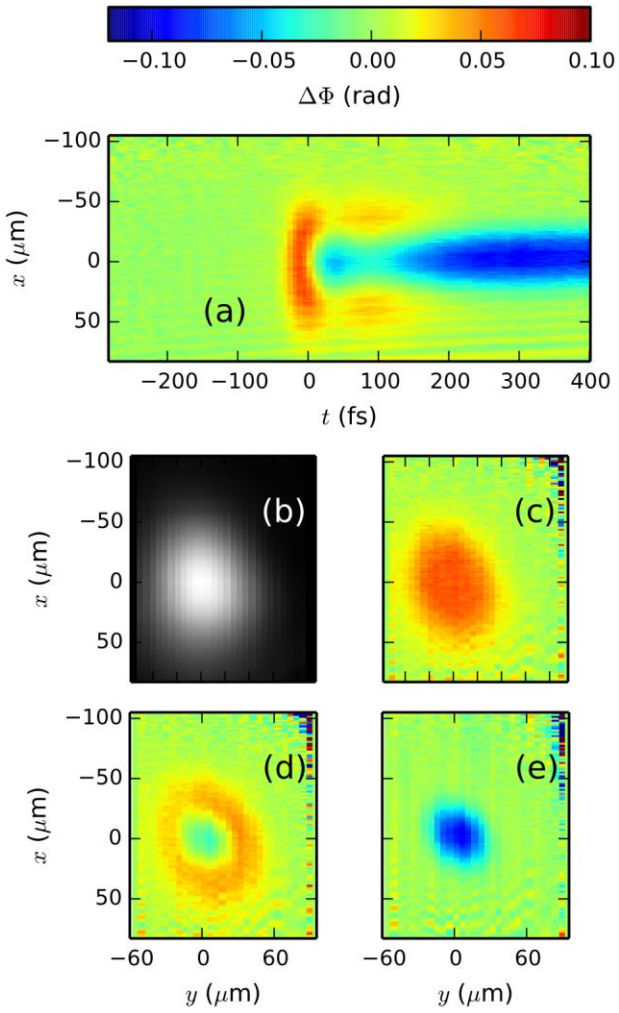

Figure 5.6. Results in O_2 at a pump peak intensity of 89 TW/cm^2. (a) Measured spatiotemporal phase shift $\Delta\Phi(x,y_0,t)$. (b) An image of the pump spot at the gas target, showing that the Kerr response simply follows the pump intensity profile. (c) The phase shift $\Delta\Phi(x,y,t_0 - 14$ fs), showing mostly the Kerr response. (d) The phase shift $\Delta\Phi(x,y,t_0+14$ fs), showing the Kerr response on the wings and the growing plasma phase shift in the center of the beam. (e) The phase shift $\Delta\Phi(x,y,t_0+350$ fs), showing the negative plasma phase shift long after the pump pulse and rotational response

Recording the full 2D+1 phase shift and amplitude change of the probe beam has multiple advantages. Among them is that the spatial peak of the pump spot is easily located, even in the presence of pointing drift, and that a single 2D phase shift profile contains many intensity points. Additionally, the 2D+1 data provides sufficient

information to computationally propagate the imaging plane, allowing post-experiment correction for slight misalignments of the imaging system, which can distort the measured phase and even convert probe beam phase shifts into amplitude changes and vice versa.

We first examine the pure plasma component of the phase shift, which can be isolated by examining time delays long after the bound electron response, which can include the prompt Kerr response and the delayed rotational response [29] (in the case of N_2 and O_2). For our case of a thin gas target in which the probe experiences negligible refraction, the refractive index profile is found using $\Delta n(x,y,t) = \Delta\Phi(x,y,t)/(kL_{eff})$, giving $N_e(x,y)$=-$2N_{cr}\Delta n(x,y,t_1)$ for the electron density profile, where t_1 > 50 fs for the noble gases and t_1 > 250 fs for N_2 and O_2. Here we have used the refractive index shift induced by a low density collisionless plasma, $\Delta n = -N_e / 2N_{cr}$, where $N_{cr} = 3.1\times10^{21}\,\mathrm{cm}^{-3}$ is the critical electron density at the probe central wavelength λ_{pr} = 600 nm. In the absence of probe refraction, each probe ray centered at (x_i,y_i) samples the dynamics induced by the intensity profile $I(x_i,y_i,t)$. The ionization yield $Y = N_e/N_0$ as a function of intensity is shown in Fig. 5.7, where N_0 is the peak gas density in the target. Each plotted point is determined as follows: For each data set (a complete 2D+1 scan of ~10^4 consecutive shots at the same nominal peak laser power), we sorted the ionization yield data points (for times $t > t_1$) into 20 intensity bins. The points in Fig. 5.7 are average values for Y in each bin. A full intensity scan for a gas species consists of multiple 2D+1 datasets, each at a different nominal peak laser power. A total of 12 data sets were used for Ar, 4 for Kr, 6 for Xe,

9 for N_2, and 8 for O_2 to generate Fig. 5.7. Results are compared to the ionization yield calculated using the highly cited Peremolov-Popov-Terent'ev (PPT)

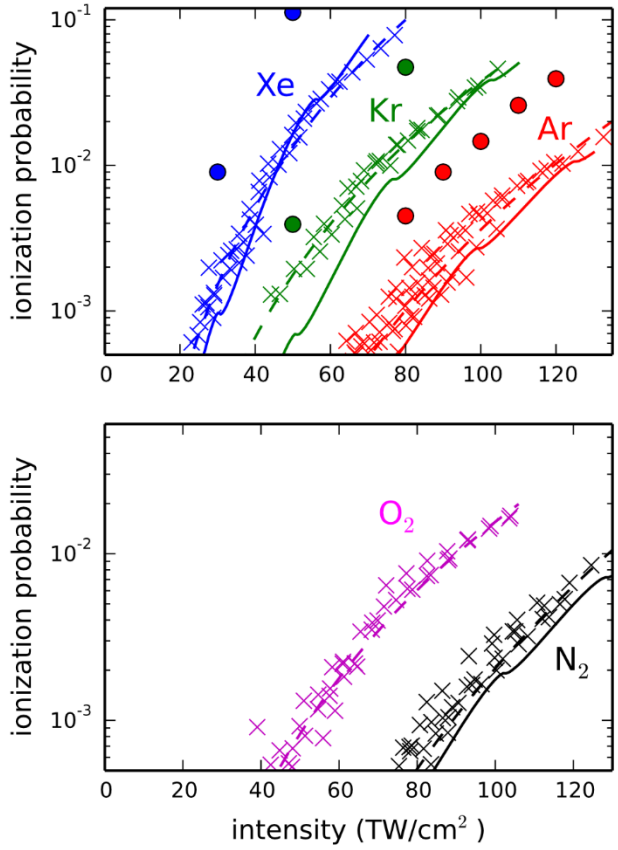

Figure 5.7. Ionization yield (x) as a function of peak intensity for **(a)** Ar (red), Kr (green), Xe (blue); **(b)** N2 (black) and O2 (magenta). PPT [130] rates are shown as solid lines. TDSE calculations for Ar, Kr, and Xe are shown as closed circles [131]. Fits to a multiphoton ionization rate are shown as dashed lines.

rate [126,130] (solid lines) and to single active electron time-dependent Schrodinger equation (TDSE) calculations (closed circles) [131].

As in most measurements of the nonlinear response, the error is dominated by the uncertainty in the peak intensity. Here, in a new procedure, we use our previous measurement [22,108] of the nonlinear refractive index of Ar, $n_2 = (9.7\pm1.2)\times10^{-20}$ cm^2/W, to provide full 2D calibration of our intensity profiles through

$\Delta n(x,y) = n_2 I(x,y)$ by directly comparing CCD camera images of the pump spot to 2D Kerr phase shift profiles measured with 2D+1 SSSI at sub-ionization intensities of <50 TW/cm^2. The uncertainty in the intensity is 13%, mostly arising from the uncertainty in n_2, with the residual uncertainty due to shot-to-shot fluctuations in the measured phase shift of ~3 mrad. The actual uncertainty, as is clear from the scatter in Fig. 5.3, is greater and increases with ionization yield. It is dominated by systematic errors that are difficult to quantify. For example, probe refraction can distort the phase image, increasing the scatter in the measured phase shift at points that correspond to the same peak intensity.

As discussed earlier, the atoms/molecules in gases supporting filamentary propagation of femtosecond pulses are exposed to highly non-perturbative fields, leading to questions [72,132,133] about whether all the possible physics of the atomic/molecular response important to propagation had been captured by well-known models [2], and suggesting potential exotic effects [134]. While our prior experiments accurately accounted for the bound electron nonlinearity *below* the ionization threshold [108], only with this experiment have we fully mapped the complete nonlinear response through the ionization transition with sufficient accuracy to map the bound contribution surviving *above* the ionization threshold.

The full time-dependent nonlinear response, from the onset of the Kerr response through ionization for argon, is shown in Fig. 5.8. At low intensity the response follows the pump pulse intensity envelope, which is well fit by a Gaussian with a full width at half maximum (FWHM) of τ_{FWHM} =42 fs, as shown in Fig. 5.8(a). Time traces of the time-dependent refractive index shift are shown in Fig. 5.8(b) at various

intensities, along with fits to $\Delta n(t) = \Delta n_K e^{-t^2/\tau^2} + \Delta n_p \,\mathrm{erf}[t/(\tau/m^{1/2})]$, where $\tau = \tau_{FWHM}/(2\sqrt{\ln 2})$. The first term, with $\Delta n_K = n_2 I_0$, is the Kerr response for a Gaussian pulse of peak intensity I_0, and the second term models the plasma contribution supplied by a multiphoton ionization rate $Y=CI^m$ for a Gaussian pulse, where C and m are fitting parameters. Despite its simplicity, this model is an excellent fit to the data. Figure 5.8(c) plots, as a function of peak intensity, the peak Kerr contribution Δn_K and the peak index change Δn_p contributed by the plasma component.

Remarkably, we find that Δn_K continues to rise with intensity even *beyond the ionization threshold*. In Ar, Kr, and Xe, the intensity dependence of Δn_K is consistent with $\Delta n_K = n_2 I$, where n_2 describes the linear dependence of Δn_K at intensities in the perturbation regime, well below the appearance of ionization [108]. Results are similar in O_2 and N_2, shown in Fig. 5.4(d). That such a simple response of bound electrons, normally associated with low order perturbation theory, continues to apply for non-perturbative fields *beyond* the ionization threshold, is itself a more intriguing effect than any of the previously suggested exotica [129,134].

The dynamic range of the measurement is limited by two factors. Given the number of shots averaged here, the minimum measurable phase shift is ~5 mrad. To minimize refractive distortion of the probe beam, the phase shift should ideally be kept well below 1 radian. Thus, one could extend the measurement to higher intensities by lowering the gas density (input pressure), as long as the linear phase shift through the target is still large enough (~0.1 rad) to be accurately measured.

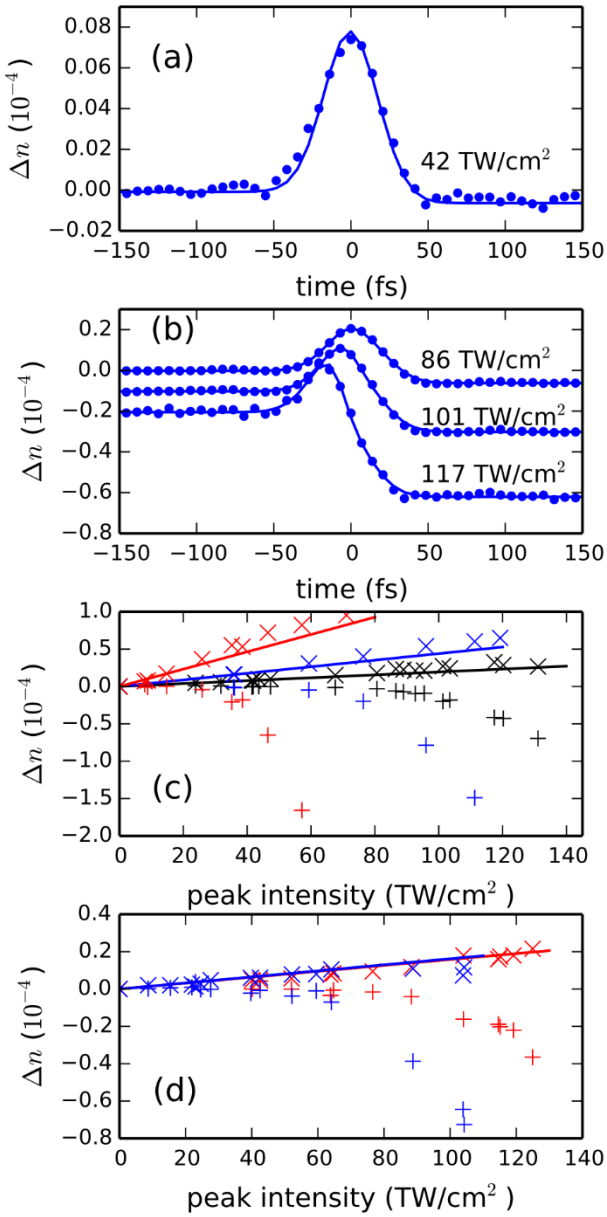

Figure 5.8. Response during pump pulse. **(a)** The nonlinear refractive index as a function of time for peak intensity of 42 TW/cm2, below the threshold for ionization, and a fit to a Gaussian with FWHM 42 fs. **(b)** Nonlinear refractive index as a function of time and fits to the standard model (Kerr effect plus ionization) for Ar. The curves have been offset vertically for clarity. **(c)** Plot of Kerr index change (×) and plasma index change (+) from fits as a function of intensity in Ar (black), Kr (blue), and Xe (red). **(d)** Same as part **(c)** for N_2 (red) and O_2 (blue).

In summary, we have performed absolute measurements of transient laser-induced ionization rates in Ar, Kr, Xe, N_2, and O_2, enabling quantitative comparison

with theory. Unlike the usual methods [9-12] for measuring ionization, which involve electrostatic collection of a few ions distributed through the laser focus, single shot spectral interferometry is applicable to high pressure gases, which allows absolute measurements associated with accurate beam intensity calibration. Importantly, knowledge of absolute ionization rates allows one, finally, to establish the absolute levels of free and bound electron contribution to the medium polarizability in common propagation scenarios involving ionization, such as femtosecond filamentation. At least for a ~40 fs Gaussian-like pump pulse at λ = 800 nm, the bound component of the electron response is universally quadratic in the field over the full range of the interaction up to >100 TW/cm^2, which is well past the ionization threshold of the gases measured here, and manifestly in the non-perturbative regime.

Appendix A: Classical work done on a rigid rotor by single impulse

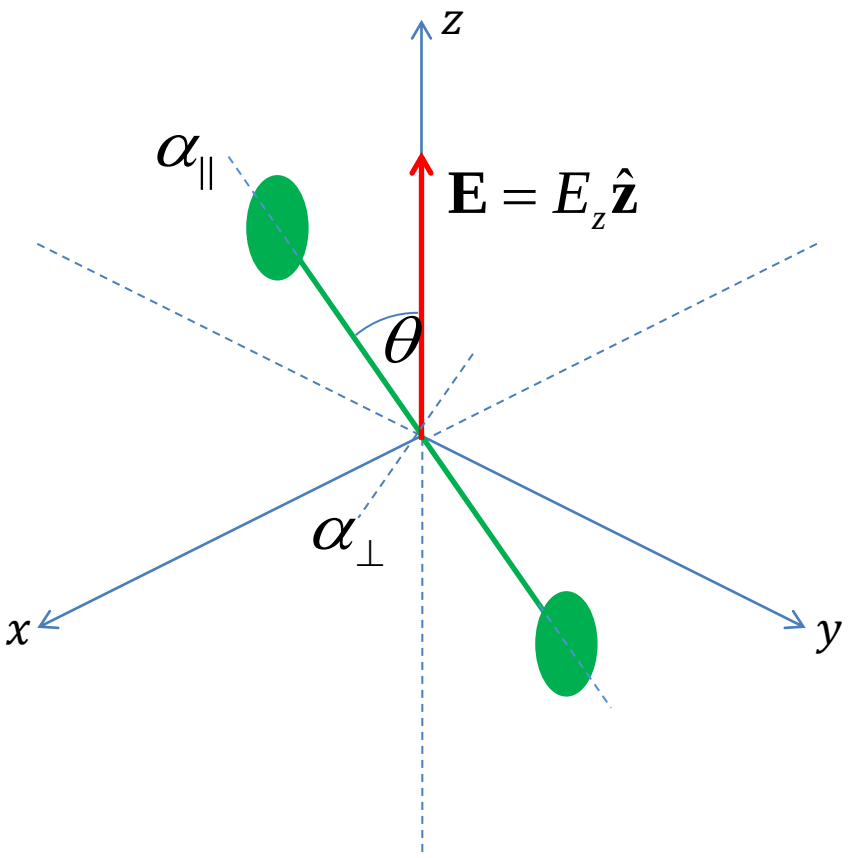

Figure A.1 Diatomic molecule in an external pump electric field

In the diatomic molecules frame of reference the linear polarizability tensor is

$$\alpha = \begin{pmatrix} \alpha_{\perp} & & \\ & \alpha_{\perp} & \\ & & \alpha_{\parallel} \end{pmatrix}, \tag{A.1}$$

where $\alpha_{\parallel}$ and $\alpha_{\perp}$ are the polarizabilities along the long and short axes of the molecule. We define the rotation matrix around *y*-axis as

$$\mathbf{R}_y(\theta) = \begin{pmatrix} \cos\theta & 0 & \sin\theta \\ 0 & 1 & 0 \\ -\sin\theta & 0 & \cos\theta \end{pmatrix}, \tag{A.2}$$

thus in lab frame of reference we have

$$\alpha(\theta) = \mathbf{R}_y^T \alpha \mathbf{R}_y = \begin{pmatrix} \alpha_{\parallel} - \Delta\alpha\cos^2\theta & 0 & \Delta\alpha\sin\theta\cos\theta \\ 0 & \alpha_{\perp} & 0 \\ \Delta\alpha\sin\theta\cos\theta & 0 & \alpha_{\parallel} - \Delta\alpha\sin^2\theta \end{pmatrix} \tag{A.3}$$

where $\Delta\alpha = \alpha_{\parallel} - \alpha_{\perp}$. The induced dipole on the molecule due to the laser electric field is $\mathbf{p} = \alpha(\theta)\mathbf{E} = \tfrac{1}{2}\Delta\alpha\sin 2\theta E_z\hat{\mathbf{x}} + (\alpha_{\parallel} - \Delta\alpha\sin^2\theta)E_z\hat{\mathbf{z}}$, which in turn causes the molecule to experience a torque $\tau = \mathbf{p}\times\mathbf{E} = \tfrac{1}{2}\Delta\alpha E_z^2\sin 2\theta\hat{\mathbf{y}}$. For a impulsive short pulse with fluence $F(\text{erg/cm}^2)$ we have $I(t) = F\delta(t) = c/4\pi\left|E_z\right|^2$, thus

$$\boldsymbol{\tau}(t) = \frac{2\pi}{c}\Delta\alpha F\sin 2\theta\delta(t)\hat{\mathbf{y}} \tag{A.4}$$

Newton's third law related the torque to the moment of inertia I_M and angular acceleration $\ddot{\boldsymbol{\theta}}$: $\boldsymbol{\tau} = I_M\ddot{\boldsymbol{\theta}}$. Integrating this we find angular velocity

$$\begin{aligned} \boldsymbol{\omega}(t) &= \frac{1}{I_M}\int_{-\infty}^{t}\tau(t')dt' + \omega_0 \\ &= \frac{2\pi\Delta\alpha F}{cI_M}\sin 2\theta_0\,\mathrm{H}(t)\hat{\mathbf{y}} + \boldsymbol{\omega}_0 \end{aligned} \tag{A.5}$$

where $\mathrm{H}(t)$ is the unit step function, $\boldsymbol{\omega}_0$ is the initial angular velocity and θ_0 is the initial angle. We have that the angle θ doesn't change significantly during the optical pulse, which is true for an ultrashort pulse. The work done on the molecule is

$$\begin{aligned} W &= \int\tau(t)\cdot\omega(t)dt \\ &= \frac{2\pi^2F^2(\Delta\alpha)^2}{c^2I_M}\sin^2 2\theta_0 + \frac{2\pi}{c}\Delta\alpha F\sin 2\theta_0\hat{\mathbf{y}}\cdot\boldsymbol{\omega}_0 \end{aligned} \tag{A.6}$$

Assuming all of the initial angles and initial angular velocity directions are equally likely the second term averages to zero and

$$\bar{W} = \frac{1}{2\pi}\int_0^{2\pi} d\varphi \int_0^{\frac{\pi}{2}} \frac{2\pi^2 F^2 (\Delta\alpha)^2}{c^2 I_M} \sin^2 2\theta_0 \sin\theta_0 d\theta_0 \qquad (A.7)$$

$$= \frac{16\pi^2 F^2 (\Delta\alpha)^2}{15 c^2 I_M}$$

Appendix B: Electronic and rotational symmetries in isotropic media

For an isotropic media third order electronic nonlinearity $\chi^{(3)}$ possesses the following symmetries [26]:

$$\chi^{(3)}_{yyzz} = \chi^{(3)}_{zzyy} = \chi^{(3)}_{zzxx} = \chi^{(3)}_{xxzz} = \chi^{(3)}_{xxyy} = \chi^{(3)}_{yyxx}, \tag{B.1a}$$

$$\chi^{(3)}_{yzyz} = \chi^{(3)}_{zyzy} = \chi^{(3)}_{zxzx} = \chi^{(3)}_{xzxz} = \chi^{(3)}_{xyxy} = \chi^{(3)}_{yxyx}, \tag{B.1b}$$

$$\chi^{(3)}_{yzzy} = \chi^{(3)}_{zyyz} = \chi^{(3)}_{zxxz} = \chi^{(3)}_{xzzx} = \chi^{(3)}_{xyyx} = \chi^{(3)}_{yxxy}, \tag{B.1c}$$

$$\chi^{(3)}_{xxxx} = \chi^{(3)}_{yyyy} = \chi^{(3)}_{zzzz} = \chi^{(3)}_{xxzz} + \chi^{(3)}_{xzxz} + \chi^{(3)}_{xzzx}. \tag{B.1d}$$

Assuming Kleinman symmetry, eq. (B.1d) results in

$$\frac{1}{3}\chi^{(3)}_{xxxx} = \frac{1}{3}\chi^{(3)}_{yyyy} = \frac{1}{3}\chi^{(3)}_{zzzz} = \chi^{(3)}_{xxzz} = \chi^{(3)}_{xzxz} = \chi^{(3)}_{xzzx}. \tag{B.2}$$

Let us assume initially that the pump and probe are both polarized along the *z* axis. We have

$$P_z(\omega_p) = \chi^{(3)}_{zzzz}(-\omega_p;\omega_e,-\omega_e,\omega_p)E_e^{(z)}E_e^{(z)*}E_p^{(z)}, \tag{B.3}$$

whereas for the case that the probe is polarized along *x* we have

$$\begin{aligned} P_x(\omega_p) &= \chi^{(3)}_{xzzx}(-\omega_p;\omega_e,-\omega_e,\omega_p)E_e^{(z)}E_e^{(z)*}E_p^{(x)} \\ &= \frac{1}{3}\chi^{(3)}_{zzzz}(-\omega_p;\omega_e,-\omega_e,\omega_p)E_e^{(z)}E_e^{(z)*}E_p^{(x)} \end{aligned} \tag{B.4}$$

Thus the phase shift imparted on the probe due to electronic response in isotropic media when it is perpendicular to the pump is 1/3 of the electronic phase shift of the probe when they are copolarized.

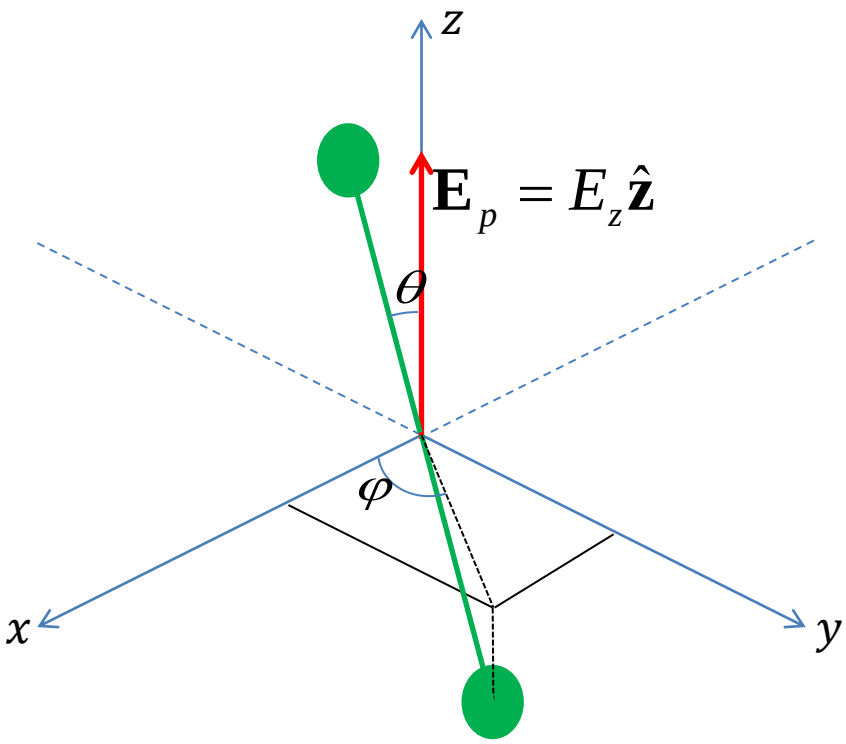

Figure B.1 Diatomic molecule in an external probe electric field

Next we derive the induced phase shift due to rotational response when the probe is parallel to pump (along z) , as shown in Fig. B.1. As derived in Eq.(A.3) the induced dipole moment along z is $p_z = (\alpha_\perp + \Delta\alpha\cos^2\theta)E_z$. When we have a population of molecules that are at thermal equilibrium every orientation along upper half sphere is equally probable and thus in average

$$\left\langle \cos^2\theta \right\rangle = \int_0^{2\pi} d\varphi \int_0^{\frac{\pi}{2}} d\theta \cos^2\theta \frac{1}{2\pi}\sin\theta = \frac{1}{3} \tag{B.5}$$

and $\langle p_z \rangle = (\alpha_\perp + 1/3\Delta\alpha)E_z$ So for a probe along the z- axis the refractive index is $n_0^2 = 1 + 4\pi N(\alpha_\perp + \frac{1}{3}\Delta\alpha)$. A strong pump along z-axis, rotational wave packet is formed, then the refractive index is $n_\parallel^2 = 1 + 4\pi N\left(\alpha_\perp + \Delta\alpha\left\langle \cos^2\theta \right\rangle_t\right)$. Thus the

change in refractive index due to the rotational wave packet is

$n_{\parallel}^2 - n_0^2 = 4\pi N \Delta\alpha \left(\left\langle \cos^2\theta \right\rangle_t - 1/3 \right)$ which can be simplified as

$$\Delta n_{\parallel}(t) \approx \frac{2\pi N \Delta\alpha}{n_0} \left(\left\langle \cos^2\theta \right\rangle_t - 1/3 \right).$$

When the probe is aligned along *x* we define the new rotation matrix

$$\mathbf{R} = \mathbf{R}_y(\theta)\mathbf{R}_z(\varphi) = \begin{pmatrix} \cos\theta\cos\varphi & \cos\theta\sin\varphi & \sin\theta \\ -\sin\varphi & \cos\varphi & 0 \\ -\sin\theta\cos\varphi & -\sin\theta\sin\varphi & \cos\theta \end{pmatrix}, \tag{B.6}$$

thus have

$$\alpha(\theta,\varphi) = \mathbf{R}^T \alpha \mathbf{R} \tag{B.7}$$

After tedious calculations, it can be shown that $n^2 = 1 + 4\pi N \left(\alpha_{\perp} + \frac{1}{2}\Delta\alpha \left\langle \sin^2\theta \right\rangle_t \right)$

and using the relation

$$\left\langle \sin^2\theta \right\rangle = \int_0^{2\pi} d\varphi \int_0^{\frac{\pi}{2}} d\theta \sin^2\theta \frac{1}{2\pi} \sin\theta = \frac{2}{3} \tag{B.8}$$

for an ensemble of molecules with thermal distribution.. Thus for the case of probe perpendicular to pump we have $n_{\perp}^2 - n_0^2 = 4\pi N \Delta\alpha \left(\frac{1}{2} \left\langle \sin^2\theta \right\rangle_t - \frac{1}{3} \right)$ or

$\Delta n_{\perp}(t) \approx \frac{2\pi N \Delta\alpha}{n_0} \left(\frac{1}{2} \left\langle \sin^2\theta \right\rangle_t - 1/3 \right)$. We note that $\left\langle \sin^2\theta \right\rangle_t = 1 - \left\langle \cos^2\theta \right\rangle_t$ which

results in $\Delta n_{\perp}(t) = -\frac{1}{2}\Delta n_{\parallel}(t)$

Bibliography

1. M. Lewenstein, P. Balcou, M. Y. Ivanov, A. L'Huillier, and P. B. Corkum, "Theory of high-harmonic generation by low-frequency laser fields," Phys. Rev. A **49**, 2117–2132 (1994).

2. A. Couairon and A. Mysyrowicz, "Femtosecond filamentation in transparent media," Phys. Rep. **441**, 47–189 (2007).

3. L. Bergé, S. Skupin, R. Nuter, J. Kasparian, and J.-P. Wolf, "Ultrashort filaments of light in weakly ionized, optically transparent media," Reports Prog. Phys. **71**, 109801 (2008).

4. K. Y. Kim, A. J. Taylor, J. H. Glownia, and G. Rodriguez, "Coherent control of terahertz supercontinuum generation in ultrafast laser–gas interactions," Nat. Photonics **2**, 605–609 (2008).

5. T. Vockerodt, D. S. Steingrube, E. Schulz, M. Kretschmar, U. Morgner, and M. Kovačev, "Low- and high-order harmonic generation inside an air filament," Appl. Phys. B **106**, 529–532 (2012).

6. Y. Liu, Y. Brelet, G. Point, A. Houard, and A. Mysyrowicz, "Self-seeded lasing in ionized air pumped by 800 nm femtosecond laser pulses," Opt. Express **21**, 22791 (2013).

7. D. Kartashov, S. Ališauskas, A. Baltuška, A. Schmitt-Sody, W. Roach, and P. Polynkin, "Remotely pumped stimulated emission at 337 nm in atmospheric nitrogen," Phys. Rev. A **88**, 41805 (2013).

8. A. Dogariu, J. B. Michael, M. O. Scully, and R. B. Miles, "High-Gain Backward Lasing in Air," Science (80-.). **331**, (2011).

9. R. R. Alfano and S. L. Shapiro, "Emission in the Region 4000 to 7000 Å Via Four-Photon Coupling in Glass," Phys. Rev. Lett. **24**, 584–587 (1970).

10. E. W. Rosenthal, N. Jhajj, I. Larkin, S. Zahedpour, J. K. Wahlstrand, and H. M. Milchberg, "Energy deposition of single femtosecond filaments in the atmosphere," Opt. Lett. **41**, 3908 (2016).

11. Y.-H. Y.-H. Cheng, J. K. Wahlstrand, N. Jhajj, and H. M. Milchberg, "The effect of long timescale gas dynamics on femtosecond filamentation.," Opt. Express **21**, 4740–51 (2013).

12. N. Jhajj, Y. H. H. Cheng, J. K. Wahlstrand, and H. M. Milchberg, "Optical beam dynamics in a gas repetitively heated by femtosecond filaments," Opt. Express **21**, 28980–28986 (2013).

13. E. W. Rosenthal, N. Jhajj, J. K. Wahlstrand, and H. M. Milchberg, "Collection of remote optical signals by air waveguides," Optica **1**, 5–9 (2014).

14. J. K. Wahlstrand, N. Jhajj, E. W. Rosenthal, S. Zahedpour, and H. M. Milchberg, "Direct imaging of the acoustic waves generated by femtosecond filaments in air," Opt. Lett. **39**, 1290 (2014).

15. N. Jhajj, J. K. Wahlstrand, and H. M. Milchberg, "Optical mode structure of the air waveguide.," Opt. Lett. **39**, 6312–5 (2014).

16. O. Lahav, L. Levi, I. Orr, R. A. Nemirovsky, J. Nemirovsky, I. Kaminer, M. Segev, and O. Cohen, "Long-lived waveguides and sound-wave generation by laser filamentation," Phys. Rev. A - At. Mol. Opt. Phys. **90**, (2014).

17. N. Jhajj, Y.-H. Cheng, J. K. Wahlstrand, and H. M. Milchberg, "Optical beam dynamics in a gas repetitively heated by femtosecond filaments," Opt. Express **21**, 28980 (2013).

18. P. Panagiotopoulos, P. Whalen, M. Kolesik, and J. V. Moloney, "Super high power mid-infrared femtosecond light bullet," Nat. Photonics **9**, 543–548 (2015).

19. T. Popmintchev, M.-C. Chen, D. Popmintchev, P. Arpin, S. Brown, S. Ališauskas, G. Andriukaitis, T. Balčiunas, O. D. Mücke, A. Pugzlys, A. Baltuška, B. Shim, S. E. Schrauth, A. Gaeta, C. Hernández-García, L. Plaja, A. Becker, A. Jaron-Becker, M. M. Murnane, and H. C. Kapteyn, "Bright Coherent Ultrahigh Harmonics in the keV X-ray Regime from Mid-Infrared Femtosecond Lasers," Science (80-.). **336**, (2012).

20. D. Kartashov, S. Ališauskas, A. Pugžlys, A. Voronin, A. Zheltikov, M. Petrarca, P. Béjot, J. Kasparian, J.-P. Wolf, and A. Baltuška, "Mid-infrared laser filamentation in molecular gases," Opt. Lett. **38**, 3194 (2013).

21. P. N. Butcher and D. (David) Cotter, *The Elements of Nonlinear Optics* (Cambridge University Press, 1990).

22. J. K. Wahlstrand, Y.-H. Cheng, and H. M. Milchberg, "Absolute measurement of the transient optical nonlinearity in N 2 , O 2 , N 2 O, and Ar," Phys. Rev. A **85**, 43820 (2012).

23. J. P. Palastro, J. Peñano, L. A. Johnson, B. Hafizi, J. K. Wahlstrand, and H. M. Milchberg, "Two-photon vibrational excitation of air by long-wave infrared laser pulses," Phys. Rev. A **94**, 23816 (2016).

24. D. T. Reid, P. Loza-Alvarez, C. T. A. Brown, T. Beddard, and W. Sibbett, "Amplitude and phase measurement of mid-infrared femtosecond pulses by

using cross-correlation frequency-resolved optical gating," Opt. Lett. **25**, 1478 (2000).

25. R. Y. Chiao, E. Garmire, and C. H. Townes, "Self-Trapping of Optical Beams," Phys. Rev. Lett. **13**, 479–482 (1964).

26. R. W. Boyd, *Nonlinear Optics* (Academic Press, 2008).

27. D. Strickland and G. Mourou, "Compression of amplified chirped optical pulses," Opt. Commun. **55**, 447–449 (1985).

28. K. Y. Kim, I. Alexeev, and H. M. Milchberg, "Single-shot supercontinuum spectral interferometry," Appl. Phys. Lett. **81**, 4124–4126 (2002).

29. Y.-H. Chen, S. Varma, A. G. York, and H. M. Milchberg, "Single-shot, space- and time-resolved measurement of rotational wavepacket revivals in H_2, D_2, N_2, O_2, and N_2O," Opt. Express **15**, 11341 (2007).

30. J. K. Wahlstrand, S. Zahedpour, and H. M. Milchberg, "Optimizing the time resolution of supercontinuum spectral interferometry," J. Opt. Soc. Am. B **33**, 1476 (2016).

31. M. Sheik-Bahae, A. A. Said, T.-H. Wei, D. J. Hagan, and E. W. Van Stryland, "Sensitive measurement of optical nonlinearities using a single beam," IEEE J. Quantum Electron. **26**, 760–769 (1990).

32. M. Takeda, H. Ina, and S. Kobayashi, "Fourier-transform method of fringe-pattern analysis for computer-based topography and interferometry," J. Opt. Soc. Am. **72**, 156 (1982).

33. J. Yu, D. Mondelain, J. Kasparian, E. Salmon, S. Geffroy, C. Favre, V. Boutou, and J.-P. Wolf, "Sonographic probing of laser filaments in air.," Appl. Opt. **42**, 7117–20 (2003).

34. F. Vidal, D. Comtois, Ching-Yuan Chien, A. Desparois, B. La Fontaine, T. W. T. W. Johnston, J. C. J.-C. Kieffer, H. P. H. P. Mercure, H. Pepin, and F. A. F. A. Rizk, "Modeling the triggering of streamers in air by ultrashort laser pulses," IEEE Trans. Plasma Sci. **28**, 418–433 (2000).

35. S. Tzortzakis, B. Prade, M. Franco, a. Mysyrowicz, S. Hüller, and P. Mora, "Femtosecond laser-guided electric discharge in air," Phys. Rev. E **64**, 57401 (2001).

36. Y.-H. Cheng, J. K. Wahlstrand, N. Jhajj, and H. M. Milchberg, "The effect of long timescale gas dynamics on femtosecond filamentation," Opt. Express **21**, 4740 (2013).

37. N. Jhajj, E. W. Rosenthal, R. Birnbaum, J. K. Wahlstrand, and H. M. Milchberg, "Demonstration of Long-Lived High-Power Optical Waveguides in Air," Phys. Rev. X **4**, 11027 (2014).

38. D. V. Kartashov, A. V. Kirsanov, A. M. Kiselev, A. N. Stepanov, N. N. Bochkarev, Y. N. Ponomarev, and B. A. Tikhomirov, "Nonlinear absorption of intense femtosecond laser radiation in air," Opt. Express **14**, 7552 (2006).

39. A. M. Kiselev, Y. N. Ponomarev, A. N. Stepanov, A. B. Tikhomirov, and B. A. Tikhomirov, "Nonlinear absorption of femtosecond laser pulses (800 nm) by atmospheric air and water vapour," Quantum Electron. **41**, 976–979 (2011).

40. T. B. Petrova, H. D. Ladouceur, and A. P. Baronavski, "Nonequilibrium dynamics of laser-generated plasma channels," Phys. Plasmas **15**, 53501 (2008).

41. A. G. York and H. M. Milchberg, "Broadband terahertz lasing in aligned molecules.," Opt. Express **16**, 10557–105645 (2008).

42. J. P. Cryan, P. H. Bucksbaum, and R. N. Coffee, "Field-free alignment in repetitively kicked nitrogen gas," Phys. Rev. A **80**, 63412 (2009).

43. S. Varma, Y.-H. Chen, J. P. Palastro, A. B. Fallahkair, E. W. Rosenthal, T. Antonsen, and H. M. Milchberg, "Molecular quantum wake-induced pulse shaping and extension of femtosecond air filaments," Phys. Rev. A **86**, 23850 (2012).

44. J. P. Palastro, T. M. Antonsen, and H. M. Milchberg, "Compression, spectral broadening, and collimation in multiple, femtosecond pulse filamentation in atmosphere," Phys. Rev. A **86**, 33834 (2012).

45. S. Zhdanovich, C. Bloomquist, J. Floß, I. S. Averbukh, J. W. Hepburn, and V. Milner, "Quantum Resonances in Selective Rotational Excitation of Molecules with a Sequence of Ultrashort Laser Pulses," Phys. Rev. Lett. **109**, 43003 (2012).

46. D. M. Villeneuve, S. A. Aseyev, P. Dietrich, M. Spanner, M. Y. Ivanov, and P. B. Corkum, "Forced molecular rotation in an optical centrifuge.," Phys. Rev. Lett. **85**, 542–5 (2000).

47. L. Yuan, C. Toro, M. Bell, and A. S. Mullin, "Spectroscopy of molecules in very high rotational states using an optical centrifuge," Faraday Discuss. **150**, 101 (2011).

48. S. Zhdanovich, A. A. Milner, C. Bloomquist, J. Floß, I. S. Averbukh, J. W. Hepburn, and V. Milner, "Control of Molecular Rotation with a Chiral Train of

Ultrashort Pulses," Phys. Rev. Lett. **107**, 243004 (2011).

49. U. Steinitz, Y. Prior, and I. S. Averbukh, "Laser-Induced Gas Vortices," Phys. Rev. Lett. **109**, 33001 (2012).

50. H. Stapelfeldt and T. Seideman, "Colloquium: Aligning molecules with strong laser pulses," Rev. Mod. Phys. **75**, 543–557 (2003).

51. C. H. Lin, J. P. Heritage, T. K. Gustafson, R. Y. Chiao, and J. P. McTague, "Birefringence arising from the reorientation of the polarizability anisotropy of molecules in collisionless gases," Phys. Rev. A **13**, 813–829 (1976).

52. D. R. Miller and R. P. Andres, "Rotational Relaxation of Molecular Nitrogen," J. Chem. Phys. **46**, 3418 (1967).

53. C. W. Siders, J. L. Siders, A. J. Taylor, S. G. Park, and A. M. Weiner, "Efficient High-Energy Pulse-Train Generation Using a 2 n-Pulse Michelson Interferometer.," Appl. Opt. **37**, 5302–5 (1998).

54. Y.-H. Y.-H. Chen, S. Varma, I. Alexeev, and H. Milchberg, "Measurement of transient nonlinear refractive index in gases using xenon supercontinuum single-shot spectral interferometry.," Opt. Express **15**, 7458–67 (2007).

55. K. P. Birch, "Precise determination of refractometric parameters for atmospheric gases," J. Opt. Soc. Am. A **8**, 647 (1991).

56. S. Ramakrishna and T. Seideman, "Intense Laser Alignment in Dissipative Media as a Route to Solvent Dynamics," Phys. Rev. Lett. **95**, 113001 (2005).

57. Y.-H. Chen, S. Varma, A. York, and H. M. Milchberg, "Single-shot, space- and time-resolved measurement of rotational wavepacket revivals in H_2, D_2, N_2, O_2, and N_2O," Opt. Express **15**, 11341 (2007).

58. K. P. Huber and G. Herzberg, *Molecular Spectra And Molecular Structure, IV. Constants Of Diatomic Molecules* (Van Nostrand Reinhold, 1979).

59. Y.-H. Chen, S. Varma, T. M. Antonsen, and H. M. Milchberg, "Direct Measurement of the Electron Density of Extended Femtosecond Laser Pulse-Induced Filaments," Phys. Rev. Lett. **105**, 215005 (2010).

60. B. Clough, J. Liu, and X.-C. Zhang, "Laser-induced photoacoustics influenced by single-cycle terahertz radiation," Opt. Lett. **35**, 3544 (2010).

61. a a Milner, a Korobenko, and V. Milner, "Sound emission from the gas of molecular superrotors.," Opt. Express **23**, 8603–8 (2015).

62. V. Renard, M. Renard, A. Rouzée, S. Guérin, H. R. Jauslin, B. Lavorel, and O. Faucher, "Nonintrusive monitoring and quantitative analysis of strong laser-field-induced impulsive alignment," Phys. Rev. A **70**, 33420 (2004).

63. J. Floß and I. S. Averbukh, "Anderson Wall and Bloch Oscillations in Molecular Rotation," Phys. Rev. Lett. **113**, 43002 (2014).

64. S. Fishman, D. R. Grempel, and R. E. Prange, "Chaos, Quantum Recurrences, and Anderson Localization," Phys. Rev. Lett. **49**, 509–512 (1982).

65. A. Couairon, L. Berge, and I. Introduction, "Modeling the filamentation of ultra-short pulses in ionizing media," Phys. Plas. **7**, 193 (2000).

66. M. Kolesik and J. V Moloney, "Modeling and simulation techniques in extreme nonlinear optics of gaseous and condensed media," Reports Prog. Phys. **77**, 16401 (2014).

67. J. P. Palastro, T. M. Antonsen, S. Varma, Y.-H. Chen, and H. M. Milchberg, "Simulations of femtosecond atmospheric filaments enhanced by dual pulse molecular alignment," Phys. Rev. A **85**, 43843 (2012).

68. E. W. Rosenthal, J. P. Palastro, N. Jhajj, S. Zahedpour, J. K. Wahlstrand, and H. M. Milchberg, "Sensitivity of propagation and energy deposition in femtosecond filamentation to the nonlinear refractive index," J. Phys. B At. Mol. Opt. Phys. **48**, 94011 (2015).

69. D. A. Simons and A. Tokunaga, "The Mauna Kea Observatories Near-Infrared Filter Set. I. Defining Optimal 1–5 Micron Bandpasses," Publ. Astron. Soc. Pacific **114**, 169–179 (2002).

70. D. M. Bishop, "General dispersion formulas for molecular third-order nonlinear optical properties," J. Chem. Phys. **90**, 3192–3195 (1989).

71. R. L. Sutherland, D. G. McLean, and S. Kirkpatrick, *Handbook of Nonlinear Optics*. (Marcel Dekker, 2003).

72. V. Loriot, E. Hertz, O. Faucher, and B. Lavorel, "Measurement of high order Kerr refractive index of major air components," Opt. Express **17**, 13429 (2009).

73. M. Reichert, P. Zhao, J. M. Reed, T. R. Ensley, D. J. Hagan, and E. W. Van Stryland, "Beam deflection measurement of bound-electronic and rotational nonlinear refraction in molecular gases," Opt. Express **23**, 22224 (2015).

74. M. A. Spackman, "Time-dependent Hartree–Fock second-order molecular properties with a moderately sized basis set. I. The frequency dependence of

the dipole polarizability," J. Chem. Phys. **94**, 1288–1294 (1991).

75. G. R. Alms, A. K. Burnham, and W. H. Flygare, "Measurement of the dispersion in polarizability anisotropies," J. Chem. Phys. **63**, 3321–3326 (1975).

76. D. P. Shelton and J. E. Rice, "Measurements and calculations of the hyperpolarizabilities of atoms and small molecules in the gas phase," Chem. Rev. **94**, 3–29 (1994).

77. D. P. Shelton, "Nonlinear-optical susceptibilities of gases measured at 1064 and 1319 nm," Phys. Rev. A **42**, 2578–2592 (1990).

78. J. E. Rice, "Frequency-dependent hyperpolarizabilities for argon, krypton, and neon: Comparison with experiment," J. Chem. Phys. **96**, 7580–7586 (1992).

79. H. Sekino and R. J. Bartlett, "Hyperpolarizabilities of molecules with frequency dependence and electron correlation," J. Chem. Phys. **94**, 3665–3669 (1991).

80. H. Sekino and R. J. Bartlett, "Molecular hyperpolarizabilities," J. Chem. Phys. **98**, 3022–3037 (1993).

81. J. K. Wahlstrand, Y.-H. Cheng, and H. M. Milchberg, "Absolute measurement of the transient optical nonlinearity in N 2 , O 2 , N 2 O, and Ar," Phys. Rev. A **85**, 43820 (2012).

82. J. K. Wahlstrand, Y.-H. Cheng, and H. M. Milchberg, "Absolute measurement of the transient optical nonlinearity in N_2 , O_2 , N_2 O, and Ar," Phys. Rev. A **85**, 43820 (2012).

83. C.-H. Lu, Y.-J. Tsou, H.-Y. Chen, B.-H. Chen, Y.-C. Cheng, S.-D. Yang, M.-C. Chen, C.-C. Hsu, and A. H. Kung, "Generation of intense supercontinuum in condensed media," Optica **1**, 400 (2014).

84. C.-H. Lu, B.-H. Chen, Y.-C. Cheng, and A. H. Kung, "Multi-plate generation and compression of an intense supercontinuum pulse," in *High-Brightness Sources and Light-Driven Interactions* (OSA, 2016), p. HS4B.1.

85. M. Durand, A. Jarnac, A. Houard, Y. Liu, S. Grabielle, N. Forget, A. Dur?cu, A. Couairon, and A. Mysyrowicz, "Self-Guided Propagation of Ultrashort Laser Pulses in the Anomalous Dispersion Region of Transparent Solids: A New Regime of Filamentation," Phys. Rev. Lett. **110**, 115003 (2013).

86. C. R. Petersen, U. Møller, I. Kubat, B. Zhou, S. Dupont, J. Ramsay, T. Benson, S. Sujecki, N. Abdel-Moneim, Z. Tang, D. Furniss, A. Seddon, and O. Bang,

"Mid-infrared supercontinuum covering the 1.4–13.3 μm molecular fingerprint region using ultra-high NA chalcogenide step-index fibre," Nat. Photonics **8**, 830–834 (2014).

87. A. A. Lanin, A. A. Voronin, E. A. Stepanov, A. B. Fedotov, and A. M. Zheltikov, "Multioctave, 3–18 μm sub-two-cycle supercontinua from self-compressing, self-focusing soliton transients in a solid," Opt. Lett. **40**, 974 (2015).

88. S. Ghimire, A. D. DiChiara, E. Sistrunk, P. Agostini, L. F. DiMauro, and D. A. Reis, "Observation of high-order harmonic generation in a bulk crystal," Nat. Phys. **7**, 138–141 (2011).

89. C. C. Wang, "Empirical Relation between the Linear and the Third-Order Nonlinear Optical Susceptibilities," Phys. Rev. B **2**, 2045 (1970).

90. N. Boling, A. Glass, and A. Owyoung, "Empirical relationships for predicting nonlinear refractive index changes in optical solids," IEEE J. Quantum Electron. **14**, 601–608 (1978).

91. D. J. Kane and R. Trebino, "Characterization of arbitrary femtosecond pulses using frequency-resolved optical gating," IEEE J. Quantum Electron. **29**, 571–579 (1993).

92. C. Iaconis and I. A. Walmsley, "Spectral phase interferometry for direct electric-field reconstruction of ultrashort optical pulses," Opt. Lett. **23**, 792 (1998).

93. J. K. Wahlstrand, S. Zahedpour, Y.-H. Cheng, J. P. Palastro, and H. M. Milchberg, "Absolute measurement of the ultrafast nonlinear electronic and rovibrational response in H_2 and D_2," Phys. Rev. A **92**, 63828 (2015).

94. J. K. Wahlstrand, J. H. Odhner, E. T. McCole, Y.-H. Cheng, J. P. Palastro, R. J. Levis, and H. M. Milchberg, "Effect of two-beam coupling in strong-field optical pump-probe experiments," Phys. Rev. A **87**, 53801 (2013).

95. J. Hebling, "Derivation of the pulse front tilt caused by angular dispersion," Opt. Quantum Electron. **28**, 1759–1763 (1996).

96. S. Varma, Y.-H. Chen, and H. M. Milchberg, "Trapping and Destruction of Long-Range High-Intensity Optical Filaments by Molecular Quantum Wakes in Air," Phys. Rev. Lett. **101**, 205001 (2008).

97. E. T. J. Nibbering, G. Grillon, M. A. Franco, B. S. Prade, and A. Mysyrowicz, "Determination of the inertial contribution to the nonlinear refractive index of air, N_2, and O_2 by use of unfocused high-intensity femtosecond laser

pulses," J. Opt. Soc. Am. B **14**, 650 (1997).

98. J.-F. Ripoche, G. Grillon, B. Prade, M. Franco, E. Nibbering, R. Lange, and A. Mysyrowicz, "Determination of the time dependence of n2 in air," Opt. Commun. **135**, 310–314 (1997).

99. W. Liu and S. L. Chin, "Direct measurement of the critical power of femtosecond Ti:sapphire laser pulse in air," Opt. Express **13**, 5750 (2005).

100. J. R. Peñano, P. Sprangle, B. Hafizi, A. Ting, D. F. Gordon, and C. A. Kapetanakos, "Propagation of ultra-short, intense laser pulses in air," Phys. Plasmas **11**, 2865–2874 (2004).

101. J. H. Odhner, D. A. Romanov, and R. J. Levis, "Rovibrational Wave-Packet Dispersion during Femtosecond Laser Filamentation in Air," Phys. Rev. Lett. **103**, 75005 (2009).

102. J. H. Odhner, E. T. McCole, and R. J. Levis, "Filament-Driven Impulsive Raman Spectroscopy," J. Phys. Chem. A **115**, 13407–13412 (2011).

103. A. Dogariu, T. Xia, D. J. Hagan, A. A. Said, E. W. Van Stryland, and N. Bloembergen, "Purely refractive transient energy transfer by stimulated Rayleigh-wing scattering," J. Opt. Soc. Am. B **14**, 796 (1997).

104. S. Smolorz and F. Wise, "Femtosecond two-beam coupling energy transfer from Raman and electronic nonlinearities," J. Opt. Soc. Am. B **17**, 1636 (2000).

105. J. K. Wahlstrand, J. H. Odhner, E. T. McCole, Y.-H. Cheng, J. P. Palastro, R. J. Levis, and H. M. Milchberg, "Effect of two-beam coupling in strong-field optical pump-probe experiments," Phys. Rev. A **87**, 53801 (2013).

106. D. E. Laban, W. C. Wallace, R. D. Glover, R. T. Sang, and D. Kielpinski, "Self-focusing in air with phase-stabilized few-cycle light pulses," Opt. Lett. **35**, 1653 (2010).

107. J. K. Wahlstrand, Y.-H. Cheng, Y.-H. Chen, and H. M. Milchberg, "Optical Nonlinearity in Ar and N_2 near the Ionization Threshold," Phys. Rev. Lett. **107**, 103901 (2011).

108. J. K. Wahlstrand, Y.-H. Cheng, and H. M. Milchberg, "High Field Optical Nonlinearity and the Kramers-Kronig Relations," Phys. Rev. Lett. **109**, 113904 (2012).

109. K. K. Irikura, "Experimental Vibrational Zero-Point Energies: Diatomic Molecules," J. Phys. Chem. Ref. Data **36**, 389–397 (2007).

110. K. Huber, *Molecular Spectra and Molecular Structure: IV. Constants of Diatomic Molecules* (2013).

111. S. Zahedpour, J. K. Wahlstrand, and H. M. Milchberg, "Quantum Control of Molecular Gas Hydrodynamics," Phys. Rev. Lett. **112**, 143601 (2014).

112. N. J. Bridge and A. D. Buckingham, "The Polarization of Laser Light Scattered by Gases," Proc. R. Soc. London A Math. Phys. Eng. Sci. **295**, (1966).

113. D. M. Bishop and J. Pipin, "Vibrational effects for the dispersion-energy and dispersion-polarizability coefficients for interactions between H, He, and H_2," J. Chem. Phys. **98**, 522–524 (1993).

114. W. Demtröder, *Molecular Physics : Theoretical Principles and Experimental Methods* (Wiley-VCH, 2005).

115. J. K. Wahlstrand and H. M. Milchberg, "Effect of a plasma grating on pump–probe experiments near the ionization threshold in gases," Opt. Lett. **36**, 3822–3824 (2011).

116. T. Lundeen, S. Hou, and J. W. Nibler, "Nonresonant third order susceptibilities for various gases," J. Chem. Phys. **79**, 6301–6305 (1983).

117. D. M. Golden and B. Crawford, "Absolute Raman Intensities. I. Method for Molecules in the Gas Phase," J. Chem. Phys. **36**, 1654–1661 (1962).

118. G. J. Rosasco and W. S. Hurst, "Dispersion of the electronic contribution to the third-order nonlinear susceptibility of H_2," J. Opt. Soc. Am. B **3**, 1251 (1986).

119. J. W. Hahn and E. S. Lee, "Measurement of nonresonant third-order susceptibilities of various gases by the nonlinear interferometric technique," J. Opt. Soc. Am. B **12**, 1021 (1995).

120. C. Durfee, A. Rundquist, S. Backus, C. Herne, M. Murnane, and H. Kapteyn, "Phase Matching of High-Order Harmonics in Hollow Waveguides," Phys. Rev. Lett. **83**, 2187–2190 (1999).

121. T. Popmintchev, M.-C. Chen, D. Popmintchev, P. Arpin, S. Brown, S. Alisauskas, G. Andriukaitis, T. Balciunas, O. D. Mucke, A. Pugzlys, A. Baltuska, B. Shim, S. E. Schrauth, A. Gaeta, C. Hernandez-Garcia, L. Plaja, A. Becker, A. Jaron-Becker, M. M. Murnane, and H. C. Kapteyn, "Bright Coherent Ultrahigh Harmonics in the keV X-ray Regime from Mid-Infrared Femtosecond Lasers," Science (80-.). **336**, 1287–1291 (2012).

122. P. B. Corkum, C. Rolland, and T. Srinivasan-Rao, "Supercontinuum generation

in gases," Phys. Rev. Lett. **57**, 2268–2271 (1986).

123. T. Brabec and F. Krausz, "Nonlinear Optical Pulse Propagation in the Single-Cycle Regime," Phys. Rev. Lett. **78**, 3282–3285 (1997).

124. S. L. Chin, *Femtosecond Laser Filamentation*, Springer Series on Atomic, Optical, and Plasma Physics (Springer New York, 2010), Vol. 55.

125. B. Walker, B. Sheehy, L. F. Dimauro, P. Agostini, K. J. Schafer, and K. C. Kulander, "Precision measurement of strong field double ionization of helium," Phys. Rev. Lett. **73**, 1227–1230 (1994).

126. S. F. J. Larochelle, A. Talebpour, and S. L. Chin, "Coulomb effect in multiphoton ionization of rare-gas atoms," J. Phys. B At. Mol. Opt. Phys. **31**, 1215–1224 (1998).

127. A. Talebpour, J. Yang, and S. L. Chin, "Semi-empirical model for the rate of tunnel ionization of N2 and O2 molecule in an intense Ti:sapphire laser pulse," Opt. Commun. **163**, 29–32 (1999).

128. W. C. Wallace, O. Ghafur, C. Khurmi, S. Sainadh U, J. E. Calvert, D. E. Laban, M. G. Pullen, K. Bartschat, A. N. Grum-Grzhimailo, D. Wells, H. M. Quiney, X. M. Tong, I. V. Litvinyuk, R. T. Sang, and D. Kielpinski, "Precise and Accurate Measurements of Strong-Field Photoionization and a Transferable Laser Intensity Calibration Standard," Phys. Rev. Lett. **117**, 53001 (2016).

129. M. Richter, S. Patchkovskii, F. Morales, O. Smirnova, and M. Ivanov, "The role of the Kramers–Henneberger atom in the higher-order Kerr effect Adiabatic Floquet model for the optical response in femtosecond filaments Coulomb and polarization effects in sub-cycle dynamics of strong-field ionization The role of the Kramers–Henneberger atom in the higher-order Kerr effect," New J. Phys. New J. Phys. New J. Phys. **15**, (2013).

130. A. M. Perelomov, V. S. Popov, and M. V Terent ’ev, "Ionization of Atoms in an Alternating Electric Field," J. Exp. Theor. Phys. **23**, 1393–1409 (1966).

131. A. Bahl, E. M. Wright, and M. Kolesik, "Nonlinear optical response of noble gases via the metastable electronic state approach," Phys. Rev. A **94**, 23850 (2016).

132. P. Béjot, J. Kasparian, S. Henin, V. Loriot, T. Vieillard, E. Hertz, O. Faucher, B. Lavorel, and J.-P. Wolf, "Higher-Order Kerr Terms Allow Ionization-Free Filamentation in Gases," Phys. Rev. Lett. **104**, 103903 (2010).

133. C. Brée, A. Demircan, and G. Steinmeyer, "Saturation of the All-Optical Kerr

Effect," Phys. Rev. Lett. **106**, 183902 (2011).

134. P. Béjot, E. Cormier, E. Hertz, B. Lavorel, J. Kasparian, J.-P. Wolf, and O. Faucher, "High-Field Quantum Calculation Reveals Time-Dependent Negative Kerr Contribution," Phys. Rev. Lett. **110**, 43902 (2013).